Doctoral thesis

NTNU
Norwegian University of Science and Technology
Thesis for the Degree of
Philosophiae Doctor
Faculty of Engineering
Department of Civil and Environmental
Engineering

Doctoral theses at NTNU, 2022:262

Martina Lan Salomon

Microstructural Investigation of Sea Ice and Imaging of Oil in Sea Ice by X-Ray micro-computed tomography

NTNU
Norwegian University of
Science and Technology

Martina Lan Salomon

Microstructural Investigation of Sea Ice and Imaging of Oil in Sea Ice by X-Ray micro-computed tomography

Thesis for the Degree of Philosophiae Doctor

Trondheim, September 2022

Norwegian University of Science and Technology
Faculty of Engineering
Department of Civil and Environmental Engineering

NTNU
Norwegian University of
Science and Technology

NTNU
Norwegian University of Science and Technology

Thesis for the Degree of Philosophiae Doctor

Faculty of Engineering
Department of Civil and Environmental Engineering

ISBN 978-82-326-5824-4 (printed ver.)
ISBN 978-82-326-6875-5 (electronic ver.)
ISSN 1503-8181 (printed ver.)
ISSN 2703-8084 (online ver.)

Doctoral theses at NTNU, 2022:262

Printed by NTNU Grafisk senter

All of old. Nothing else ever. Ever tried Ever failed. No matter. Try again. Fail again. Fail better. *(Samuel Beckett)*

Abstract

The alarming decline of sea ice extent over the last few decades has made the polar marine region and its resources more accessible to humans. This has resulted in increased shipping and mining activities in this area which in turn raise the probability of extremely hazardous and environmentally damaging oil spills in ice-covered waters.

Experimental studies and scientific analyses of sea ice microstructure are essential to describe the morphological, physical and physiomechanical properties of sea ice and hence develop strategies to deal with potentially devastating oil spills in ice-covered waters. To this end, we performed laboratory and field experiments combined with non-destructive X-ray micro-computed tomography investigations of clean sea ice and sea ice hosting oil and diesel. Based on the acquired data sets i) the evolution of sea ice on a pore scale and ii) the effect of oil in the sea ice pore space were studied.

Oil-free sea ice cores harvested during a field experiment in spring 2016 allowed us to study a wide variety of properties of young Arctic sea ice. Our investigations show that bulk properties such as salinity and density and structural properties such as the pore size strongly depend on the total brine porosity. The collected data set demonstrated little change in the variation of salinity, density, and pore sizes between samples. Nevertheless, we examined a significant decrease in pore number and an increase in pore connectivity over time.

In order to accurately analyse and interpret the distribution of oil and diesel distribution within sea ice imaged from computed tomography scans, different segmentation methods were developed. The segmentation approach methods developed in this study were designed to differentiate the low absorption contrast of oil/ diesel and ice and allowed us to investigate the oil and diesel distribution on a microscopic scale. We investigated the oil and diesel distribution on a selection of samples from four different experiments. We examined dispersed spread oil in the upper part of the ice cores and more channelized oil inclusion in the lower part of sea ice and with an average oil filled pore size of 0.04-0.2 mm.

Preface

This PhD study was conducted at the Department of Civil and Environmental Engineering at the Norwegian University of Science and Technology (NTNU) and the Department of Arctic Technology of the University Centre in Svalbard (UNIS). The thesis is submitted as partial fulfilment of the requirements for the degree of Philosophiae Doctor. The research is financially supported by the Norwegian Research Council (Grant No. 243812) and the Arctic Field Grant.

The doctoral work is organised as an article-based thesis and structured in two parts: *Part I* gives an overview of the conducted research during the PhD
Part II provides a selection of publications written during the PhD studies.

The study is supervised by Knut Vilhelm Høyland, Sönke Maus and Chris Petrich. The evaluation committee is formed by Matti Leppäranta, Professor emeritus from the University of Helsinki, Ross Lieblappen, Associate Professor at Vermont Tech and Irina Rogozhina, Associated Professor from NTNU, who performed as administrator.

Acknowledgements

Many contributed to making this thesis possible and the voyage an enriching experience. I am thankful for all the dedication and involvement from each of them. Thanks to everyone who fed my light of enthusiasm, especially in moments of doubt.

I appreciate Knut Vilhelm Høyland, Sönke Maus and Christian Petrich for their guidance, technical expertise and the freedom they gave me to pursue this study and the time I needed. The freedom I had did not make the path the most efficient but allowed me to wander in different directions and gave me the possibility to find the one most interesting to me. My sincere gratitude for your valuable advice and constructive feedback and your will to help to improve this work.

I am grateful for the time spent at UNIS conducting fieldwork with inspiring birds of a feather like Eef Van Dongen, Astrid Strunk and Sarah Sapper. Your helping hand in the field is highly appreciated, and your jolly company made those strenuous days unforgettable.

Credits to my dear friends Jokin Mendikute and Romana Gritzmann for your company on the journey to the HSVA- experiment and back and for your support during those nerve-wracking moments at the border control. Thank you, Sophie Woelke, for your assistance at the HSVA- experiment and your patience (especially when having difficulties understanding my weird Austrian phrases). I also would like to recognise Megan O'Sadnick and Marc Oggier for the early morning walks to HSVA and the strenuous and hard-working hours spent together and your constructive discussions and advice.

Special thanks to my dear colleagues and friends from the so-called 'Basement' who enlightened the daily life spent at NTNU. I am thankful for your support, the inspiring lunch conversations and the needed distraction from time to time. Many thanks to all my friends for a warm smile, a supporting hug and kind words. I want to express my sincere gratitude to Julie Lepage and Maria Azucena Gutierrez Gonzalez for your encouraging support. There is much to learn from emancipated women like you are. Sylvie Ginette Denise Lelu, Astrid Marie Flattum Muggerud, and Lars Martin Sandvik Aas, thank you for your open ears and sophisticated advice. Dave, I am grateful for your spontaneous help and invested time proofreading and improving the thesis writing.

At this point, it is time to express my gratitude to my parents, Julan and Gottfried, for their unconditional

love, positivism and encouragement to chase my dreams. Thank you, for providing endless opportunities and for your trust in me. To my brother Heinrich, who has been my partner in crime since I remember, I am more than thankful to have you by my side and for all the adventures spent together. I am grateful to call such a caring person my brother. Thank you for providing so much love and steadiness.

To my beloved children, Ailo and Linnea, I appreciate your care-free being, for keeping my every day sunny and refreshing, for a handful of laughter each day, sleepless nights and tons of cuddles and most important, for the outcome of this study, for providing a healthy balance between work and unforgettable moments. Finally, but dedicated not least, I want to express my sincere gratitude to Joan. Your motivation, love, mental support and self-sacrifice are priceless. Thank you for challenging me and enriching my life in so many different ways. The incidence of meeting you doubtless changed my life in an unexpected way to the better.

Dear Reader, I appreciate that you thoroughly read the acknowledgements. Please, feel welcome to dive further into the incredible sea ice expansion, and do not stop here. You will find adventurous odysseys about the sea ice harvest, mysteries unveiled by X-ray micro-computed tomography, and the courageous taming of the much-feared segmentation of oil from ice. I sincerely hope you enjoy the read.

Many thanks! Tusen Takk! Danke! 谢谢! Gracis!

Martina Lan Salomon

List of Tables

2.1 Overview of experiments 16
2.2 Field activity 18
2.3 Norut Experiments 19

4.1 Overview of CT- settings 44
4.2 Overview of measured parameters 47

Contents

I Summary Report

1 Introduction 3
1.1 Background 4
1.1.1 Earth's cryosphere 4
1.1.2 Sea ice formation and initial brine entrapment 6
1.1.3 Brine inclusions and their evolution 8
1.1.4 Air inclusions 10
1.1.5 Sea ice phases 11
1.2 Motivation 12
1.3 Research approach 12
1.4 Target of Research 12
1.4.1 Objective 12
1.4.2 Research topics 12
1.4.3 Scope 13
1.5 Thesis structure 13

2 Experimental 15
2.1 Svea: Field experiment 16
2.2 Norut: Small-scale ice tank experiment 18
2.3 HSVA: Large-scale ship tank experiment 20

3 Sea ice microstructure investigations and evolution 23
3.1 Introduction 24
3.2 Methods 25
3.2.1 Laboratory setup 25
3.2.2 μ-CT imaging and post imaging processing 25
3.2.3 Pore space analysis 26
3.3 Results and Discussion 30
3.3.1 Sea ice bulk properties 30
3.3.2 Pore characteristics 35

3.4 Conclusion 38

4 Fate of oil and diesel in sea ice 41
4.1 Introduction 42
4.2 Methods 43
4.2.1 μ-CT imaging 43
4.2.2 Segmentation 44
4.2.3 Pore space analysis 46
4.2.4 Oil content measurements on melted samples 47
4.3 Results and Discussion 48
4.3.1 Ice thickness 48
4.3.2 Temperature 48
4.3.3 Segmentation 49
4.3.4 Salinity and brine porosity 50
4.3.5 Oil porosity 53
4.3.6 Pore- and throat size distribution 54
4.4 Conclusion 57

5 Conclusion and future perspectives 61
5.1 Conclusion 62
5.2 Future perspectives 63

References 66

II Papers

Declaration of authorship 74

Paper I: Microstructure evolution of young sea ice from a Svalbard fjord using micro-CT analysis 76

Paper II: Quantitative analysis of oil and diesel distribution within sea ice pore space by micro-CT analysis 98

Paper III
Experimental and micro-CT study on the oil distribution in laboratory grown sea ice 156

Paper IV: Distribution of oil in sea ice: laboratory experiments for 3-dimensional μ-CT investigations 170

Acronyms and variables

AETB	Arctic Environmental Test Basin
C	coefficient giving the relation between solid salt mass and brine mass Cox and Weeks (1982)
DESY	Deutsches Elektronen-Synchrotron
f	factor to convert brine volume fraction between different temperatures
F1	empirical function based on sea ice phase relation Cox and Weeks (1982)
F2	empirical function based on sea ice phase relation Cox and Weeks (1982)
FOV	field of view
F_{SS}	factor to calculate the solid salt fraction
HSVA	Hamburgische Schiffbau-Versuchsanstalt
h_{ice}	ice thickness
iP	initial Pixel
k	gives the relation: mass of salt in the brine and mass of salt in the solid salts Cox and Weeks (1982)
μ-CT	X-ray micro-computed tomography
NaN	not a number
NTNU	Norwegian University of Science and Technology
Oil_{ref}	Oil content reference measurements
Oil_{CT}^{ref}	Oil content reference measurements conducted on melted samples by μCT
Oil_{UV}^{ref}	Oil content reference measurements conducted on melted samples by UV- fluorescent spectroscopy
Oil_{CT}	Oil content measurements conducted on frozen samples by μCT
OT	Object tracing
ϕ_{air}	air porosity
ϕ'_{air}	CT derived in situ air porosity
ϕ_{aircal}	air porosity calculated after Cox and Weeks (1982)
ϕ_{closed}^{air}	closed air porosity from CT images
ϕ_{open}^{air}	open air porosity from CT images
ϕ_b	brine porosity
ϕ'_b	CT derived in situ brine porosity
ϕ_{bcal}	brine porosity calculated after Cox and Weeks (1982)
$\phi_{bclosed}$	closed brine porosity
$\phi'_{bclosed}$	CT derived in situ closed brine porosity

ϕ_{bcon}	connected brine porosity
ϕ'_{bcon}	CT derived in situ vertically connected brine porosity
ϕ_{bopen}	open brine porosity
ϕ'_{bopen}	CT derived in situ open brine porosity
ϕ_{tot}^{brine}	total brine porosity from CT images
ϕ_{air}^{CT}	air porosity from CT images
$\phi_{airclosed}^{CT}$	closed air porosity from CT images
ϕ_{aircon}^{CT}	vertically connected air porosity from CT images
$\phi_{airopen}^{CT}$	open air porosity from CT images
ϕ_{brine}^{CT}	brine porosity from CT images
ϕ_{tot}^{oil}	total oil porosity from CT images
ϕ_{z+}	pore fraction accessed from the upper sample surface in z-direction
ϕ_{z-}	pore fraction accessed from the lower sample surface in z-direction
$\phi_{z\pm}$	pore fraction accessed from the upper and the lower sample surface in z-direction
PS	Pore size
PSD	Pore size distribution
PS_{oil}	Pore size distribution for oil fraction
RECX	Norwegian Centre for X-ray Diffraction, Scattering and Imaging
ROI	region of interest
ρ_{air}	air density
ρ_{brine}	brine density
ρ_{bulk}	sea ice bulk density
ρ_{CT}	porosity derived sea ice bulk density
ρ_{hydro}	sea ice bulk density derived from hydrostatic measurements
ρ_{ice}	ice density
ρ_{par}	paraffin density
ρ_{SS}	solid salt density
SAS	semi-automated segmentation
S_b	brine salinity
S_{bcent}	brine salinity of brine removed during centrifuging
S_{bdrip}	brine salinity dripped from sample during transport from field to the laboratory
S_{free}	bulk salinity from oil free cores measured by conductivity
S_{cent}	bulk salinity measured on centrifuged samples
S_{CT}	bulk salinity derived from porosity
S_{ice}	sea ice bulk salinity
S_{oil}	bulk salinity from oil & diesel cores measured by conductivity
S_{rest}	bulk salinity from cut-off accumulated by downsizing of samples for investigations on the microstructure
SLF	WSL- Institut für Schnee- und Lawinen Forschung
T	in situ ice temperature
T_{CT}	imaging temperature

T_{ice}	ice temperature
T_{ocean}	ocean temperature
T_f	freezing point
TS_{oil}	Throat size distribution for oil fraction
TSD	Throat size distribution
XRT	X-ray micro-computed tomography
UNIS	The University Centre in Svalbard
VOI	Volume of interest
W_{air}	sample weight measured in air
W_{par}	sample weight measured fully submerged in paraffin
WSL	Eidgenössische Forschungsanstalt für Wald, Schnee und Landschaft

Part I

Summary Report

Chapter 1

Introduction

It is the set of the sails... that determines which way we will go. (Jim Rohn)

1.1 Background

Increasing global temperatures has led to a substantial decline in the extent of sea ice which has in turn made the polar marine region more accessible to humans (e.g., Vaughan et al., 2013; IPCC, 2014, 2021). Therefore, historically remote previously inaccessible areas are becoming increasingly attractive for conventional heavy industrial operations such as mining, oil-and-gas- production, as well as marine shipping (e.g., Peters et al., 2011; Smith and Stephenson, 2013; Assesment, 2010). Moreover, sea ice acts as a critical element within the climate system with significant influence over heat and moisture transfer and the global albedo (Ebert and Curry, 1993). Sea ice provides the habitat for a whole ecosystem vital for the Arctic food web (Legendre et al., 1992). The microstructure of the sea ice can strongly influence its physical, biological and engineering properties. The presence of salt in the ocean (average 35 ‰) makes sea ice a permeable material, as it gives rise to a network of brine channels and air pockets. The size and connectivity of this network changes with temperature and strongly affects the properties of sea ice. Studying and understanding the sea ice structure at the microscale can help us solve challenges faced on the macroscale and cope with hazard management of potential oil spills in ice-covered waters. Experimental studies and scientific analyses of sea ice microstructure are essential to develop strategies to deal with devastating oil spills in ice-covered waters. Proper hazard response is dependend on the understanding of the sea ice microstructure evolution on a pore scale and the understanding of the fate of oil in the sea ice pore space.

1.1.1 Earth's cryosphere

Ice covers approximately 10 % of the Earth's surface, and on average 7 % of the oceanic surface is covered annually (Reay et al., 2007). The Cryosphere consists primarily of meteoric ice (e.g., snow cover, glaciers, ice caps, ice sheets), sea ice, freshwater ice in lakes and rivers and frozen ground.

Snow consists of **meteoric ice** crystals that precipitate as snowflakes from clouds. Clouds form by condensation of water vapour to liquid water or sublimation to ice in the presence of solid particles by aerosols in present. In cold regions and at high altitudes, clouds usually consist of ice or a mixed solid and liquid water phase. When the temperature decreases to 195 K or lower, snow precipitates from polar stratospheric clouds (Bartels-Rausch et al., 2012). Once fallen to the ground, the single hexagonal crystals grow together (i.e. sinter), and eventually transform under mechanical load and metamorphism to ice, creating glaciers, ice caps and ice sheets, ice shelfs and icebergs. The IPCC (2021) summarizes that nearly 45 % of the land surface in the Northern Hemisphere is covered by snow at its annual maximum in winter. Ice sheets hold 99.5 % of the perennial ice volume (Davies, 2022) while glaciers constitute less than 1% of the global ice volume (IPCC, 2021).

Subsurface ice forms when the water content in soil and rocks freezes. The pore water filling the ground (either partially or entirely frozen) forms pore ice or ice films. Ice layers or lenses (0.15-13.0 cm thick) form as the ground retracts water during freezing, and are known as segregated ice. Superimposed ice can be distinguished in seasonally frozen ground and permafrost, where permafrost stays below 0 °C for at least two consecutive years

(Everett, 1989). Permafrost occurs when the winter ground freezing exceeds the summer thawing (Dobinski, 2011). It occurs both on land and beneath offshore arctic continental shelves, and underlies about 22 percent of the Earth's land surface (National Snow and Ice Data Center, 2020). In the Northern Hemisphere, around 58 % of the land freezes seasonally (National Snow and Ice Data Center, 2020).

Freshwater ice cover develop in high-latitude freshwater bodies during winter months. The area and volume of freshwater ice are small compared to other components of the cryosphere (IPCC, 2014). In the boreal zone, tundra, and mountain regions, lakes freeze seasonal, while in very high altitudes and high polar latitudes, a perennial lake ice cover can develop (Leppäranta, 2015). Lake freezing is stratified since the maximum density of water is met before the freezing point (Figure 1.1.) As atmospheric cooling occurs, the fluid density increases until 4 °C. The surface layer of the lake in contact with the atmosphere cools faster than the underlying warmer fluid, creating convection. The convective mixing continues until the mixing layer is cooled to 4 °C, after which a stable situation where colder (less dense) water sits on top of warmer (more dense) water occurs and faster cooling occurs. Eventually, as atmospheric cooling continues, the lake develops an ice cover. Unlike lakes, turbulent mixing in rivers caused by streams requires the entire water depth to cool uniformly even after the maximum density at 4 °C is met.

Sea ice formation starts with the atmospheric cooling of the ocean below freezing temperature. Typically a water layer of 10 to 40 m needs to be cooled to -1.8 °C, called the surface mixed layer. This layer experiences an unstable situation due to density differences (Figure:1.1). For salinity higher than 24.7 ‰ the temperature of maximum density is lower than the freezing point. The oceans have an average salinity of 35 ‰, meaning that during consistent cooling below the freezing point, the density of the surface layer is higher than the density of underlying warmer fluids, creating an unstable situation and convection. Once the mixing layer (typically 10-40 m) has reached freezing temperature, ice formation will start before the density maximum is reached (Weeks, 2010).

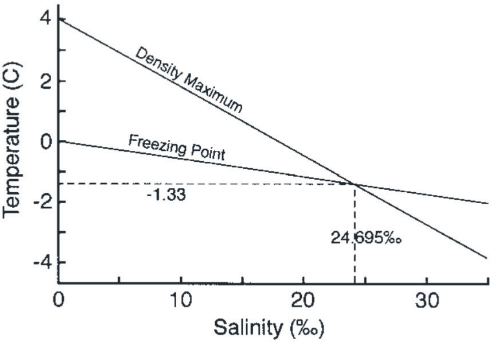

Fig. 1.1 Density maxima and freezing point as a function of salinity. From (Weeks, 2010).

1.1.2 Sea ice formation and initial brine entrapment

The initial ice crystal nucleates with the aid of particles in the presence of a thin supercooled surface layer, where sea water typically does not supercool by more than 0.1 K (Fletcher, 1970). These primary ice crystals (called frazil ice) typically have a diameter of a few millimetres to tens of millimetres and a thickness of less than a millimetre (Weeks, 2010). The frazil may freeze together and form a continuous ice cover. The initial thin ice cover is characterized by randomly shaped and oriented crystals describing **granular ice** (Figure 1.2). Under the presence of winds and waves, frazil ice forms within a turbulent surface layer, and not only at the surface. When the wind-driven turbulence ceases and the submerged ice crystals float to the surface, a deeper initial granular ice layer forms.

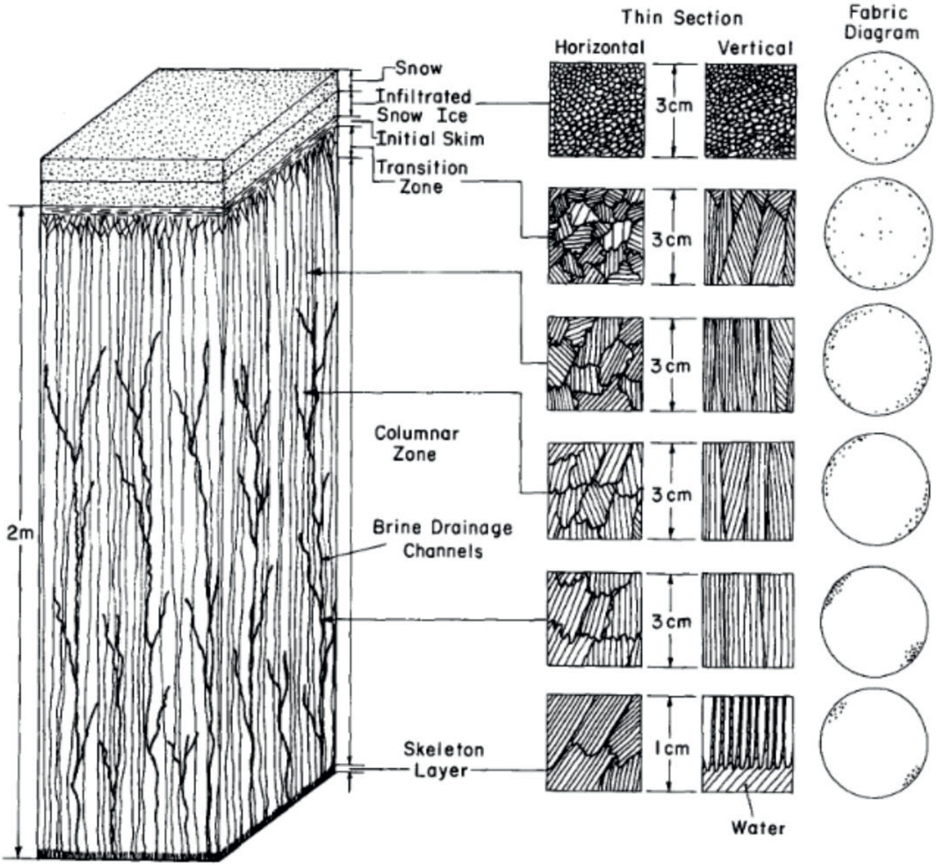

Fig. 1.2 Schematic diagram of typical congelation first year sea ice structure from Maykut et al. (1992). The first columns shows the typical structure of first year sea ice, with snow, infiltrated snow ice and the initial ice skim with a granular texture on the top. The granular ice is underlain by the transition zone, the columnar zone and the skelatal layer. Column two represents schematic horizontal and vertical thin sections and the third column presents typical c-axes orientation found in the different levels of young sea ice.

Once a continuous ice layer has formed at the sea surface, growth conditions change, and the transition zone is entered. The **transition zone** (Perey and Pounder, 1958) is characterised by a mixed ice texture consisting of granular and columnar ice (Figure 1.2). The ice cover growth in this zone depends on the balance of heat flux between atmosphere and ocean. Furthermore, ice crystals prefentially grow in a vertical direction (c-axes oriented parallel to the water surface) as they otherwise interfere with neighbouring grains (Figure:1.3). Since ice crystals with horizontal c-axes orientation are favoured, geometric selection appears and leads to anisotropic growth. The geometric selection is commonly present within a vertical distance of less than 10 cm from the ice-air interface, where the bottom of the transition zone is present within 15 cm. (Weeks, 2010).

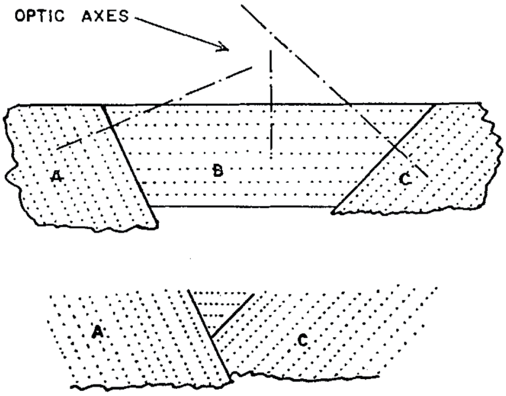

Fig. 1.3 Schematic diagram of the geometric selection in sea ice growth, representative for the Transition Zone from Perey and Pounder (1958). In the upper picture three individual oriented sea ice crystals are shown (A,B and C). The lower pictures depicts that the growth conditions of crystal A and C are favoured due to the orientation of the optical axes and advantageous thermal conductivity.

Below the transition zone, when geometric selection largely resulted in horizontal c- axis orientation, the ice is called columnar. The **Columnar Zone** is defined by congelation ice with a strong alignment of the c-axes in the horizontal direction and pronounced elongation of the ice grains with a typical lamellar substructure, which favours heat conduction (Figure 1.2). Maykut et al. (1992) reports a gradual increase in the average crystal size measured in the horizontal plane with depth. Pore size and shape, including brine tubes and channels, are characteristically parallel to the grain boundaries.

The lower 2- 3 cm in a growing ice sheet is called the **skeletal layer** (Figure 1.2). This layer is associated with little mechanical strength. The weakness is related to the lack of horizontal ice contact with a high brine volume fraction (Cox and Weeks, 1986). As sea ice grows, the salt from the ocean is rejected. Salt rejection is related to the molecular structure of ice and salt. The crystal lattice of pure ice consisting of H_2O has an approximate unit cell volume of 130 $Å^3$ (O-O distance 2.76 Å). At the same time, NaCl shows a unit cell volume of 179 $Å^3$ (Cl-Cl distance 5.64 Å) which makes it too big to be incorporated into the crystal lattice of ice. As the sea ice grows downwards, salt builds up in a thin layer ahead of the growth front resulting in a concentration gradient. This gradient, in consequence, leads to the diffusion of salt from the growth front towards the less salty ocean. At the same time, heat exchange by diffusion from the warmer ocean towards the colder growth front appears. Since heat transport is an order of magnitude faster than salt diffusion, a thin, slightly salt enriched layer in front of the growth interface is cooled below the freezing point. This mechanism leads to constitutional supercooling and a nonplanar, cellular interface, and brine entrapment (Weeks, 2010) (Figure: 1.4.) The pore microstructure (i.e. crystal size and orientation and layer spacing of pores) is manifested in the crystal pattern developed in the skeletal layer (Petrich and Eicken, 2016).

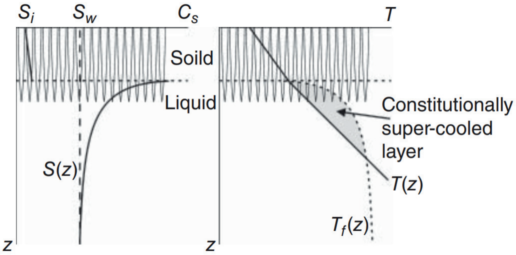

Fig. 1.4 Schematic diagram of the skeletal layer, with corresponding salinity gradient (left) and temperature changes (right) from the freezing interface toward the ocean. S_i denotes the sea ice salinity and S_w the ocean salinity. The skeletal layer consists of lamellar ice crystals separated by brine layers. $T_f(z)$ is the freezing temperature (dashed line to the right) at the actual salinity (S(z)) (to the left). The actual temperature profile (solid line to the right) is colder than $T_f(z)$. The grey zone represents the constitutional supercooled layer. From Petrich and Eicken (2016).

An important parameter to describe the substructures within an ice crystal is the brine layer spacing (λ) (Figure:1.5). λ describes the distance between the centres of two neighbouring brine layers measured parallel to the c-axis as a function of the growth velocity v. λ often increases with distance from the sea ice surface and is inversely proportional to the growth velocity. In young sea ice λ shows typical values from 0.4 mm near the air-ice interface and around 1.0 mm at the bottom (Weeks et al., 1962)). Maus (2020) reviews existing observations on the average brine layer spacing depending on the growth rate. Maus (2020) presents a simplified model of the brine layer spacing based on the theory of constitutional supercooling (Rutter and Chalmers, 1953).

1.1.3 Brine inclusions and their evolution

The brine layer spacing is an initial length scale of sea-ice microstructure evolution. As skeletal layer growth continues, the temperature in the upper part of the skeletal layer decreases. The reduction in temperature leads to a decrease in brine inclusion size and brine volume. As the ice lamellae thicken and eventually bridge, a pure ice matrix hosts an increasing number of minor isolated brine inclusions. The described intercellular entrapped brine is further referred to as primary brine inclusions, which will merge and create a whole network of brine channels. Some residual brine is likely to stay connected as long as freezing increases the pore pressure and pushes brine through the matrix. Additional brine channels form, indicating the favoured pathway of brine movements. Upon warming, the brine inclusions will enlarge. This secondary pore space is characterized by longer and broader channels than the primary pore space (Petrich and Eicken, 2016).

Several processes lead to the redistribution of brine within the ice cover, to desalinisation and the development of the sea ice pore structure. Processes such as brine pocket migration, brine expulsion, gravity drainage and the coalescence of pores are described.

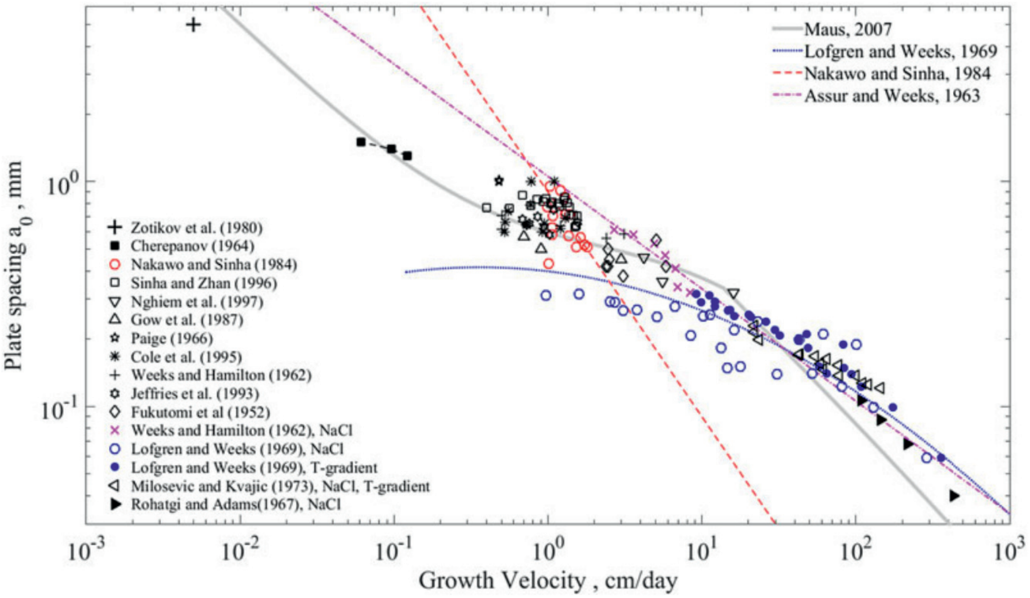

Fig. 1.5 Average brine layer spacing (λ) denoted as a_0 in dependency of growth velocity (v). Summary of brine layer measurements from different experiments. From Maus (2020).

Brine pocket migration As brine strives for thermal equilibrium, temperature changes within the ice cover will lead to redistribution and migration of brine. Temperature gradients in the ice causes concentration gradients in the brine pockets. In growing sea ice, the upper part of the ice (closer to the atmosphere) is colder than the lower part (closer to the ocean). The temperature gradient causes the salinity and density to increase towards the surface under thermodynamic equilibrium. This unstable situation favours salt diffusion from the top of the brine inclusion towards the bottom. In return, ice forms at the top and dissolves in the bottom part of the brine pocket as described by Whitman (1926). Consequently this leads to a slow downward brine pocket migration. Untersteiner (1968) calculated the migration for a brine pocket located 10- 20 cm below the sea ice surface in Antarctic multiyear ice. The author concluded that the brine pocket migrates 2 cm downwards between August and April and an equal amount upwards from May to June, resulting in net migration of essentially 0. In brine inclusions bigger than 1 mm in diameter, in addition to diffusion, thermal convection might appear, speeding the processes of brine pocket migration up. The significance of brine pocket migration is limited to microscopic observation but might also affect the pore space connectivity (Petrich and Eicken, 2016).

Brine expulsion Freezing of brine causes a volumetric change, since ice (ρ_{ice}= 918.0 kgm^{-3} at -10 °C) is less dense than brine (ρ_{brine}= 1000+0.08*$S_b[kgm^{-3}]$ (Zubov, 1945) or 1113.2 kgm^{-3} at -10 °C). Consequently, the phase change leads to a pressure increase within the brine pocket, failure of the ice in the vicinity and redistribution of brine within the ice. Most brine is expelled at higher temperature, when brine pores are connected. Notz and Worster (2009) concluded that the brine flow rate is always lower than the growth rate of sea ice at the lower interface and furthermore assumed that the brine cannot leave the ice during sea ice growth and is instead redistributed by brine expulsion.

Gravity drainage The brine density profile within the ice cover is unstable during the winter months due to thermodynamic equilibrium. Therefore, the highest brine density is observed at the top of the ice flow. Studies propose that this situation results in an overturn of brine and some replacement with seawater in permeable sea ice. Notz and Worster (2009) suggests that gravity drainage is the leading mechanism of salinity loss during winter months.

Coalescence of pores During the melt season and warming temperatures, the brine salinity within the brine pockets decreases, consequently increasing the brine freezing temperature. The reduction in brine salinity is caused by an increase in brine volume via the melt of pure ice diluting brine and leading to an expansion of brine inclusions (Perovich and Gow, 1996). Warming sequences cause brine inclusions to merge, and bigger inclusions grow at the cost of smaller inclusions (Ostwald ripening) to accomodate the expansion of brine inclusions (Figure 1.6).

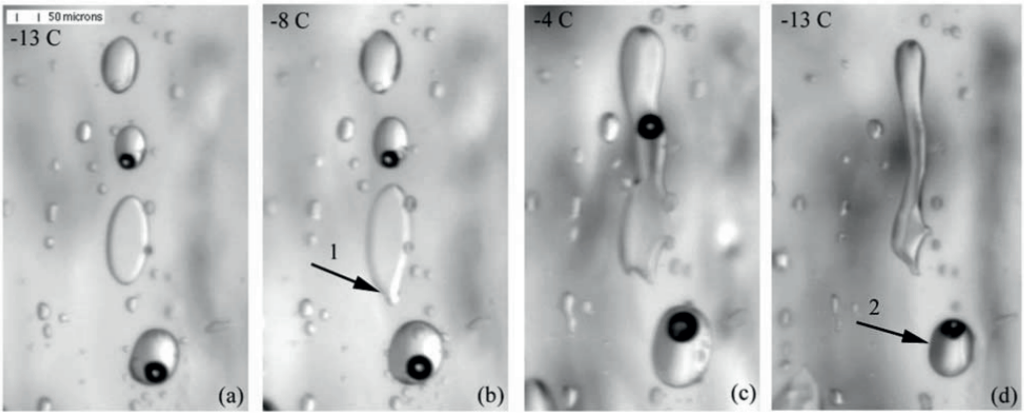

Fig. 1.6 Changes in brine pockets during a warming sequence. a) -13 °C, b) -8 °C,c) -4 °C and cooled to d) -13 °C. Arrow 1 indicates merged brine inclusion, and arrow 2 indicates shrinkage of a brine pocket. In Figure 1.6d), inclusion remained merged after cooling. From Light et al. (2003).

1.1.4 Air inclusions

Dissolved gases are entrapped during sea ice formation and growth, forming the gas porosity of ice. Furthermore, we refer to the gas porosity as air porosity. Gas is excluded from the ice growth process since the crystal lattice structure of pure ice can only accommodate a limited amount of impurities. Loose et al. (2009) observed that 45 to 61 % of O_2 is rejected during ice growth and accumulates at the growth front. Since the gas concentration increases, a gradient appears, and diffusion from the growth front towards the ocean occurs. Gases have a higher diffusion coefficient in comparison to salt (Loose et al., 2009). This phenomena leads to a lower air porosity (ϕ_{air}) than brine porosity in the ice (ϕ_b), as gases are more effectively rejected. Loose et al. (2009) concluded that at a lower freezing rate (higher temperature), gasses have more time to diffuse from the growth interface. Hence, fewer gases are entrapped in the ice. The gas content expressed as air volume fraction (ϕ_{air}) in first-year ice frequently occurs in the range of 2 to 30‰. The upper portion hosts more air volume up to around 55‰, with the highest values at the top Weeks (2010). In first year sea ice the air pockets are generally cylindrical or spherical (Lieb-Lappen et al., 2017), and the diameter of air inclusions varies from micrometre-scale (Light et al., 2003) up to several millimetres (Perovich and Gow, 1996). Other mechanisms for gas entrapment in sea ice are:

- Freezing of already encapsulated brine leads to a supersaturation of gases. This induces air bubbles to form within the brine inclusion (Glud et al., 2002).
- Replacement of brine with air due to brine drainage (Tsurikov, 1979).
- "Snow ice formation", flooding of snow with seawater and refreezing. Air present in the snow cover becomes trapped in the ice(Tsurikov, 1979).
- Internal melting of ice, the volumetric change from ice to water induces bubble formation (Tsurikov, 1979).
- Oxygen production via respiration by microorganisms (Glud et al., 2002).

1.1.5 Sea ice phases

The sea ice phase diagram is essential to understand the relationship of the different phases within sea ice (ice, brine, solid salt) at specific temperatures. The classic phase relation, given by Assur (1960) based on experimental data from Nelson (1953) and Nelson et al. (1954), describes the physiochemical phase relation for a standard composition of sea ice to predict characteristic sea ice behaviour regarding cooling and warming. Despite information on the phase volumes, no direct information on the sea ice microstructure can be drawn from this data. Following the classical phase relations in sea ice, Cox and Weeks (1983) derived a set of equations to obtain the brine (ϕ_b) and air volume fractions (ϕ_{air}) as a function of the sea ice temperature T_{ice}, bulk salinity S_{ice} and the bulk density ρ_{bulk}. Any change in T_{ice} affects the brine salinity S_b, phase volumes and consequently the sea ice microstructure. Ideally one obtains the sea ice bulk density ρ_{bulk} to calculate the phase volume fractions. ϕ_b is determined as:

$$\phi_b = \frac{\rho_{bulk} * S_{ice}}{F1(T_{ice})} \tag{1.1}$$

and ϕ_{air} is calculated as:

$$\phi_{air} = 1 - \frac{\rho_{bulk}}{\rho_{ice}} + \rho_{bulk} * S_{ice} * \frac{F2(T_{ice})}{F1(T_{ice})}; \tag{1.2}$$

where ρ_{ice} is the ice density at temperature T_{ice} and F1 and F2 are empirical functions based on the phase relation. $F_i(T_{ice}) = \alpha_0 + \alpha_1 T_{ice} + \alpha_2 T_{ice}^2 + \alpha_3 T_{ice}^3$. ρ_{ice} is given in kg/m^3 and T_{ice} in °C as: $\rho_{ice} = 916.7 - 0.1403 T_{ice}$. Coefficients are listed in Cox and Weeks (1983) for a temperature range from -2 to -30 °C. Coefficients for the phase volume fraction calculation on warmer sea ice, with T_{ice} in the range of 0 to -2 °C are recorded in Leppäranta and Manninen (1988).

1.2 Motivation

This PhD project is motivated by the need to improve the current knowledge regarding sea ice microstructure and its interaction with oil. Currently Norway's largest industry is petroleum, and development into the higher Arctic is expected. Licences awarded by the Norwegian Petroleum Directorate (e.g., Licence 1134, granted 2021 in Licensing round 25) lay in seasonally ice-covered areas. Quantitative descriptions of sea ice microstructure and behaviour and distribution of oil within this structure will help to inform effective response strategies in the case of oil spills and therefore help mitigate the subsequent risks of environmental and ecological damage.

1.3 Research approach

Field and laboratory studies on sea ice were planned and performed. The microstructure of sea ice containing oil and oil-free samples from the experiments was investigated by 3-D X-ray micro-computed tomography (μ-CT). μ-CT scans were morphologically analysed and statistically interpreted with the understanding of the physical processes.

1.4 Target of Research

1.4.1 Objective

The main objective of this research was to investigate the interaction of sea ice with oil on the pore scale. Through analyses of non-destructive imaged sea ice samples by μ-CT, the brine, air and oil size distribution were analysed in order to acquire insights into the underlying physical processes.

1.4.2 Research topics

From the objectives, the following research topics are identified:

- Study of the microstructure evolution of "non-contaminated" sea ice.
- Investigation and quantification of pore parameters of oil-contaminated sea ice.
- Develop an enhanced semi-automated image segmentation method due to similar absorption contrast of oil and ice in μ-CT scans.
- Analysis of the spatial distribution of oil in sea ice.

1.4.3 Scope

To meet the research objectives, the following scope is defined:

- Experimental preparation and performance of under-ice oil spills and their fate on the porous space of sea ice through laboratory experiments and field investigations.
  - Small-scale ice-tank experiment at Norut (Northern Research Institute AS). Our experiments aimed to investigate the oil distribution and concentration within laboratory grown sea ice by using μ-CT imaging.
  - Field observations on Svalbard, Norway. Six-weeks sea ice microstructure evolution and diesel distribution study on naturally grown young sea ice.
  - Four-weeks large-scale ice-tank experiment at HSVA (Hamburgische Schiffbau- Versuchsanstalt). Examinations on the oil migration and distribution in sea ice and the near-surface detectability.
- Work-flow allowing objective differentiation of ice and oil signal obtained by μ-CT.
- Characterisation of the oil-, air-, brine-volume fraction, pore size distribution, porosimetry, and porosity.
- Obtaining sea ice bulk properties such as sea ice temperature, salinity and density.

1.5 Thesis structure

This thesis is organised as a collection of scientific papers and divided into two parts. *Part I* gives an overview of the conducted research work during the PhD.

- Chapter 1 provides an introduction and background information to the research topic. The motivation to conduct the research is described. The objectives, research topics, and the scope of the work are presented. Finally, this discloses the outline of this thesis.
- Chapter 2 describes the experimental set-ups.
- Chapter 3 elaborates on the microstructure investigation and evolution of oil-free young sea ice based on field data.
- Chapter 4 presents the fate of oil on the pore scale and characterises oil inclusions investigated on μ- CT scans. And describes the executed work steps to establish a semi-automated oil segmentation.
- Chapter 5 provides the conclusions and recommendations for further research.

Part II comprises the scientific publications of the PhD research.

Chapter 2

Experimental

Difficulties are just things to overcome. (Ernest Shackleton)

Data were collected during four different types of field and laboratory experiments described in this chapter, ranging from small scale ice-tank experiments to ship-tank and field experiments summarised in Table 2.1.

Table 2.1 Overview of experiments

Experiment	ice type	Type of experiment	Paper
Svea	mixed*	field	*Chapter 3 & 4 (Paper I, II)*
HSVA	mixed* & columnar	large scale ship-tank	*Chapter 4 (Paper II)*
Norut I & II	columnar	small scale ice-tank	*Chapter 4 (Paper II,III,IV)*

*mixed: columnar with granular ice on top

2.1 Svea: Field experiment

During spring 2016 (16 March - 23 April) a field study located in Sveasundet (Spitsbergen) south of Sveagruva in Van Mijenforden (77°53'13.0"N 16°44'23.1"E) was conducted (Figure: 2.1). The aims of this experiment were to obtain i) a data set to investigate the porous space throughout the field season and ii) a data set to investigate the behaviour of diesel within the pore structure.

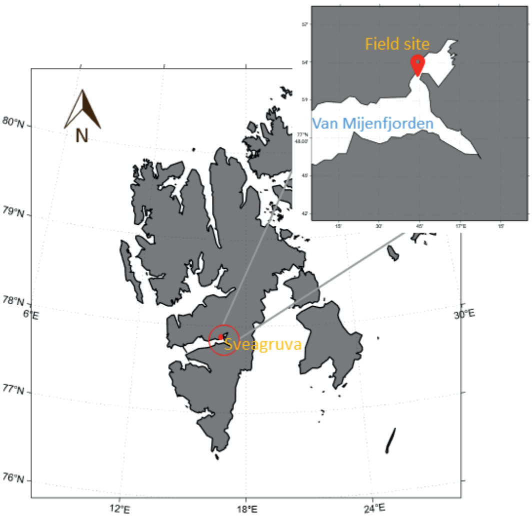

Fig. 2.1 Field work location: Sveasundet, south of Sveagruva in Van Mijenfjorden, Spitsbergen (77°53'13.0"N 16°44'23.1"E)

Before sampling sea ice, the field site was prepared on 16 and 17 March 2016 to minimise oil intrusion into the environment. An area of 12x12 m was subdivided into 16 smaller fields, each 3x3 m. A cardboard tube with an inner diameter of 7.8 cm (outer diameter 8.2 cm) and a length of 50 cm was placed in the centre of each square. The cardboard tubes enclosed the later artificially created under-ice diesel spill. One cardboard tube was equipped with two sets of temperature sensors. Each set comprised of six type T thermocouples spaced 10 cm apart. One set of temperature sensors faced south and the other one north. No oil was injected into the cardboard tube with the temperature sensors. The sea ice temperature signal from the sensors was logged with a USB-5104 4-channel logger from Measurement Computing every 5 seconds. Furthermore, a temperature sensor to measure the ocean temperature (SBE 56, Sea bird Scientific) with a resolution of 0.00001 °C and an accuracy of ±0.00286 °C in the temperature range of -5 to +35 °C was deployed at 1.2 m below the sea ice surface. The ocean temperature was logged every two minutes.

To submerge the cardboard tubes in the sea ice cover, ice cores were drilled using a Kovacs core barrel (7.2 cm diameter diameter). The ice core was extracted and immediately relocated into the cardboard tube and returned to the original position. The temperature sensors were oriented south and north. The sea ice thicknesses of the submerged cores were 29 - 37 cm. After relocating the ice core into the cardboard tubes and returning to the original positions within ice cover, the cores were left for 2-4 days to refreeze before oil injection experiments were conducted. The 15 installed cardboard tubes for oil injection had aluminium pipes (inner diameter: 5.1 mm, outer diameter: 6.0 mm) to facilitate oil injection. The top part of the pipes was covered with a screw-threaded lid. The bottom was sealed with a latex membrane. Covers avoided seawater entering the pipe and plugging it. Two days after the cardboard tube installation, oil was injected through the aluminium pipes. The lid on the top was removed, and the latex membrane was punctured. A two-meter long silicone tube was mounted on the top end of the aluminium pipe. A funnel mounted to the silicone tube was filled with motor oil (Lazerway 5W-40 from Circle K). By lifting the funnel, potential energy was used to try to overcome the hydrostatic pressure of the sea to enable transfer of the motor oil into the cardboard tube. However, the high viscosity of the motor oil at low temperature prevented sufficient flow and this strategy was abandoned. In order to overcome this issue experienced attempting to inject motor oil, injection of winter diesel (Circle K) was attempted instead and the injection strategy was modified. The end of a silicone tube was now formed to a hook and mounted to a stick. Next to each cardboard tube, we drilled a hole through the ice cover. The syringe was submerged through the drilled hole, and the neighbouring cardboard tube was hooked. After manoeuvring, we commenced with the diesel injection using a funnel as described previously.

After preparation of the field site, sampling was conducted as summarised in Table 2.2, which gives an overview of the field activity. On each sampling day, we measured the snow depth with a ruler (resolution: 1 mm), snow temperature, slush-ice interface temperature and two sea ice temperature profiles with a portable thermometer (HI 93510 from Hanna Instruments, accuracy: 0.4 °C, resolution: 0.1 °C). Two salinity cores, one density core, two diesel-free cores for pore structure analysis with the μ- CT, and diesel cores were sampled. The length of all cores was measured. Salinity cores were subsampled to a length of 2.5 cm from bottom to top, and density cores were cut into subsamples of 5 cm in length. Both salinity and density subsamples were packed in plastic containers before they were transported in an upright position and at ambient temperatures to the laboratory in Longyearbyen. Microstructure cores were subsampled into 2.5 cm lengths from bottom to top and stored in conical plastic containers. Conical containers were chosen to minimise contact between the sample and the container walls. Samples were transported in an upright position close to their in situ temperature, in portable battery-powered cooling boxes (WAECO) to the laboratories at The University Centre in Svalbard (UNIS). Sampled diesel cores were wrapped as a whole into plastic bags and were transported at ambient temperature to the UNIS laboratory.

Table 2.2 Field activity

Date	Work	h_{ice}	T_{ocean}	T_{ice}	S_{ice}	ρ_{bulk}	μCT_{ice}	oil
16 March	Preparation							
17 March	Preparation & sampling	35.6 cm	×	×	×	×		
19 March	Oil injection							
21 March	Oil injection							
30 March	Sampling	40.4 cm	×	×	×	×	×	×
06 April	Sampling	38.9 cm	×	×	×	×	×	×
12 April	Sampling	42.2 cm	×	×	×	×	×	×
23 April	Sampling	47.5 cm	×	×	×	×	×	×

h_{ice}: *average ice thickness, measured on extracted cores,excluding oil cores*

2.2 Norut: Small-scale ice tank experiment

We performed small-scale ice tank experiments at the former Northern Research Institute AS (Norut) in Narvik, Norway, now administrated by Stiftelsen for industriell og teknisk forskning (SINTEF). The experiments were conducted in slightly conical, double-walled Plexiglas tanks 51 x 51 x 51 cm in dimensions (inner-dimensions of 50 x 50 x 50 cm, figure 2.3. In order to provide cooling of the water column from top, to allow quasi-one-dimensional columnar ice growth with a planar growth front, radiant heat was supplied from below the tank that was homogeneously distributed by means of a fan and the tank was insulated using Styrofoam. The tanks were filled with around 100 L of artificial saltwater (Blue Treasure Synthetic Salt). Before initiating ice growth, we lowered the water temperature roughly to 0 °C. Sea ice was grown at an ambient air temperature of -15 °. The room was cooled to this temperature, which was determined to be the starting point of the experiment. Once the ice reached a thickness of 3.5 - 8.0 cm, a silicone syringe with a diameter of 0.5 cm was used to inject oil beneath the ice surface. Once the oil was encapsulated, ice samples were taken using a core barrel of 5 cm in diameter. Two slightly different experiments were conducted in this manner. The main differences in the experiments are summarized as follows and listed in Table 2.3. We acquired two μ-CT data sets of the samples from experiment Norut I at NTNU and SLF (WSL-Institut für Schnee- und Lawinenforschung SLF, Davos, Switzerland). Harvested ice cores from experiment Norut II were imaged by synchrotron-based μ-CT at DESY (Deutsches Elektronen-Synchrotron, Hamburg, Germany). In the Norut I experiment, circular Styrofoam patches 3 cm in diameter were deposited on the sea ice surface once the ice thickness reached 6.5 cm. The styrofoam patches slowed down the local ice growth and created under ice cavities. These cavities hosted the injected oil. Additionally, we increased the ambient temperature to -10 °C one day after the oil injection to allow oil migration. Sampling was conducted three days after the oil injection by which time the ice thickness was 11-13 cm. After sampling, we stored the specimens at -80 °C overnight before transportation to NTNU where they were stored at -50 °C. Prior to the μ-CT imaging at SLF, specimens were cut into subsamples of 2.0- 3.5 cm in height and a diameter of 3.5 cm. Samples were transported between NTNU to SLF at -15 °C.

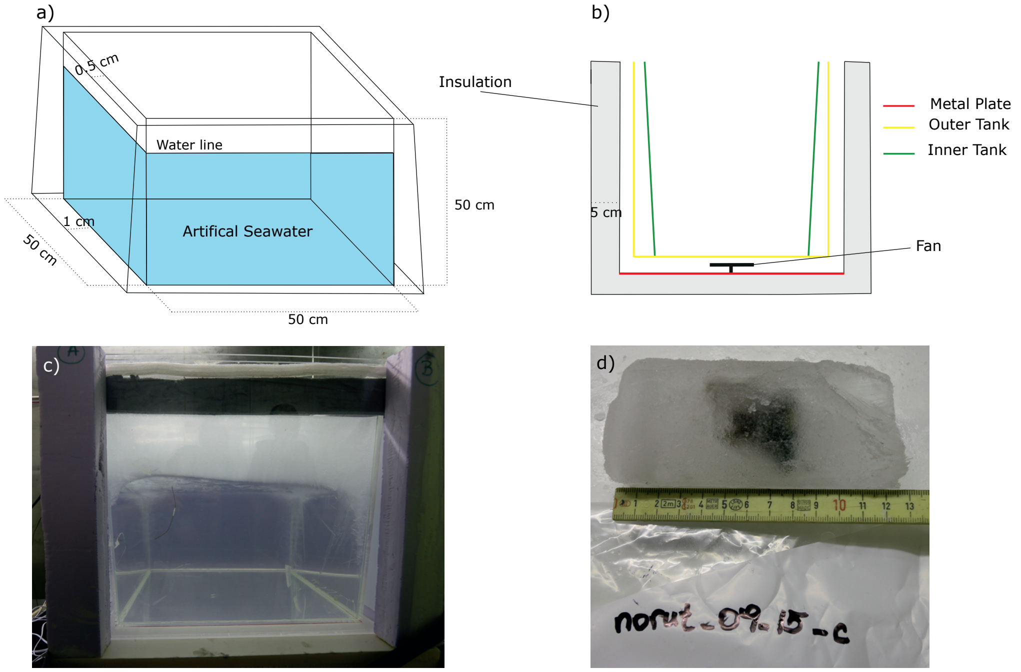

Fig. 2.2 Small-scale ice tank setting. a) Depicts the slightly conical, double walled sea ice tank. b) Cross sectional view of the ice tank. Styrofoam for insulation creates the outer layer of the tank. Two plexiglass walls with an air cushion in between providing extra insulation. At the bottom tank a fan distributes the heat sourcing from a metal plate. Sketches are not to scale, from Salomon et al. (2016). c) shows a photography of the ice tank and d) depicts an ice sample containing oil.

In the Norut II experiment, crude oil injection was undertaken twice. We injected the first oil droplets at an ice thickness of 3.5 cm and the second oil injection at an ice thickness of 8.0 cm. We proceeded with the sampling at an ice thickness of 10-11 cm. Harvested ice cores were subsampled to 8.75 mm in diameter and placed into tightly fitting plastic containers. The samples were transported in two portable battery-powered cooling boxes by train from Narvik via Stockholm and Copenhagen to the Deutsches Elektronen- Synchrotron (DESY) in Hamburg. The cooling boxes were set to a temperature of -7 °C and -18 °C, respectively. -7 °C represented the in-situ temperature at an ice thickness of 3.5 cm. Backup- samples were transported at -18 °C and on dry ice.

Table 2.3 Norut Experiments

Experiment	initial salinity[ppt]	$z_{i,oil}$ [cm]	Paper
Norut I	31.5	8.0	Paper II & III
Norut II	30.5 & 30.6	3.5 & 8.0	Paper IV

2.3 HSVA: Large-scale ship tank experiment

We conducted large-scale oil in ice experiments at the HSVA (Hamburgische Schiffbau- Versuchsanstalt) in the Arctic Environmental Test Basin (AETB). The experiments were performed from 14 March to 4 April 2017, with an entire growth season and a warming cycle simulation. The experiment aimed to quantify and predict near-surface oil movements and distribution and their impact on near-surface detectability by remote sensing (Petrich et al., 2018). The AETB measures 30x6 m and was filled with a saline solution of 30 gkg^{-1} NaCl mixed with tap water from the pumping station Rothenburgsort to a depth of 1.2 m. Two sections, with dimensions of 16x6 m and 14x6 m were created using a wooden barrier to separate the areas. Columnar ice was grown in the larger section while the smaller area accommodated granular ice growth underlain by columnar ice. The ambient temperature was -12 °C during the ice growth. Over two days of ice growth, an airflow created by six centrifugal fans (WDH-AB 10) was forced over the water surface, creating turbulence and allowing granular ice to form. Additionally, we submerged cardboard tubes before the onset of freezing into the granular and columnar division of the test basin. The cardboard tubes were mounted on a wooden rack to hold them in place and facilitated simulated oil spills with iodine-doped crude oil. Iodine increases the x-ray absorption of oil, simplifying later oil segmentation of μ-CT scans. The cardboard tubes had an inner diameter of 7.8 cm (outer diameter of 8.2 cm) and a length of 50 cm.

Ten days after the ambient temperature was reduced to -12 °C, the ice reached a thickness of approximately 13.6-17.2 cm. At this point, Styrofoam patches were placed on top of the ice, reducing the sea ice growth and creating under-ice cavities. After two days after the insulation was removed in order to allow the ice temperature to equilibrate overnight and oil injection experiments were carried out the following day. 5400-7600 mL of Troll B crude oil was injected into the medium sized cavities of approximately 1 m in diameter. To ensure oil encapsulation by ice forming underneath the simulated oil spill, the ambient temperature was maintained at -12 °C for three more days. Four days after oil injection, the ambient temperature was gradually increased to -6 °C and six days after the injection to -2 °C. After each temperature adjustment, the ice had a minimum of 14 hours to thermally equilibrate before sampling. Ice samples containing incorporated oil were sampled from day one after the oil injection until the end of the experiment. We sampled using a Kovacs core barrel (7.2 cm in diameter). The ice cores were subsampled on-site to a height of 5-7 cm with a handsaw and packed in plastic containers filled with cooling liquid (RT-9HC and RT-4HC from Rubitherm Phase Change Material, based on Paraffins (petroleum), normal C5-20. The cooling liquid was pre-cooled to avoid excessive oil leakage. Furthermore, to this end the samples were transported to NTNU at -20° C.

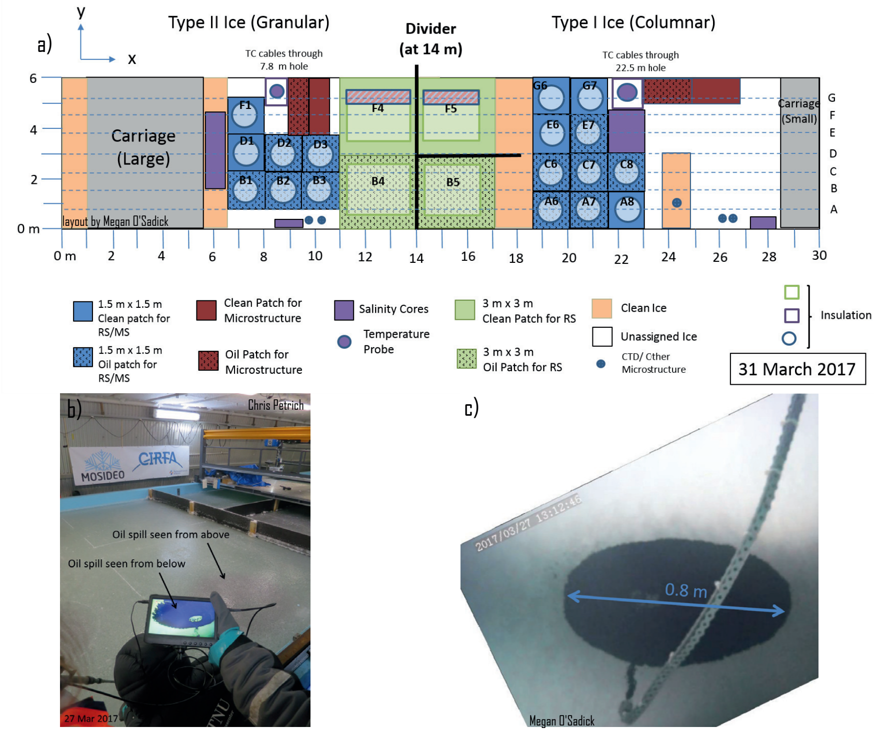

Fig. 2.3 Large-scale ship tank settings from Petrich et al. (2018). a) Schematic top view of the experimental set-up. To the left of the divider mixed ice type growth, with granular ice on top underlain by columnar ice. To the right of the divider columnar ice type. Blue sections represent the areas of clean ice and oil spills with non-doped oil injected. The dark red patches show the areas with installed cardboard tubes injected with iodine-doped oil. b) shows an image of the oil injection. The oil spill seen from the top, shining through the ice and from underneath seen through an underwater camera. c) Oil injected into an under-ice cavity seen through an underwater camera.

Chapter 3

Sea ice microstructure investigations and evolution

Nothing is constant except change. (Heraclitus Ephesus)

This chapter summarises the analysis, and results of experimental field data on the pore structure evolution of young sea ice, collected in Van Mijenfjorden (Svalbard) in spring 2016. The experimental data, including macroscopic investigations such as salinity, density, and temperature, as well as microscopic observations of the brine- and air- pore sizes, connectivity and number, is presented in its full length in *Part II (Paper I).*

3.1 Introduction

Initial sea ice structure studies are mainly based on 2-D macroscopic observations (cm-mm scale). The descriptions were mostly made on vertical or horizontal thick- and thinsections, which required destructive preparation. In the 1970s, Lake and Lewis (1970) provided the first 3-dimensional insight into brine channel systems through a detailed study on sections from an ice block of ca. 2x2x1.5 m and a weight of 5900 kg. Since then several optical studies on the description of sea ice microstructure using petrographic methods have been published (e.g., Lange, 1988; Perovich and Gow, 1991, 1996; Light et al., 2003). A detailed 2- D study of single brine inclusions was conducted by Sinha (1977) who implemented a dual observation method using a polarized- and a scanning electron microscope. Investigations on the sea ice pore fluids and their thermal evolution utilizing magnetic resonance imaging were conducted by Eicken et al. (2000). Kawamura (1988) gave the first 3-D insights into sea ice, employing non-destructive CT, with a resolution of 2 mm. The advances in technology and the use of μ-CT allow us to examine specimens at a much higher resolution and provide an opportunity to deepen our knowledge of the physical properties of sea ice. Brine inclusions, their connectivity and permeability were investigated with μ-CT by Golden et al. (2007) and Pringle et al. (2009), supporting the disconection of the pore space with decreasing temperature. Investigations on the spatial distribution of gas bubbles and gas transport through sea ice were conducted by Crabeck et al. (2016). Observations on natural grown sea ice from μ-CT scans were first reported in 2009 (Maus et al., 2009; Obbard et al., 2009; Lieb-Lappen et al., 2017). The brine volume tend towards thermodynamic equilibrium, and temperature changes alter the sea ice microstructures . To diminish the likelihood of changes occuring within the pore structure in the time between from sampling until imaging, Maus et al. (2009) removed the brine volume fraction by centrifuging the ice specimens. The proposed method was used to obtain cast samples of the sea-ice pore space (Freitag, 1999; Weissenberger et al., 1992). Maus et al. (2009) transported the samples close to their in situ temperature for the field into the lab. Once in the lab, specimens were centrifuged close to their in situ temperature, and the highly mobile brine was removed. The brine removal allowed transportation and imaging of the samples at sub-eutectic temperatures without changes to the pore structure.

This part of the thesis presents the development of young sea ice pore structures obtained in the period 16 March to 23 April 2016. Detailed investigations of the brine network, air inclusions and bulk physical parameters, including sea ice temperature, salinity, density, porosity, pore- and throat- size and pore number per area, are reported. Hydrostatic density- measurements were compared with sea ice density derived from μ-CT observations. Salinity derived from conductivity was collated with salinity deduced from ϕ_b observed from μCT scans.

3.2 Methods

3.2.1 Laboratory setup

The **bulk salinity** (S_{ice}) was measured on melted samples, utilising a conductivity/salinity meter from Hanna instruments (HI 98 188). Salinity was measured in psu.

The sea ice **bulk density** of sea ice (ρ_{bulk}) was measured by hydrostatic weighing of samples in paraffin (Fritidsparafin: Wilhelmsen Chemicals) (Nakawo, 1980; Kulyakhtin et al., 2013; Pustogvar and Kulyakhtin, 2016). Sample weight was determined in air (W_{air}) and the submerged sample weight (W_{par}) as well as the measured paraffin density (ρ_{par}) to calculate ρ_{bulk} after Equation 3.1.

$$\rho_{bulk} = \frac{W_{air}}{W_{air} - W_{par}} * \rho_{par} \tag{3.1}$$

We used the measured bulk density and salinity to calculate ϕ_{air} after Cox and Weeks (1982) (Equation: 3.2).

$$\phi_{air} = 1 - \frac{\rho_{bulk}}{\rho_{ice}} + \rho_{bulk} * S_{ice} * \frac{F_2(T)}{F_1(T)} \tag{3.2}$$

The samples collected for **microstructure analysis** were removed from the conical plastic containers used to transport the samples from the field to the laboratory. The salinity of the brine that had accumulated during transport was measured (S_{bdrip}). Microstructure samples were weighed (PCE Group, BT 2000) and reduced to a diameter of 4 cm.The waste accumulated during the trimming of the samples was retained for salinity measurements (S_{rest}). Samples for pore structure analysis were centrifuged at a temperature of -3 °C and 900 revolutions per minute (40 G) for 10 minutes to remove the mobile brine. The salinity of the brine removed during centrifuging was measured (S_{bcent}). Centrifuged samples were packed in plastic bags prior to storage and transported at -15 °C from the laboratory of UNIS to NTNU, where the pore structure analysis by μ-CT scanning were conducted. Following scanning, the sample was melted and the salinity was determined (S_{cent}).

3.2.2 μ-CT imaging and post imaging processing

3-D X-ray micro-computedtomographic imaging of collected samples was performed at the Norwegian Centre for X-ray Diffraction, Scattering and Imaging (RECX), NTNU using an XT H 225 ST micro-CT system (Nikon Metrology NV). The CT was equipped with a Perkin Elmer 1620 flat panel detector (2048 × 2018 pixel field of view). Scanning was executed with 3142 rotation per 360°, an exposure time of 708.00 ms at 250 μA, an acceleration voltage of 150 kV and tungsten (W) was chosen as the target material. Diverse settings, including different targets (W, Mo, Ag, Cu), currents, acceleration voltage, and exposure time, were tested before acquiring the whole data set. W and Mo with a current of 150 kV and an acceleration voltage of 260 μA or 250 μA and 3142 projections gave the best results regarding the noise to signal ratio and the sharpest phase transition for the objects of interest (air and brine inclusions). The acquisition using Mo target took longer and provided only minor improvement to the image quality. Therefore W was chosen. The images were scanned with a voxel edge length of 25 μm. Reconstruction was conducted using the Nikon Metrology XT Software. Beam hardening [1] correction was applied during reconstruction, and data were stored as 16-bit grey value stacks. For the scans, an alumina sample holder (1 mm wall thickness) was used and scans were performed at -15°C. The scanning temperature was maintained by a self-assembled cooling system consisting of two thermoelectric assemblies (www.lairdtech.com).

Reconstructed data stacks were processed using ImageJ (Schneider et al., 2012). The images were cropped to a cross-section of 1150x1150 pixels and an average of 400-650 pixels in height. The sample holder and scattering on the top and bottom were cut out of the field of view (FOV). A filter combination of a Median filter (radius: 2 voxels) and a Gaussian filter (radius: 1.5 voxels) was applied to the cropped scans. Next, the grey values within the CT images were segmented into three signals: ice, air and brine. To differentiation between the ice and air signal Otsu's algorithm (Otsu, 1979; Maus et al., 2015) was applied. Air segmentation was conducted in a semi-automated procedure: Five sub-areas were chosen which contained a similar amount of ice and air and Otsu's algorithm was applied. The mean of the Otsu derived threshold from the subareas was selected as the air threshold. The brine threshold was determined by the Triangle algorithm (Zack et al., 1977), since the Otsu threshold gave too high brine volume fractions. The brine threshold was estimated on a selection of 41 samples. Five subregions, including an equal amount of brine and ice, were visually chosen. Based on the investigation of the 41 selected samples, we observed a correlation between the ice peak and the brine threshold. The brine threshold was set following the ice peak. The ratio of brine threshold determined with the Triangle algorithm to ice peak was 1.13 (±0.03). The brine segmentation in this study is based on that factor and was set following the ice peak (Figure: 3.1).

3.2.3 Pore space analysis

Porosity metrics

GeoDict 2018 and 2019 (Linden et al., 2018) was used to determine in situ brine porosity $\phi_b^{'}$ and the air porosity $\phi_{air}^{'}$. ϕ_b can be further specified into the open brine porosity $\phi_{bopen}^{'}$, the connected brine porosity $\phi_{bcon}^{'}$ and the closed brine porosity $\phi_{bclosed}^{'}$.

The fractions of open and closed pores were determined in GeoDict concerning the six faces of a 3-D image. The x-axis and the y-axis span the horizontal cross-sectional plane, and the z-axis defines the vertical direction. An open pore is connected to any of the sample surfaces. A closed pore is isolated and locked from the surfaces. The connected porosity is a sub-set of the open porosity and was determined through the access of the open pores from the different faces in the z-direction. The pore fraction opened either to the upper surface z+ (ϕ_{z+}) or the lower surface z $-(\phi_{z-})$ were summed up. In this manner, some of the pores were counted twice. Consequently, the pore fraction accessed from both z+ and z $-(\varphi_{z\pm})$ were accounted for and subtracted from the sum of the porosity reached from either top or bottom as expressed in Equation 3.3. Applying Equation 3.3 on the example

---

[1] Beam hardening: When polychromatic radiation is applied, beam hardening occurs. The lower-energy photons are consumed faster than the higher-energy photons when the beam penetrates a sample. The result is an average increasing photon energy of the beam with distance ("hardening").

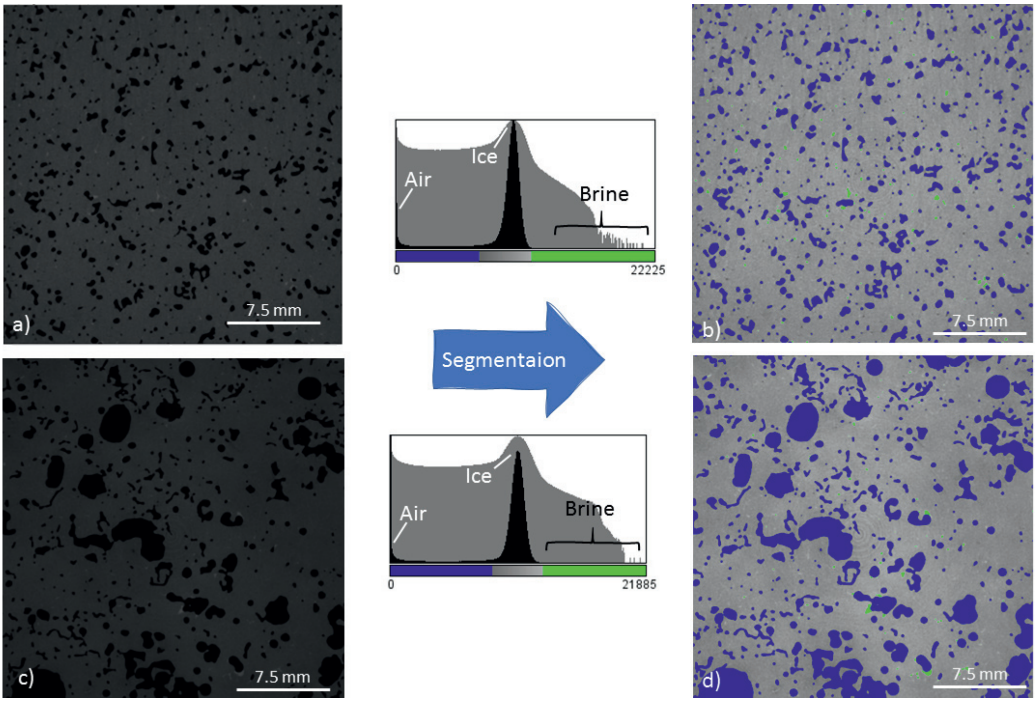

Fig. 3.1 Filtered greyscale μ-CT scans (horizontal) for a) a sample with a small number of macropores and c) a large number of macropores. Filtered data are segmented into air (blue), brine (green) and ice (grey). The histograms in the middle show the linear grey value distribution in black and the logarithmic distribution in grey with a significant ice peak. b)& d) present segmented image slices. From Salomon et al. (2021)

given in Figure 3.2 results in one connected pore. In more detail, two air pores are reached from z+, three air pores from z−and four pores are opened in the z± direction, resulting in one interconnected pore.

$$\varphi_{con} = \varphi_{z+} + \varphi_{z-} - \varphi_{z\pm} \tag{3.3}$$

Since the samples were centrifuged before imaging, the segmented output from the CT images needs to be reinterpreted. The received output from the imaged samples was ϕ^{CT}_{brine}, which consists of the residual brine and solid salt that remained in the ice sample after centrifuging. ϕ^{CT}_{air} inclued all imaged air-filled voids. ϕ^{CT}_{air} is composed of disconnected air pockets and centrifuged brine pores. We assumed that all the open air porosity found in the CT- images ($\phi^{CT}_{airopen}$) originated from centrifuged brine pores. Further, we supposed that the closed air pores ($\phi^{CT}_{airclosed}$) correspond to the original air porosity in the ice sample before centrifuging. Since the connected pore space is a part of the open pore space, ϕ^{CT}_{aircon} is associated with the connected brine pore space.

The μ-CT derived porosities are related to the in situ pore metrics as illustrated in Figure: 3.2, where the prime denotes the μ-CT imaged derived in situ properties. $\phi^{CT}_{airopen}$ is associated with the μ-CT derived in situ property of open brine (ϕ'_{bopen}). ϕ'_{bopen} pores were open brine filled pores under in situ conditions and emptied during centrifuging. The connected air space (ϕ^{CT}_{aircon}) found in the μ-CT analyses relates to connected brine space (ϕ'_{bcon}) under in situ condiciont. ϕ'_{bcon} is a part of ϕ'_{bopen}. The disconnected brine space observed in the

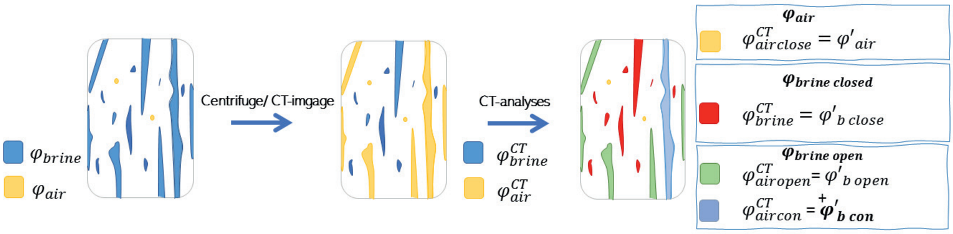

Fig. 3.2 Classification of pores under in situ conditions to the left, after centrifuging in the middle, and after μ-CT image analysis to the right. ϕ_{brine} and ϕ_{air} present the in situ brine, and air porosity. After centrifugation air porosity is given by ϕ^{CT}_{air} and the brine porosity by ϕ^{CT}_{brine}. In the the μ-CT images the air volume fraction can be distinugished in $\phi^{CT}_{airclosed}$ interpreted as in situ air porosity ϕ'_{air}, $\phi^{CT}_{airopen}$ interpreted as in situ open brine porosity ϕ'_{bopen}, and ϕ^{CT}_{aircon} interpreted as in sity connected brine porosity ϕ'_{bcon}. The brine ϕCT_{brine} observed in the CT images is interpreted as in situ closed brine porosity $\phi'_{bclosed}$. From Salomon et al. (2021).

μ-CT images (ϕ^{CT}_{brine}) corresponds to the closed brine porosity ($\phi'_{bclosed}$) under in situ conditions. The total in situ brine porosity (ϕ'_{b}) comprises the sum ϕ'_{bopen} and $\phi'_{bclosed}$. However, as μ-CT acquisition was performed below in situ temperatures, $\phi'_{bclosed}$ needs to be converted by the factor $f(T, T_{CT})$, where T represents in situ temperature and T_{CT} denotes the centrifugation temperature. To calculate the conversion factor of the brine volume at different temperatures Equation 3.4 from Cox and Weeks (1982) was used, i.e. $f = \frac{F1(T_{CT})}{F1(T)}$.

$$F_1(T) = \rho_{brine} S_b (1 + k) \tag{3.4}$$

While the conversion factor is solely valid for the brine volume, one needs to make a minor correction since the μ-CT imaged brine fraction contains undetected solid salt crystals. f was divided by F_{SS} to account for the solid salt volume at T_{CT} of -15 °C. F_{SS} describes the factor to calculate the solid salt fraction from the brine volume fraction at -15°C and is calculated as shown in Equation 3.5.

$$F_{SS} = (C(T_{CT}) + 1) * \frac{\rho_{brine}(T_{CT}) - \rho_{ss}(T_{CT})}{\rho_{brine}(T_{CT})}, \tag{3.5}$$

where C describes the temperature-dependent ratio of the mass of solid salt to the mass of brine Cox and Weeks (1982), column 4 in Table 1. ρ_{brine} is the brine density and ρ_{SS} the solid salt density at centrifuging temperature T_{CT}. At our imaging temperature C was $41.69 * 10^{-3}$ and thus $F_{SS} = 1.031(\pm 0.03)$.

Bulk salinity and density calculation from CT derived porosity

Based on the porosity metrics determined from segmented μ-CT images, we calculated the bulk salinity in psu after Equation 3.6.

$$S_{CT} = \frac{\phi'_b \rho_{brine}(T) S_b(T)}{\rho_{bulk}}, \tag{3.6}$$

where ρ_{brine} is the brine density and S_b is the brine salinity at temperature T. The bulk sea ice density ρ_{bulk} was calculated after Equation 3.7.

$$\rho_{CT} = \rho_{air} * \phi'_{air} + \rho_b * \phi'_b + \rho_{ice} * (1 - \phi'_b - \phi'_{air}) \tag{3.7}$$

where ρ_{air} is the air density and ρ_{ice} the ice density.

Pore sizes

The pore size distribution (granulometry) and the throat size distribution (porosimetry) describe characteristic length scales of the pore space.

- The pore size distribution (granulometry) (Figure: 3.3 b) was determined by fitting spheres of different sizes into every single point of the pore volume. A point was classified by the diameter of the largest sphere that fits in the pore around it. The frequency of sphere diameters was binned into classes of 1 voxel (25 μm). The pore size distribution was determined for ϕ'_{air}, ϕ'_{bopen} and $\phi'_{bclosed}$ (Salomon et al., 2021).
- The throat size distribution (porosimetry) (Figure: 3.3 c) considers the connectivity and the connection size for the open pore space. Spheres were injected from the surfaces, and any point was classified by the largest sphere that can reach it via any path. For example, a larger pore reached via a bottleneck would be assigned the size of the bottleneck. Porosimetry was determined by considering injections from all sample surfaces and binned into classes of 1 voxel (25 μm). The approach is comparable to laboratory tests known as Mercury Intrusion Porosimetry (MIP) or Liquid Extrusion Porosimetry (LEP), yet it is a virtual measurement. Using MIP and LEP, a non-wetting fluid or gas is pressed through the pore space while measuring the absorbed volume and the applied pressure (Salomon et al., 2021).

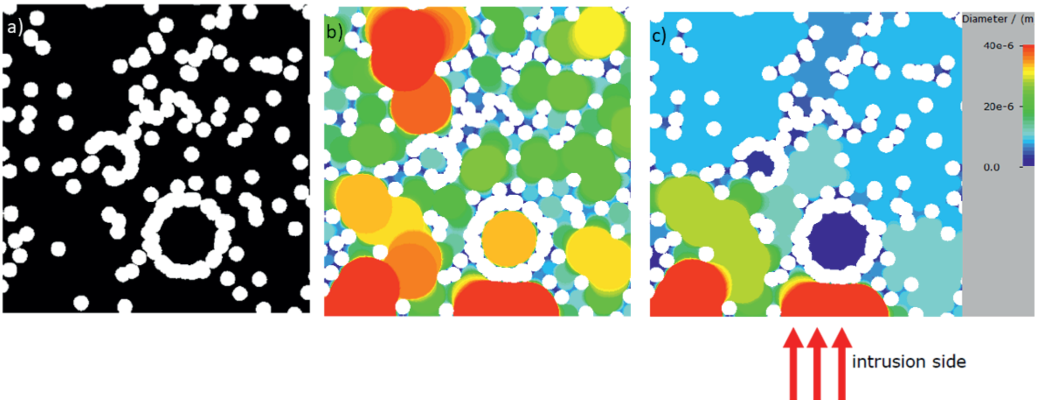

Fig. 3.3 Granulometry and porosimetry used to calculate the pore, and throat size distribution, respectively. a) Shows a structure with the solid material in white and the pore space in black. b) Granulometry: shows the same structure with coloured pore volume. The red volume describes the pore diameters around 40 μm and larger, green areas represent diameters around 20 μm and the blue coloured area below 15 μm. c) Porosimetry: structure shown in a gets penetrated with a non-wetting fluid, indicated by the red arrows. Pores found by porosimetry must be connected to the non-wetting phase. From Linden et al. (2018).

Statistical analysis of the pore space

Statistical analysis of the pore and throat size distribution were conducted in MatlabR2017b and R2019b. The pore and throat sizes were classified into micropores <700 μm, and macropores > 700 μm. A value of 700 μm was chosen since this corresponds to the brine layer spacing at moderate growth rates (0.5 to 2.0 cm day^{-1}) (Weeks, 2010; Shokr and Sinha, 2015; Maus, 2020). An average sea ice growth rate of 0.3 to 1.0 cm day^{-1} was observed, which compares well with the typical growth rate of 0.5 to 2.0 cm day^{-1} for the upper 35 to 40 cm of the ice collected throughout the field campaign. Macro pores were interpreted as secondary pores formed by the connection of the primary brine layers. Freitag (1999) applied a similar classification, yet he classified pores < 1 mm as micropores. Presented pore and throat size distributions are smoothed with a running mean over three pore classes. The distribution per sampling day was based on the average of two cores.

3.3 Results and Discussion

3.3.1 Sea ice bulk properties

Ice thickness

The average ice thickness increased from 35.6 cm on 17 March to 46.3 cm on 26 April. The calculated growth rate throughout the experiment varied between 0.3 to 1.0 cm day^{-1}.The boundary between columnar and granular ice was distinguished on vertical μ-CT reconstructions (Figure: 3.4). Markers for the transition were elongated inclusions in the vertical for columnar ice and randomly orientated inclusions for granular ice. The granular-columnar boundary constantly moved into bigger depths from 4 to 8 cm with respect to the sea ice surface from 30 March towards 12 April. On 23 April, the boundary was found at a depth of 7 cm. We observed that snow infiltrated ice was accumulating on top of the sea ice throughout the field campaign, thus the granular ice layer increased.

Temperature

The mean air temperature during the experimental period was -11.1 °C. The minimum temperature was -29.2 °C measured on 21 March, and the observed maximum air temperature was 0.1 °C observed on 23 April. The coldest sampling day was 17 March, with an average measured air temperature of -20.2 °C. The warmest sampling day was 23 April, with an average air temperature of -0.5 °C (Figure: 3.5). Observed sea ice temperatures showed little variation and fluctuated, at any level in the ice, by less than 0.5 K over the whole sampling period. The temperature gradient over the sea ice depth was relatively weak, allowing transport and centrifugation of the ice close to its in situ temperature with limited logistics. The centrifuge temperature, computed from S_{bcent} was systematically by an average of 0.7 °C higher than the sea ice in situ temperature. The largest temperature differences between the centrifugaton and the in situ temperature was observed in the upper- and lowermost subcores. This is related to different causes, described as followed.

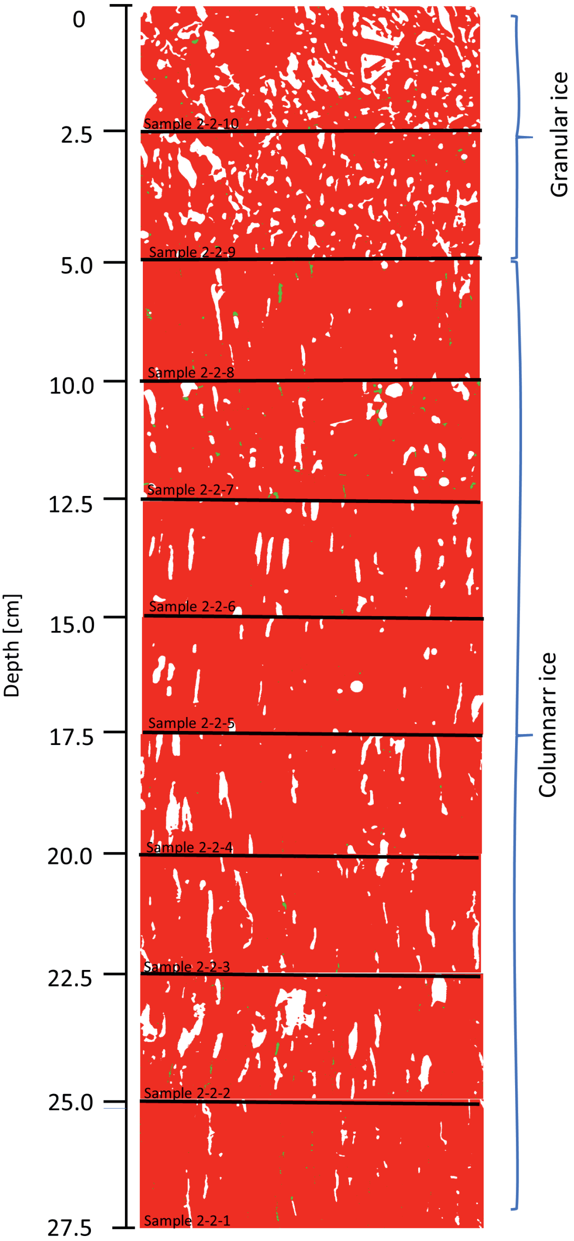

Fig. 3.4 Vertical μ-CT reconstructions, showing ice in red, brine in green and air in white. Elongated, vertical oriented air inclusions (centrifuged brine) from sample 2-2-9 and downwards indicate columnar sea ice. Sample 2-2-10 and 2-2-9 show a random pattern of air inclusions and are therefore interpreted as granular sea ice. From Salomon et al. (2021)

- Scooter-based transport of samples in mobile freezers showed that the temperature control suffered from rapid changes in environmental conditions and that the nominal temperature accuracy of ±0.5 K was not met.
- The temperature stability in the centrifuge.

The overall higher processing temperature in comparison to the in situ temperature had to be taken into account in the interpretation of the brine volume fraction and all parameters associated.

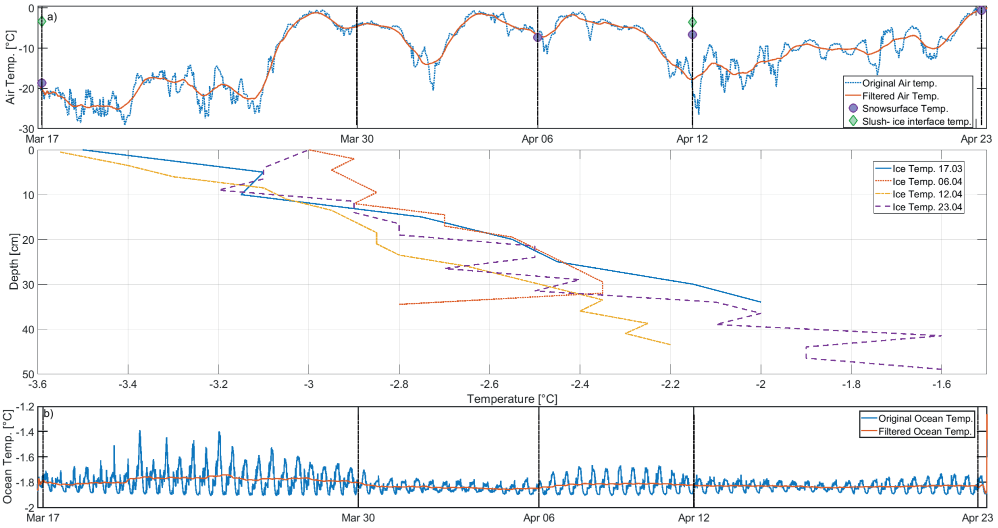

Fig. 3.5 Air, ice and ocean temperatures over the course of the fieldwork period from 17 March to 23 March 2016. a) Blue line represents the original air temperature data, measured every hour from The Norwegian Meteorological institute at Sveagruva målestasjon (99760) 9 m a.s.l. The red line shows air temperature data from the same source, filtered by a moving mean with an interval of 24 hours. b) Sea ice temperature profiles over the course of the fieldwork period from 17 March to 23 April 2016. In dark blue the temperature profile for 17 March is shown, the red dotted line represents temperature measurements for the 06 April, temperature profile for 12 April is presented as the yellow line and the purple dashed line presents the temperature profile from 23 April. Measured snow surface temperature is presented as purple circles, snow-slush interface temperature is represented as green diamonds. c) Ocean temperature measured at a depth of 1.2 meter (0.7-0.8 meter below the ice) is plotted in blue. The red line represents filtered data with a running mean of 24 hours. From Salomon et al. (2021)

Salinity

The salinity profiles based on measured conductivity (S_{con} were investigated Figure:3.6a-e, blue line), as well as the salinity derived from ϕ_b' observed on μ-CT scans (S_{CT},Figure:3.6a-e, red line). S_{CT} calculated from porosity values at centrifuging temperature (mean -2.0 °C). The salinity profiles based on the presented methods largely coincided, where S_{CT} was smaller than S_{con} in the lower half of the ice. Averaged vertical salinity values over time were consistent. An average S_{con} of 6.7 psu (± 2.1 psu), and S_{CT} of 6.1 psu (±4.2 psu) was observed. The comparison of vertical profiles on S_{con} and S_{CT} broadly agreed, yet they were considerably scattered. It was noticeable that all μ-CT cores were slightly shorter than the salinity cores since the weak skeletal layer was destroyed during the cutting process. Deviations of S_{CT} in comparison to S_{con} can be explained as follows:

- The natural variability between two different cores and the fact that S_{CT} was based on an approximately 10 times smaller volumes than S_{con}, may have contributed to the observed differences Gough et al. (2012).
- An underestimation of S_{CT} was attributed to the resolution limitations in the μ-CT scans. Objects smaller than two times the voxel size of 25 μm pixel were not sufficiently resolved and might have appeared as mixed pixels (Nyquist–Shannon theorem).
- Erroneous brine segmentation due to the similar signal of brine to mixed air-brine pixels account for uncertainties of 1 % in the closed brine volume fraction ($\phi'_{bclosed}$) (Maus, 2020). Consequently at a total brine volume fraction (ϕ'_b) of 10-20 % a salinity change by 5–10% or 0.3–0.7 psu can be expected. The observed difference of −0.5 to + 0.8 psu between S_{con} and S_{CT} lays within the error expected from image analysis and the resolution limit of brine pore detection.
- Consistently lower S_{CT} in the lower parts of the ice core may be related to brine loss during sampling. One would expect that S_{CT} derived from ϕ'_{bopen} was not affected by brine loss, as the derivation accounts for the centrifuged brine. But since the assumed S_{bcent} (considering the loss of brine during sampling and transport) would be lower than the in situ values, the calculated S_{CT} based on equation 3.6 was affected, resulting in an underestimation. Maus et al. (2020) concluded that during similar storage and transport procedures, 28% of the total connected brine leaked before centrifugation.
- In the upper part of the salinity profiles-in the freeboard S_{CT} was overestimated in comparison to S_{con}. In this part, sea ice drained naturally before sampling, leaving many connected pores empty. As described earlier $\phi^{CT}_{airopen}$ was interpreted as ϕ'_{bopen} in the μ-CT analyses, thus S_{CT} was overestimated.

Density

The hydrostatic evaluated density (ρ_{hydro}, figure 3.6f-j, blue line) was compared to the density calculated based on ϕ'_{air} and ϕ'_b (ρ_{CT}, Figure 3.6f-j, red line). ρ_{hydro} was performed at -2.7 °C for samples from 17 March and 30 March and at -15 °C for the samples from April. ρ_{CT} was calculated at the same temperature as ρ_{hydro}. ρ_{hydro} of 17 March was calculated after Cox and Weeks (1982) since problems in the cooling chain destroyed the cores for the pore structure analysis. The overall average ρ_{hydro} was 900.5 kgm^{-3} (± 21.6 kgm^{-3}). In comparison, the average ρ_{CT} was 911.8 kgm^{-3} with a standard deviation of 9.8 kgm^{-3}. ρ_{CT} was on average 11.3 kgm^{-3} larger than ρ_{hydro} (± 4.4 kgm^{-3}). The difference appeared systematically over the ice depth, where the upper 10 cm showed a higher ρ_{CT} than ρ_{hydro}, with differences of up to 20-80 kgm^{-3}. The upper part of the sea ice included the freeboard and ice formed from snow. Below 10-15 cm from the sea ice surface ρ_{CT} (range lower 15 cm: 896 - 962 kgm^{-3} were similar or slightly higher than ρ_{hydro} (range lower 15 cm: 895 - 926 kgm^{-3}). Differences for ρ_{CT} in comparison with ρ_{hydro} in the upper part were explained as follows:

- ρ_{CT} was based on ϕ'_{air} and ϕ'_{brine}, and since the entire open air-filled space on CT images was assumed to be brine filled under in situ conditions, ρ_{CT} was overestimated. The correct value at the surface is thus ρ_{hydro}.
- Transport and centrifuging temperatures were higher than the in situ temperature for samples from the upper part of the sea ice cover and lower for the samples near the sea ice bottom. Incongruity in temperatures may result in lower ρ_{CT} closer to the bottom, and larger ρ_{CT} close to the top.

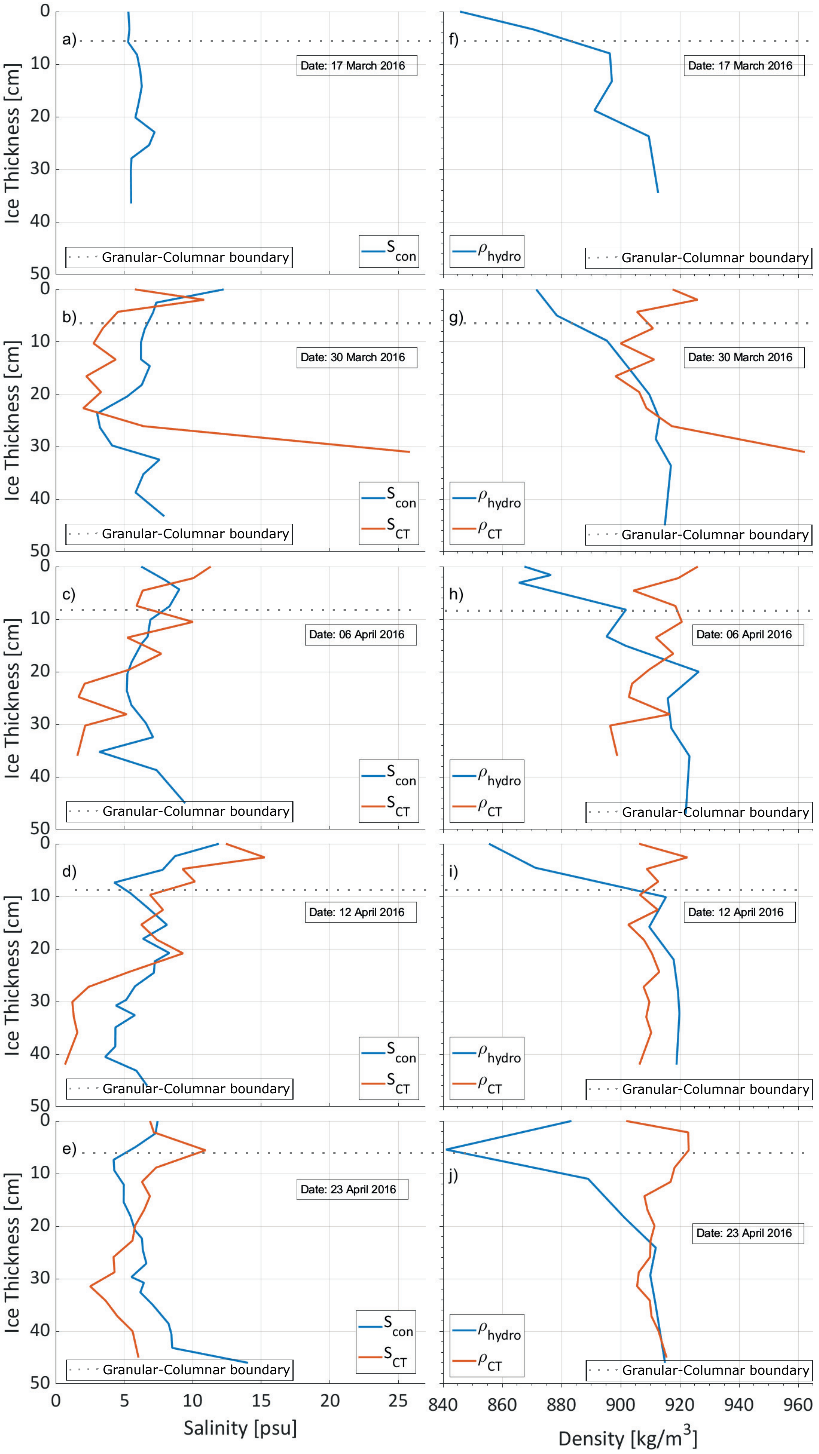

Fig. 3.6 Depth proflies of salinity in psu (a-e) and density in kgm^{-3} (f-j) plotted for the period from 17 March to 23 April 2016. 0 cm depth represents the top sea ice surface.. a-e) Blue line represents conductivity measured salinity S_{con} and red depicts the calculated salinity from porosity observed in μ-CT scans S_{CT} at centrifuging temperature. f-j) Blue line represents measurements from hydrostatic weighing ρ_{hydro} and the red line presents calculated density from μ-CT data ρ_{CT}.ρ_{hydro} and ρ_{CT} at -2.7 °C for the 17 and 30 March and at -15 °C for the sampling days in April. From Salomon et al. (2021).

Porosity

The air porosity based on μ-CT scans (ϕ'_{air}, Figure 3.7 b-e,in red) was compared to the estimated air porosity evaluated from hydrostatic density measurements (ϕ_{aircal}, Figure 3.7 a-e, in blue). The two compared methods were largely consistent, with an exception in the upper 10-15 cm where ϕ_{aircal} was considerably larger than ϕ'_{air}. In the upper part of the ice ϕ_{aircal} reached values from 3-9 vol.%, whereas the average ϕ_{aircal} was 2.6 vol.% (±2.0 vol.%). ϕ_{aircal} was in average by 0.8 vol.% (± 0.6 vol.%) larger than ϕ'_{air}. ϕ'_{air} showed a mean value of 1.6 vol.% with a standard deviation of 0.6 vol%. An underetimation of ϕ'_{air} was assumed in the upper part of the sea ice cover. In the upper sea ice cover the freeboard was found, and infiltrated snow metamorphism to ice. Since, the entire detected open air porosity was interpeted as ϕ'_{bopen}, ϕ'_{air} was underestimated . However, ϕ'_{air} is valid for ice below the freeboard. Comparison of ϕ_{aircal} with ϕ'_{air} (excluding the top 15 cm) show that ϕ'_{air} was by a mean of 0.4 vol % smaller (±0.5 vol%). This difference may have resulted from natural variability as well as from resolution limitations.

Brine porosity measurements based on μ-CT scans (ϕ'_{b}, Figure 3.7 g-j,in red) at a mean centrifuging temperature of -2.0 °C were compared to brine porosity calculations based on salinity measurements (ϕ_{bcal}, Figure 3.7 f-j,in blue) at in situ temperature. The connected brine porosity (ϕ'_{bcon}) a part of ϕ'_{b} is depicted in yellow. ϕ'_{b} showed a mean of 17.8 vol.% (± 11.4 vol. %) at centrifuging temperature (mean -2.0 °C). ϕ'_{bcon} contributed to approximately two thirds of ϕ'_{b}. The mean ϕ'_{bcon} was 12.2 vol.% (±10.2 vol %). ϕ'_{bcon} corresponds to the vertically connected brine porosity fraction of ϕ'_{bopen} which showed a mean of 14.8 vol. % (± 10.0 vol. %). An almost linear increase in ϕ'_{bcon} with the total brine porosity ϕ'_{b} was observed. Vertically connected brine pores were not found once the total brine porosity dropped below 3 %. As well as for ϕ'_{bcon} an almost linear increase of ϕ'_{bopen} was observed depending on ϕ'_{b}.

3.3.2 Pore characteristics

Pore number density

Anlayses of the open brine channel number resulted in 5 to 50 pores cm^{-2}.An increase in the number of open brine channels in the bottom 5 cm was observed, apart from that no pronounced depth dependence was distinguished. Furthermore, a decrease in connected brine pores throughout the fieldwork period was seen. A negative correlation between the open pore number with the total brine porosity ϕ'_{b} with a R^2 of 0.2 was observed i.e. the open pore number decreased slightly with an increase in ϕ'_{b}. The number density of closed brine pores mostly fell into the range of 10^3 to 10^4 pores per cm^3 (or 1-10 pores per mm^3). Both an increase of pores towards the top and the bottom was observed. A negative correlation between the closed brine pore number with ϕ'_{b} with a R^2 of 0.04 was observed. These data can be compared to the reported pore statistics from Light et al. (2003) and Perovich and Gow (1996). Light et al. (2003) reported 24 brine pockets per mm^3. The higher number is likely related to the higher imaging resolution (10 μm compared to our 25 μm). Perovich and Gow (1996) detected in their optical analysis of 2-D thin sections (pixel size of: 30 μm) of young sea ice 1-6.9 brine pockets per mm^3. Furthermore, they observed a decrease in brine pockets at higher porosities, attributed to the coalescence of pores. In the porosity range of 3 to 20 %, they saw an increase in the number of brine pockets associated with increased pores of the size that reached the detectability threshold.

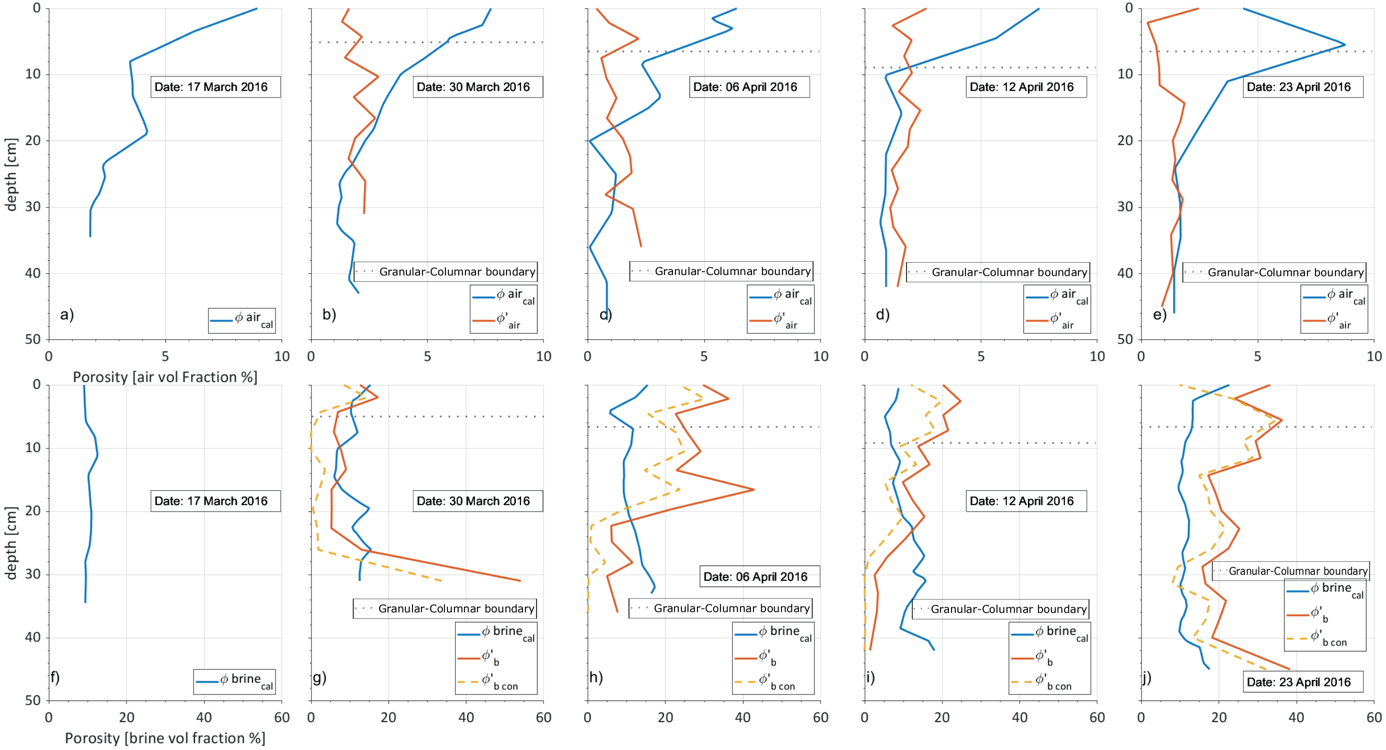

Fig. 3.7 Total air ϕ'_{air}, brine ϕ'_b and connected brine porosity ϕ'_{bcon} in volume fraction % as a function of depth in cm. Where 0 cm depth represents the sea ice surface. The blue line represents theoretical air $\phi_{air_{cal}}$ and brine porosity $\phi_{brine_{cal}}$ according to Cox and Weeks (1982) at in situ temperature. The red line shows porosity data for brine ϕ'_b and air ϕ'_{air} at centrifuging temperature observed from μ-CT images. Yellow line presents connected brine porosity ϕ'_{bcon}. a) Air porosity from 17 March at -2.7 °C, in b) air porosity from the 30 March is shown at -2.7 °C, c) presents air porosity from 06 April at -15 °C, d) shows air porosity from 12 April at -15 °C and e) represents air porosity from 23 April at -15 °C. f) brine porosity from 17 March, in g) brine porosity from the 30 March is shown, h) presents brine porosity from 06 April, i) shows brine porosity from 12 April and j) represents brine porosity from 23 April. From Salomon et al. (2021)

However, we observed a continuous decrease in pore pockets over time from 06 April to 23 April for ϕ'_b from 15 to 50 %. The closed air pore density mostly was in the range of 200 to 1000 per cm^3 (or 0.1 -1 pores per mm^3). With an observed increase towards the top and the bottom. A negative correlation between the closed air pore number with ϕ'_b with a R^2 of 0.1 was observed. A comparison of the results presented here with the study from Light et al. (2003) again shows significantly larger air pocket number in the latter study (1.2 air pockets per mm^3) at higher resolution (10 μm). Hence, the smallest air bubbles were likely not resolved. Yet a decrease of air pockets at high ϕ'_b is observed, which is likely related to the the coalescence of brine pores. Furthermore, the highest number of air bubbles were observed close to the bottom and the top of the sample.

Pore size distribution

The biggest air inclusion was found on 30 March with a pore size of 2575 μm. Most air pores appeared in the size of micropores, and we typically found the mode in the range 200 to 225 μm. The smallest micro and macro pore medians were observed close to the sea ice surface. A positive correlations of the air pore size distribution's median with ϕ'_b and a R^2 of 0.05 was observed. Since the investigated samples were centrifuged only air bubbles within the residual brine and the ice matrix were observed. Moreover, all the samples were scanned at the same temperature (-15 °C), which was below the in situ temperature. As the air bubbles decrease simultaneously with the residual brine volume (Crabeck et al., 2019), little variation in the air pore size was observed in dependence of ϕ'_b (which was centrifuged).

The pore size distribution of the closed brine pore fraction was analysed at -15 °C, and was seen to stretch up to 875 μm. Most closed brine pores found were classified as micropores < 700 μm. Note that investigations on the closed brine pores were restricted by the scanning resolution for scans with a voxel edge length of 25 μm. The indication was given by the pronounced peak in the beginning of the pore size distribution. No significant evolution for the mode and median of $\phi'_{bclosed}$ pore size distribution over time was found. The pore size distribution suggests that around 16% of $\phi'_{bclosed}$ had a diameter of 2 voxel (50 μm) and 13 % had a diameter of 1 voxel (25 μm). To estimate the number of undetected pores, reference data at higher resolutions are needed. Light et al. (2003) (pixel size: 10 μm) observed numerous brine pockets with a length at the resolution limit of 10 μm. Brine inclusions with diameters <50 μm in our study would roughly correspond to the class of brine pockets with lengths <100 μm in Light et al. (2003) Figure 8, containing roughly 3% of ϕ'_b. This comparison suggests an inconsiderable fraction of hidden pockets, in terms of their volume. Nevertheless, Light and others (2003) stated that they could only visualize 2/3 of the conductivity-based brine volume. In general, there is a lack of data on small inclusions.

The open brine pore size distribution ϕ'_{bopen} contained pore sizes up to 7450 μm (Figure 3.8), where the mode was found between 200 and 300 μm. In general, the smallest macro pore median (diameter larger than 300 μm) was observed towards the ocean. The median of ϕ'_{bopen} macro pores increase with ϕ'_b the correlation was given with a R^2 of 0.9. An increase in pore size is expected as the sea ice warms and internal melting occurred, leading to an increase in ϕ'_b and thus widening the pores.

Throat size distribution

The throat size distribution for ϕ'_{bopen} showed a mode of 100 to 200 μm throughout the experiment. The biggest throat had a size of 3825 μm. Similar to the pore size distribution of ϕ'_{bopen} the throat size distribution for ϕ'_{bopen} showed an increase in size correlating with increasing ϕ'_b. The correlation was given with an R^2 of 0.3. The mechanism is the same as described above. The observed mode of the pore size was larger than the mode in the throat size distribution for ϕ'_{bopen}, by a factor of roughly 1.5. Throats above 2 mm in diameter were only found in the upper 7.5 cm at the beginning of the experiment. As the sea ice matured by the end of the experiment, throats larger than 2 mm in diameter were apparent throughout the whole profile. Analysis of the throat size showed that between 0.4 and 3.4 vol % had a diameter larger than 2 mm.

3.4 Conclusion

Microscopic sea ice properties were defined from the process of (i) centrifuging, removal of brine allowing for investigation of the connected and disconnected pore space and (ii) 3-D μ-CT imaging followed by (iii) analysis of the pore size characteristics. The main findings from this study are:

- Density and air porosity determinations based on hydrostatic weighing and μ-CT images below the freeboard are consistent, regarding the measurement accuracy and natural variability.
- μ-CT-based salinity determinations are subject to larger than standard uncertainties due to spatial resolution limitations. The μ-CT-based brine investigation's strength is to distinguish from spatially different porosity metrics, the local distribution, and the differentiation in open, closed and vertically connected brine fractions.
- Vertical variation of the occurrence of open and closed brine pores and closed air pores is remarkably small. Most variation observed was related to changes in the brine porosity.
- Salinity and density, pore sizes and the proportion of secondary (macro) pores remained broadly constant throughout the observation period (16 March to 23 April 2016), while a decrease in the pore number and an increase in pore connectivity over time was observed.
- Confident correlations between the open, connected and the total brine porosity in young sea ice were established. The air pore sizes varied little and the open brine sizes increased with increasing total brine porosity.

Future studies focusing on density measurements on non- centrifuged sea ice samples will be helpful to diminish the observed problems above the freeboard and better understand surface drainage and the evolution of the low-density layer. However, the presented approach provided details on the morphology of the drained low-density surface regime.

Another critical issue for future studies is the scale-dependence of properties (e.g., connectivity, permeability, percolation threshold), which should be addressed by scanning larger samples with a larger FOV at different temperatures.

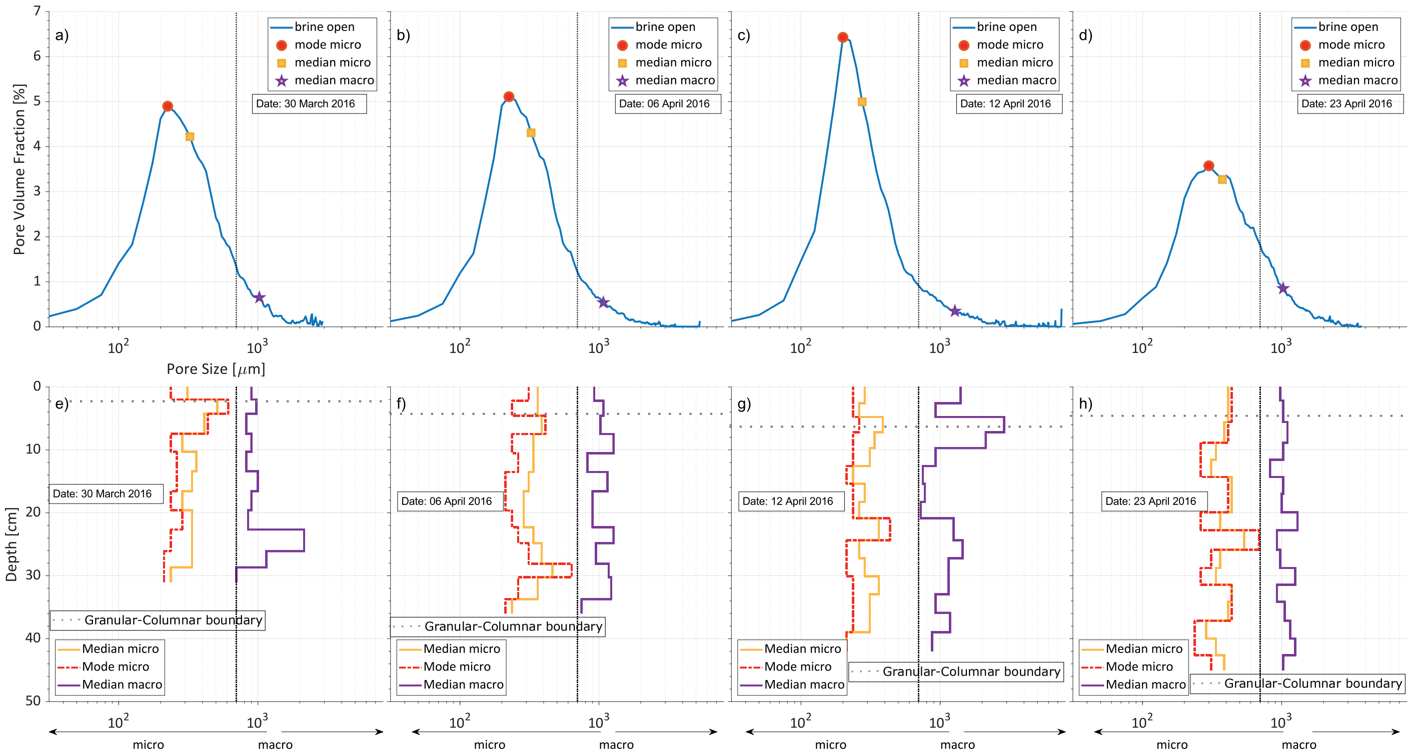

Fig. 3.8 Pore size distribution for the open brine porosity as a function of depth in cm, where 0 cm depth represents the top sea ice surface. a-d) Pore volume fraction for open brine in % plotted against the pore size in μm. The red circle presents the mode, the yellow square marks the median of micropores, and the purple star represents the macro median. e-h) Median and mode for open brine pore size distribution in μm plotted over ice thickness in cm. From Salomon et al. (2021)

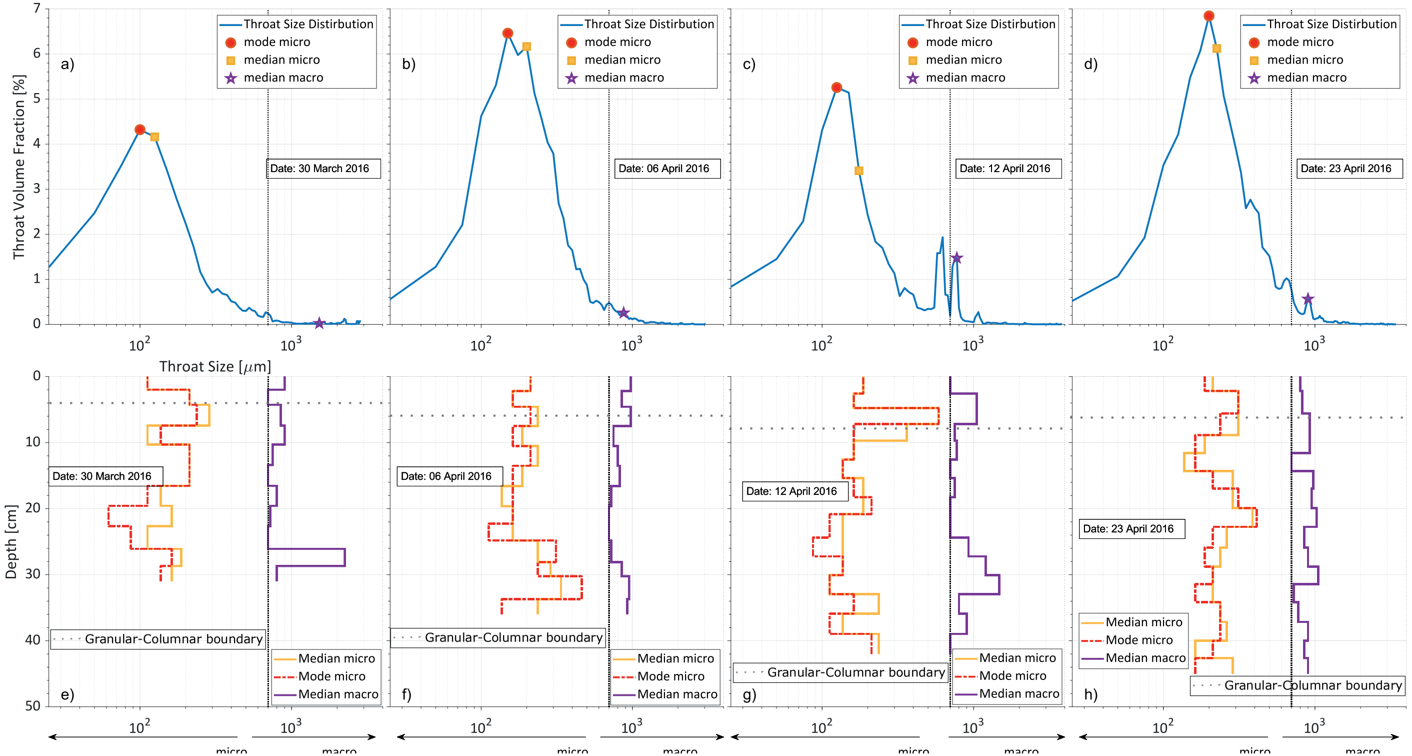

Fig. 3.9 Throat size distribution for the open brine porosity as a function of depth in cm, where 0 represents the top sea ice surface. a-d) Throat volume fraction for open brine in % plotted against the pore size in μm. The red circle presents the mode, the yellow square marks the median of micropores, and the purple star represents the macro median. e-h) Median and Mode for throat size distribution in μm plotted over ice thickness in cm. From Salomon et al. (2021)

Chapter 4

Fate of oil and diesel in sea ice

It took a million years of unprecedented volcanic activity during the Permian to poison the ocean. We have begun to do so again in less than two hundred. (David Attenborough)

This chapter summarises experimental analysis and results on the distribution of oil and diesel within sea ice. It exemplifies different segmentation methods for low absorption contrast materials in CT- images, such as oil and ice. Specimens imaged with μ-CT were segmented either manually by object tracing (*Part II, Paper III*) or by a newly recommended enhanced semi-automated thresholding technique (*Part II, Paper II*). In addition to scans from laboratory-based μ-CT, synchrotron-μ-CT scans are presented (*Part II, Paper IV*). Four different experimental sets are presented (Norut I & II, Svea and HSVA).

4.1 Introduction

The high porosity and permeability of sea ice make it a potential entrapment medium for spilled oil. Previous studies suggest that once oil is spilled underneath a sea ice cover during the sea ice-growth season, the spreading of oil primarily depends on the under-sea ice topography. Oil will collect preferentially in lenses, with a thickness of 0.08- 0.2 m underneath concave depressions (Wilkinson et al., 2015; Glaeser and Vance, 1972; NORCOR Engineering and Research Ltd, 1975). Most of the spilled oil is entrapped in lenses within 12 to 48 hours by continuous ice growth (NORCOR Engineering and Research Ltd, 1975; Buist and Dickins, 1983). Upwards percolation of the oil is limited to the skeletal layer of the ice, where only a minor amount is infiltrated (NORCOR Engineering and Research Ltd, 1975). The sea ice porosity limits the ability of oil penetration (Otsuka et al., 2004; Karlsson et al., 2011). Previous studies determined porosity thresholds between 8 to 15 % and an oil saturation up to 4.5 to 7 mass % were observed (Otsuka et al., 2004; Petrich et al., 2013). Petrich et al. (2013) investigated the potential oil penetration depth and entrained oil volumes. The authors based their study on 1D thermodynamic modelling of salinity and temperature profiles in first-year ice. Depending on the sea ice temperature, they observed an increase in potential penetration depth (0.02 -0.10 m in January to 0.12 - 0.25 m in May for a porosity threshold of 10%). The penetration depth was halved at a porosity threshold of 15 %. The oil entertainment volume was found to increase with sea ice temperatures and ranges from less than 1 up to 5 L/m^2 (Petrich et al., 2013).

Another critical factor determining whether oil will enter the sea ice pore space is the pore size and the dimensions of necking connecting the single pores. The critical pore size depends on the thickness of the oil layer, buoyancy, and capillary pressure. The porous space can be entered once the buoyancy overcomes the capillary pressure. Maus et al. (2015) simulated the oil saturation in sea ice based on the sea ice porosity obtained by CT images. They concluded that buoyancy is too weak to be the driving mechanism for oil to enter young sea ice with a median pore size of 0.15 mm. Moreover, they did not note a porosity threshold for oil to enter the sea ice. It was presumed that oil entrainment depends on several factors such as the permeability, oil layer thickness, convection of brine, and the pore microstructure. In a recent study from Oggier et al. (2019) five phases of oil migration throughout one seasonal cycle were experimentally described:

- Oil saturation of the skeletal layer.

- Oil immobilization as the permeability is low during sea ice growth (some oil can migrate upward in larger channels).
- Mobilization of oil because of melting and warming, as the porosity increased (permeability threshold $\approx 10^{-11} m^2$).
- Invasion of unaffected primary and secondary pore space as ice continues to warm and bulk porosity increases.
- Invasion of granular pore space before complete ice melt.

However, studies on faithfully preserved sea ice samples using X-ray μCT including oil remain a challenge and are rare (Salomon et al., 2017; Desmond et al., 2021). The reason is that the similarity in density and the resulting similar absorption contrast of ice and oil makes the distinction in μ-CT images difficult. Recently Desmond et al. (2021) suggested an enhanced automated segmentation method to detect oil. They used the absorption contrast of the polypropylene tube they used as a sample holder as a benchmark for the oil segmentation. Their observation from the upper part of sea ice (frazil/interfrazil layer) was:

- The major diameter of oil inclusions is less than 1 mm.
- Oil inclusion size does not vary with depth.
- 50 % of the inclusions ranged between 0.1 and 0.2 mm at different imaging temperatures ranging from -15 °C to -4.8 °C at pixel size of 29 μm.
- Sea ice temperature did not affect the size of the oil inclusion.

μ-CT imaging is a powerful tool to interpret the morphological distribution of oil in ice. However, an independent and systematic segmentation process of low absorption contrast phases needs to be developed. To this end, three oil segmentation methods are presented: Object tracing (OT), Semi- automated segmentation (SAS) and Manual segmentation. One of the approaches is a newly suggested semi-automated segmentation routine for low absorption contrast phases such as oil/diesel and ice. The results of the segmented oil amount are compared with reference measurements on melted samples. Furthermore, the oil inclusion morphology and distribution are presented.

4.2 Methods

4.2.1 μ-CT imaging

Four different experimental sets (Norut I & II, Svea and HSVA) were scanned by μ-CT imaging for non-destructive 3-D investigations on the oil distribution within sea ice. The acquisition specifications are summarized in Table 4.1.

The samples acquired during the experiment Norut I were scanned twice, once at the SLF(WSL- Institut für Schnee- und Lawinen Forschung) and another time at NTNU. At SLF, we used a Scanco Medical μ-CT 40 and 80 with a current and peak energy of 177 μA and 45 kV. The detector panel for the Scanco Medical μ-CT 40 had a dimension of 2048 x 256 pixels, while the Scanco Medical μ-CT 80 was equipped with a detector panel of

Table 4.1 Overview of CT- settings

Experiment	Scanner/ Location	Energy	Voxel edge length	Sample diameter
Norut I	XT H 225 ST μ-CT (Nikon Metrology NV)/NTNU	250 μA, 150 kV	25 μm	35 mm
Norut I	Scanco Medical μ-CT 40 & 80 / SLF	177 μA, 45 kV	18 μm	35mm
Norut II	IBL* P05 at PETRA III/ DESY	20 kV	4.9 μm	8.75 mm
Svea	XT H 225 ST μ-CT (Nikon Metrology NV)/NTNU	250 μA,175 kV	49 μm	72 mm
HSVA	XT H 225 ST μ-CT (Nikon Metrology NV)/NTNU	250 μA,175 kV	49 μm	72 mm

*IBL: Image Beam Line at the storage ring Petra III

2048 x 128 pixels. Both systems were operated with 2000 rotations per 360 °. The voxel edge length was 18 μm, and scanning was performed at an ambient temperature of -15°C. Settings for both systems were the same, and no difference in the μ-CT-scans was assumed. At NTNU a XT H 225 ST μ-CT (Nikon Metrology NV) was used at a current of 250 μA and an acceleration voltage of 15 kV to scan the samples from the Norut I experiment at a voxel edge length of 25 μm. The flat panel detector was a Perkin Elmer 1620 with a pixel size of 200 μm x 200 μm and 2048 x 2018 pixels. 3124 radiographs were taken per 360° at an exposure time of 708 ms. The temperature during scanning was -15 °C.

Samples from the Norut II experiment were imaged with synchrotron radiation at the Helmholtz Zentrum Gesthacht P05 imaging beamline at Petra III/ DESY, Hamburg in Germany. Scanning energies that allowed sufficient transmission for phase-contrast imaging were chosen. An energy of 20 kV and a FOV of 7.5 mm x 7.5 mm was used, resulting in a voxel edge length of 2.45 μm. 600-1500 radiographs of 1300x3056 pixel in size at an exposure time of 150-250 ms were acquired per 180°. During reconstruction, voxels were binned two times, giving an effective voxel edge length of 4.9 μm. The samples were scanned in plastic containers, in which they were also transported. Specimens acquired during the Svea and HSVA experiment were imaged at NTNU using an XT H 225 ST μ-CT (Nikon Metrology NV). The samples were scanned at a 250 μA current and peak energy of 175 kV. 3142 rotations per 360° were taken at an exposure time of 500 ms. The FOV was 98 mm x 98 mm, relating to a voxel edge length of 49 μm. Throughout all the scans performed at NTNU, the temperature was controlled by bottom and top cooling with a thermoelectric assembly (www.lairdtech.com). The samples were placed in an aluminium container with a wall thickness of 1 mm during the scans. The data aquired at NTNU was reconstructed using the Nikon Metrology XT software, applied beam hardening correction, and stored data as size 16-bit grey value stacks of 2000x2000x2000 pixels.

4.2.2 Segmentation

The reconstructed images were cropped to the largest possible volume (volume of interest VOI), excluding the sample holder, such that the VOI included only air, brine, ice, and oil. Air and brine segmentation was conducted on filtered images. A filter combination of a Median filter (radius: 2 voxels) and a Gaussian filter (radius: 1.5 voxels) was applied to the VOI. For descriptions of the segmentation of air and brine, the reader is referred to section 3.2.2. Oil segmentation was performed using three different methods. The method presented first is a manual segmentation relying on visual tracing of objects and the second method introduces a three-step semi-automated segmentation. The third segmentation process presented is based on the grey value histogram of the CT- scans and is performed manually.

Object tracing (OT)

Oil inclusions found in μ-CT- scans from the Norut I experiment were segmented using the image analysis software ImageJ (Schneider et al., 2012) by manual performance of the Wand (tracing) Tool. The segmentation was performed on 2D horizontal slices of the filtered 3D VOIs. Therefore an initial pixel (iP) was chosen in every visually detected oil blob. After that, the Wand Tool investigated the grey value of the four adjacent pixels to the iP. It selects the vicinal area under the condition that its grey value falls within a tolerance range and classifies the pixel as the region of interest (ROI). The Wand Tool proceeded similarly with the next neighbouring pixels if the contiguous area was selected. The manual selection of iP was repeated on every 5th to 20th horizontal cross-section and interpolated the ROIs between the 2-D slices, by connecting them with each other.

Semi-automated segmentation (SAS)

The presented approach aims to detect oil via a semi-automated segmentation (SAS). The method consists of 3 processing parts: pre-segmentation-processing, segmentation, and post-segmentation-processing. The processes were applied to selected samples from the Norut I, Svea and HSVA experiment, cropped but non-filtered (further referred to as original images).The brightness gradient towards the CT scan faces in the pre-segmentation processing was compensated for. The segmentation images processed in the pre-segmentation were labelled as ice or oil. In the post-segmentation-processing morphological operations were applied to the segmented oil. Thinner features were connected, and isolated oil inclusions < 10 voxels (for a voxel edge length of 25 μm and 49 μm, respectively 10 voxels correspond to a volume of $1.6*10^{-5}$ mm^3 and $1.2*10^{-4}$ mm^3) were removed.

The **pre-segmentation-processing** was performed to diminish the brightness gradient toward the edges and faces of the CT scans. The process was executed on original images in Matlab2021a and can be subdivided into four steps. The Idun cluster at NTNU (Själander et al., 2019) powered the computational demand of the operations. The pre-segmentation for one sample took around 24 to 72 hours, depending on the sample size.

1. **Masked image**: In the first step, air and brine were excluded by masking. The air threshold was determined with Otsu's algorithm (Otsu, 1979; Maus et al., 2015), whereas the brine threshold was identified according to the ice peak. Brine masking was carried out by determining the ice peak for each slice in the grey value histogram. The brine threshold was found according to ice peak and a determined ratio. For further details on the air and brine threshold, the reader is referred to section 3.2.2. Based on the determined threshold, grey values ≥ brine threshold and grey values ≤ air threshold were set to not a number (NaN) and excluded from further processing steps.
2. **Background image**: From the masked images in step 1, a background image was produced. The background image represented the grey value distribution of the matrix, in this case, ice. The masked images were filtered with a 2-D Median filter ignoring NaN with a kernel size of 99 x 99 pixels. Since median values were computed for the masked areas, these were replaced with NaN in a further step.
3. **Divided image**: In the third step, the brightness gradient within the original images was removed, by dividing the background image by the original image ($\frac{background}{original}$). The division led to an inversion of the oil and ice grey values compared to the original image. As a result, the oil appeared brighter than ice.

4. **Pre-segmented image**: In a fourth step, we applied a combination of a 3D- median and minimum filter with a footprint of 5x5x5 voxels on the divided image stacks. The median filter removed noise while the minimum filter eroded oil clusters smaller than 5x5x5 pixels.

The oil-ice **segmentation** was determined on pre-segmented image stacks in Geodict2021 and 2022 (Linden et al., 2018). The processed images were labelled as either ice or oil, aiming to simplify further analyses. The segmentation was based on the grey value histogram from pre-segmentation-processed images. The threshold was appointed visually right after the ice peak.

In the **post-segmentation-processing** the segmented image stacks were processed in ProcessGeo (Geodict2021 and 2022). Dilatation and Erosion, two morphological operations, were iteratively applied. The sequence of these two operations is known as "opening" and "closing". It had the effect of connecting thin and small oil structures while filling holes at the same time (Stock, 2018; Elmoutaouakkil et al., 2003). First, all pixels segmented as oil were dilated by two voxels, meaning two extra voxels of oil were added at the oil boundaries. Afterwards, the outermost two oil voxels at the oil inclusion boundary were removed by Erosion.We applied Clean (Geodict2021 and 2022) on the dilated and eroded images, to filter out noise. During that process, all oil pores smaller than the volume of 10 voxels, which were not connected with at least one face to another oil inclusion were removed. This resulted in an elimination of smaller, unconnected and dispersal distributed oil inclusions and removal of noise. Finally, ring artefacts were manually edited in a few samples using the software Geodict2022.

Manual segmentation

A visually determined threshold was applied for ice and oil on selected iodine doped samples from the HSVA and the Norut II experiment. The CT scans were cropped to the largest possible VOI and filtred with a Median Filter (radius: 2 voxels) and a Gaussian filter (radius: 1.5 voxels) to reduce noise. The threshold was determined accordingly to the grey value histogram of each sample and verified by visual inspection and comparison of the segmented to the original CT reconstruction. The oil inclusions were observed to be surrounded by a few brine pixels. These brine pixels were mixed pixels between ice and doped oil. To remove the mixed pixels, we applied Dilation after the oil segmentation. Dilation expanded the oil inclusion laterally by the number of mixed pixels.

4.2.3 Pore space analysis

We analysed pore metrics as well as characteristic pore scales (pore and throat size) focusing on the oil pore space. An overview of investigated parameters for the oil thresholded by object tracing (OT), the semi-automated-segmentation (SAS) and the manual method are presented in table 4.2. The closed, open and total volume fraction of air (ϕ_{air}), brine (ϕ_b) and oil (ϕ_{oil}) were investigated. Furthermore, the pore size (PSD) distribution for the open and closed ϕ_{air} as well as for the total ϕ_{oil}, were obtained. The throat sizes (TSD) connecting the open ϕ_{air} and ϕ_{oil} were investigated. Oil content reference measurments Oil_{ref}, conducted by UV-fluorescence spectroscopy and μ-CT on melted samples are presented. Salinity measured by conductivity on melted samples (S_{oil}) was compared to the salinity S_{CT} derived from ϕ_b.

Table 4.2 Overview of measured parameters

Experiment	ϕ_{air}			ϕ_b			ϕ_{oil}			PS_{air}		PS$_{oil}$	TS$_{air}$	TS$_{oil}$	Oil$_{ref}$		S$_{oil}$	S$_{CT}$	Segmentation
	tot	open	closed	tot	open	closed	tot	open	closed	open	closed				UV	CT			
Norut I (SLF)	✓	✓	✓	✓	✓	✓	✓								✓		✓	✓	OT
Norut I (NTNU)	✓	✓	✓	✓	✓	✓	✓								✓		✓	✓	OT
Norut I (NTNU)	✓	✓	✓	✓	✓	✓	✓	✓	✓	✓	✓	✓	✓	✓	✓		✓	✓	SAS
Norut II	✓	✓	✓	✓	✓	✓	✓	✓	✓										Manual
Svea	✓	✓	✓	✓	✓	✓	✓	✓	✓	✓	✓	✓	✓	✓		✓	✓	✓	SAS
HSVA	✓	✓	✓	✓	✓	✓	✓	✓	✓	✓	✓	✓	✓	✓	✓		✓	✓	SAS
HSVA (doped)	✓	✓	✓	✓	✓	✓	✓	✓	✓										Manual

Porosity

The closed and open porosity were calculated using GeoDict, concerning the six faces in the Cartesian coordinate system for three-dimensional space. The x- and y-axis span the horizontal plane of the sample. The z-axis identifies the vertical direction. Pores connected to one of the six faces are defined as open pores. Closed pores, on the contrary, were isolated to any of the six sample faces. Based on this concept, the porosity of any segmented face (air, brine and oil) can be determined. Furthermore, the total brine porosity (ϕ_{tot}^{brine}) was used to calculate the CT-derived bulk salinity (S_{CT}). For further details on the calculation of S_{CT}, the reader is referred to equation 3.6 in section 3.2.3.

Pore and throat size distribution

The pore size (PS) distribution was determined for ϕ_{open}^{air},ϕ_{closed}^{air},ϕ_{tot}^{brine} and ϕ_{tot}^{oil} in GeoDict. The reader is invited to find additional information on the background on the calculations in section 3.2.3. The pore and throat size distribution were calculated for selected cores from the Norut I experiment imaged at NTNU, the Svea and HSVA experiment. All samples were thresholded with SAS.

4.2.4 Oil content measurements on melted samples

Two different approaches to measure the total oil content on melted samples were applied. Selected samples from the HSVA and Norut I experiment were analyzed by UV-fluorescent spectroscopy. The oil content on melted samples from the Svea experiment was derived from μ-CT scans.

- **UV-fluorescent spectroscopy**: We used a TD-500TM (Turner Desings Hydrocarbon Instrumens, Inc.) to determine the total oil content by ultraviolet (UV)- fluorescence spectroscopy. First,the contained oil from the melted sample was extracted using heptane. Subsequently, the oil concentration in the heptane-oil solution was determined. Under UV or near UV light, aromatic hydrocarbons of oil are stimulated to emit fluorescent light. The emitted fluorescent light is proportional to the concentration of the aromatic molecules in the sample. The TD-500TM was calibrated with the same crude oil as used in the experiments, and the intensity of the fluorescent emission corresponds to the oil concentration in the extract(Brost et al., 2011).

- **Oil content from μ-CT**:

  The volume fractions of the individual samples was determined by CT imaging of the melted samples. To enhance the absorption contrast between oil and the saline solution, approximately 0.05 g of iodoheptane was added per 100 mL of sample. The oil content reference measurements was performed at NTNU at a current and peak energy of 200 kV and 300 μA with a resolution of 16 μm, an exposure time of 354 ms and 800 projections per 360°. The μ-CT imaging was performed in test glasses (3 cm in diameter) holding approximately 100 mL of melted sample. Acquired image stacks were reconstructed with beam hardening correction and stored as 16-bit image stacks. The image stacks were cropped with a maximum VOI in Fiji (ImageJ). Subsequently, the image stacks were filtered in GeoDict using a Median filter with a sphere radius of 2 voxels and a Gaussian filter with a sphere radius of 1 voxel and a sigma of 1.5 voxels. The segmentation was performed in Geodict, where the diesel threshold was visually determined from the grey value histogram. The obtained diesel volume fraction was converted into mass volume fraction to be comparable with the UV-fluorescent spectroscopy measurements.

4.3 Results and Discussion

4.3.1 Ice thickness

The measured ice thickness for the cores from the Norut I experiment was around 12 cm. Presented cores from the Svea experiment are Svea 5-2, cored on the 12. April 2016 with a length of 40 cm and sample Svea 1-1 with 42 cm in length, sampled on 23 April 2016. Salinity and temperature cores were somewhat longer(39-49 cm). Cores containing oil from the HSVA experiment were sampled with a length of 18 cm, and the salinity and temperature cores were slightly longer (23 -25.5 cm). Presented samples from the HSVA experiment were sampled towards the end of the experiment on 02 April 2017.

4.3.2 Temperature

Depth profiles of sea ice temperature profiles from oil- and diesel-free cores in °C are shown in Figure 4.1. Unfortunately, the sea ice temperature for the Norut I experiment was not recored. The temperature profile from the experiment Norut II is plotted as solid purple line. The temperatures plotted for Norut II were measured with a set of thermocouples frozen into the ice. We measured sea ice temperature in the range of -8.9 °C at the top to -2.2 °C at the bottom. The dashed red and blue lines represent sea-ice temperature measurements from the Svea experiment associated with core Svea 5-2 (-3.9 to -2.2 °C)and Svea 1-1 (-3.2 to -1.6 °C), respectively. Svea 5-2 was sampled on the 12 April and was slightly cooler than Svea 1-1 sampled on 2 April. Sea ice temperature profiles linked to the presented cores from the HSVA experiment are depicted with a yellow dotted line ranging

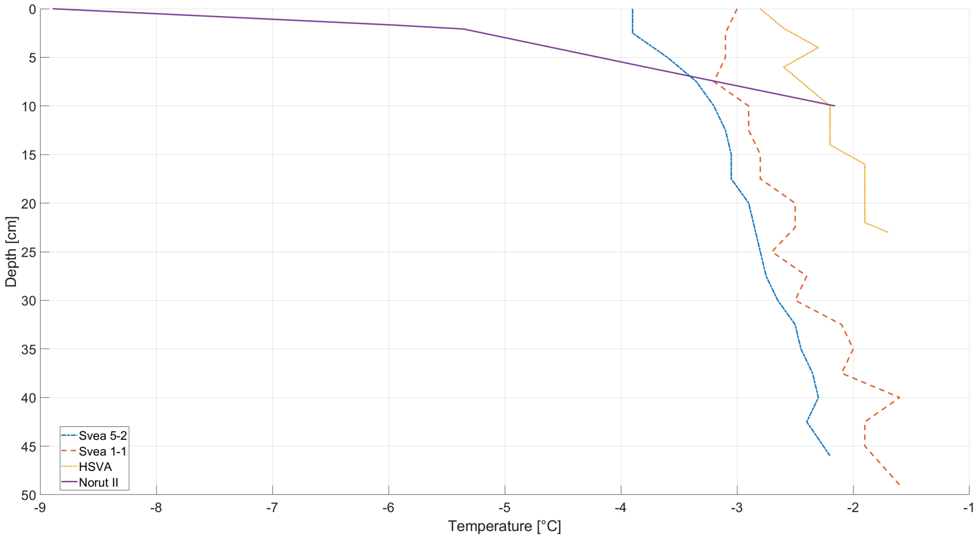

Fig. 4.1 Depth profiles of sea ice temperature cores are presented. The dark blue dashed line presents the temperature profile for core Svea 5-2, and the red dashed line presents the temperature profile for core Svea 1-1. The dotted yellow line presents the temperature profile from the HSVA experiment. The temperature profile from Norut II is measured with thermocouple probes.

from -2.8 to -1.7 °C. All samples were transported and imaged below their in situ temperature. Although the aim was to maintain conditions as close to in situ as possible, a comprise had to be made due to the presence of oil. For oil- and diesel-free cores, it has been conclusively shown that microstructural changes related to temperature fluctuations are minimized by centrifuging the samples (Salomon et al., 2021; Maus, 2020). Centrifuging sea ice samples containing oil would not only removed the brine but also the oil and diesel content. As a result, the microstructure investigations on diesel and oil samples presented here do not precisely meet in situ conditions. Observations linked to the brine volume fraction are particulary unrepresentative of in situ conditions and instead gave a conceptual image of the brine distribution. However, the air and oil fraction is believed to be less affected by temperature fluctuations (Desmond et al., 2021). Nevertheless, the 3-D distribution and characteristic pore-scale parameters of oil and diesel in sea ice were successfully studied.

4.3.3 Segmentation

Thresholding of μCT images is a crucial image processing step and subjected to several sources of errors. The segmentation step defines the geometry and volume fractions of the constituents, thus the highest precision was essential for all quantitative analysis of the samples that followed. The main difficulty in the segmentation of μCT images in this study stemmed from the low contrast between ice and oil, which made it necessary to remove the grey value gradient within the μCT images towards the edges and faces. The oil and the ice peak observed on the grey value distribution, were noted to overlap. Desmond et al. (2021) presented grey value histograms from oil containing sea ice samples, where the ice and oil peak were clearly separated from each other. The ice peak was found at about two times higher grey values than the oil peak. (Desmond et al., 2021) chose a lower acceleration voltage of 50 kV, a higher current of 800 μA and a longer exposure time, compared to the energy settings in this study. We observed as well better absorption contrast at lower energy settings in the SLF acquisitions of the Norut I samples (Figure 4.4). Desmond et al. (2021) used polypropylene sample holder, as we did for the imaging at SLF, compared to the aluminium sample holder used in the acquisition for the HSVA, Svea and Norut I samples at NTNU. Polypropylene has a lower density and consequently a lower X-ray absorption than aluminium, allowing X-rays with a lower energy to pass through (beam hardening). The chosen thresholding approach using SAS (to remove the brightness gradient) gave concern to the detectability of larger oil inclusion. The signal from homogeneous oil lenses approximately two times the kernel size of the 2- D median filter used to produce the background image vanished in the matrix. Consequently, we could no longer detect the oil signal and segmented it as ice. This issue appeared in sample Norut E4. Due to this artefact, a ϕ_{tot}^{oil} of 0.82 mass % was measured in comparison to 3.09 mass% from the UV- fluorescence measurements. The application of a more generous 2-D median filter in the background image production could resolve this problem. Trials showed that no significant change was achieved by applying a kernel size of 100 or 200 pixels regarding the segmentation of bigger oil inclusions. We suppose that applying a kernel size exceeding 200 pixels could have generated the desired result. Unfortunately, this question could not be answered since the computational power restricted the kernel size to 200 pixels.

Another problem arose from the resolution limitation in the μ-CT scans. Objects smaller than double the voxel size are not sufficiently resolved and may appear as mixed pixels. Consequently, the mixed pixel might be segmented as the wrong phase. Most mixed pixels were observed to arise where air met ice. These pixels were erroneously segmented as oil before the SAS algorithm was applied. The mixed air and ice pixels were reduced by the pre-segmentation steps of the SAS method. To gain confidence two additional segmentation methods were performed and the results compared with oil content measurements on melted samples. Segmentation of oil with OT is subjective since it is a manual segmentation method. Questionable oil signals were quickly discarded, especially when they appeared only in one slice. The manual segmentation of doped oil samples was promising, although mixed pixels of doped oil and ice were segmented around the oil inclusions as brine. The latter was easy to handle by dilation. Additionally, a prominent emptied brine channel was observed with a local braided network partially filled with oil in the centre of the core. We assume that the confined ice growth conditions in the cardboard forced the brine channel to form. O'Sadnick et al. (2017) observed the same in a study conducted, where sea ice was grown inside a cardboard tube. Results from the oil segmentation on synchrotron radiation CT scans showed flaws created by streak and phase-contrast artefacts occurring at the edges of the oil inclusions. Streak artefacts appear as radial brighter lines and resemble the form of stars. This artefact is associated with X-ray scattering and beam hardening. Phase-contrast artefacts let the oil inclusion edges appear sharper and were observed as a brighter line around the oil inclusion. Both artefacts were likely to be falsely segmented as brine and for this reason, these images were not further evaluated quantitatively.

4.3.4 Salinity and brine porosity

Figure 4.2 presents salinity concentration (psu) as a function of ice thickness (cm). Profiles a-d) show results from conductivity measurements on melted oil- and diesel-free cores (S_{free}). The salinity cores were sampled in close vicinity to oil and diesel cores. Figure 4.2 e-g) presents conductivity measurements from melted oil- and diesel cores (S_{oil}). Salinity calculated at in situ temperature from brine porosity (S_{CT}) where oil was segmeted by SAS is depicted in Figure 4.2(h-j), by OT (l-m), and by visual segmentation (n-o). S_{CT} and S_{oil} profiles were shorter than S_{free} profiles. The fragile skeletal layer often fell off during the sampling of oil/diesel cores. Also the injected oil slowed down the growth rate in the oil cores which led to shorter S_{CT} and S_{oil} profiles. The HSVA salinity profiles S_{free} depict that the columnar oil core 18CO had lower salinity than the granular oil core 18GO , where the upper part of the cores deviated the most. In general S_{free} (3.6-14.7 psu) was found to be higher than S_{oil}(0.7-7.9 psu) and S_{CT} (0.03-10.9 psu). The correlation suggests that oil replaced some brine (Oggier et al., 2019). In addition, some brine might have leaked from the sample from coring until CT-scanning, and the final conductivity measurements. Comparison of average higher ϕ^{air}_{tot} (0.3-17.2 %) for samples containing oil, where ϕ^{air}_{open} was (0.03-17.0 %), with ϕ^{air}_{tot} (1.3-2%) from oil free cores presented in Chapter 3, supported the idea of brine leakage. Consequently we presumed that ϕ^{air}_{open} represents the leaked brine and oil pore space. S_{oil} and S_{CT} measured on samples from the Svea experiment were less saline, and additionally had a bigger oil content than those from the HSVA. This observation suggests that the transfer of the ice cores into the cardboard tubes prior to the oil injection caused brine to leak. Comparison of S_{oil} with S_{CT} revealed that in the Svea and HSVA cores around 50 % of S_{CT} at a voxel size of 49 μm were overlooked (Figure: 4.3). Scans with a voxel edge length of 25 μm (Norut I) resolved ϕ_b better and in average 15% of S_{CT} was not detected in samples segmented by SAS. In the Norut I samples segmented by OT, 9% of S_{CT} was overlooked. At a resolution of 18 μm, the oil segmentation with OT overestimated S_{CT} by an average of 15 % in comparison to S_{free}. Overestimation of S_{CT} might have arisen due to several different reasons:

- If the actual scanning temperature was incongruent with the set scanning temperature, assumed for further calculations. The temperature influences the brine salinity S_b and brine density ρ_b and is therefore crucial for the calculation of S_{CT} after equation 3.6 in section 3.2.3.
- In noisy CT- scans, which were not sufficiently filtered, the noise was potentially segmented as brine. The application of filters with a bigger kernel might erase distinct transition from objects. From our experience, the application of successive filtering with a Median filter (radius: 2 voxels) and Gaus filter (radius: 1.5 voxels) preserved edges from distinct objects in the best possible way while reducing the signal to noise ratio within the CT- scans.
- As mentioned earlier brine might have leaked between CT-scanning and conductivity measurements.

Underestimation of S_{CT} can occur due to resolution limitations. The brine pore size distribution revealed that around 54 % of the pores range in the class of 1-2 voxes and 11 % in the range 2-3 voxel (voxel size: 49 μm) from the Svea experiment, 31 % and 13%, respectively from the HSVA experiment and 11 % and 7 %from the Norut I experiment (voxel size:25 μm) (Figure: 4.5). The exponential fall in the ϕ_b PSD from 1 voxel to 3 voxels in the Svea and HSVA data makes it very likely that a significant part of the brine volume fraction we overlooked. A comparison to Salomon et al. (2021) and the brine pocket PSD of oil-free cores reveal that 16 % and 13% of the brine pockets were found at at a voxel size of 25 to 50 μm and 50 to 75 μm respectively. As mentioned before, pores smaller than 2 times the voxel size might not be sufficiently resolved and potentially appear as mixed pixels. Considering the missing ϕ_b derived salinity S_{CT} in comparison with the conductivity derived salinity S_{oil}, the fractions showed good correspondence. It should be mentioned that neither ϕ_b nor the PSD ϕ_b represented in situ conditions.

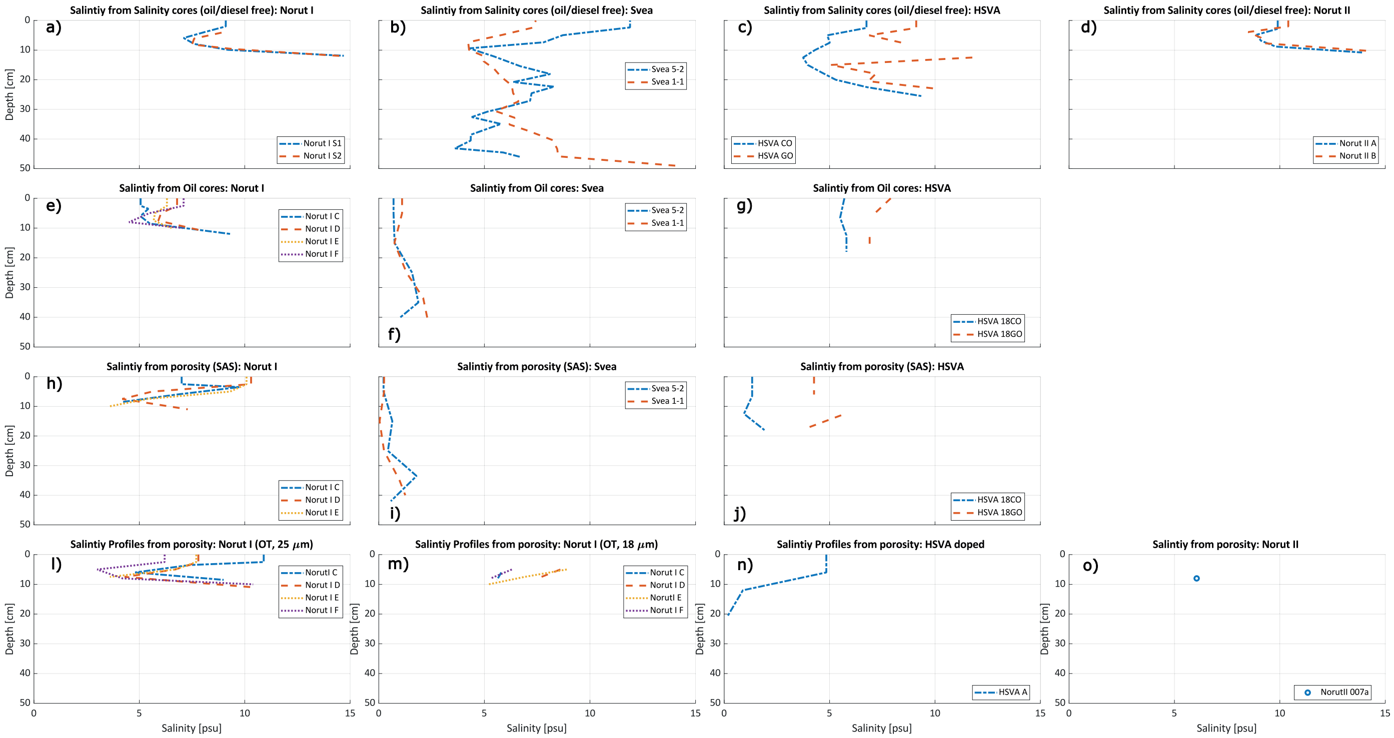

Fig. 4.2 Depth profiles of salnity (a-d) from oil- and diesel-free salinity cores (S_{free}). e-g) Salinity from melted oil/diesel cores (S_{oil}), (h-j) calculated salinity profiles from porosity (SAS) at in situ temperature (S_{CT}), (l-m) calculated salinity from porosity (OT), brine porosity obtained from CT-scans with 25 μm and 18 μm voxel edge length, respectively (S_{CT}). n) salinity (S_{CT}) from visually segmented scans of a doped HSVA sample and o) salinity (S_{CT}) from the Norut II experiment.

4.3.5 Oil porosity

The total, open and closed porosity is presented for ϕ_{oil}. The porosity is presented in volume fraction in % over the total analysed sample volume for each sub-sample and plotted as a function of the ice thickness in cm in Figure 4.6. The results were based on measurements on CT scans and represent the pore space at an imaging temperature of -15°C. In all plots, the total porosity ϕ_{tot} is shown in blue, where the total porosity is the sum of the open porosity ϕ_{open} represented in red and the closed porosity ϕ_{closed} in yellow. a-b) presents results for ϕ_{oil} from the Svea experiment, the oil was thresholded by SAS on images with a voxel size of 49 μm. c-d) shows the ϕ_{oil} profiles for the HSVA experiment the SAS was applied on scans with a resolution of 49 μm. e-g) ϕ_{oil} for Norut I was thresholded by SAS with a voxel size of 25 μm. h) presents ϕ_{oil} for a doped core from the HSVA experiment at a resolution of 49 μm thresholded by visual segmentation based on the grey value histogram. ϕ_{oil} for Norut I samples, OT was applied for segmentation i-l) oil on scans with a resolution of 25 μm and m-p) with a voxel size of 18 μm.

For all experiments most of ϕ_{oil} was present in closed pores. Comparisons for ϕ_{tot}^{oil} derived from SAS on scans with voxel size of 49 μm suggested that the Svea samples (0.1-2.3 %) had a higher oil volume fraction than the samples from HSVA (0.03-0.5 %). Samples analysed from the Norut I experiment with a resolution of 25 μm and thresholded by SAS show a range of ϕ_{tot}^{oil} from 0.1-7.9 %. The OT approach on Norut I samples imaged with a voxel size of 25 μm gave a ϕ_{tot}^{oil} range of 0.01-29.47 % and at 18 μm from 0.009-17.8 %. From the observations of Norut I cores segmented by SAS and OT on scans with a resolution of 25 μm, we concluded that SAS tended to give higher ϕ_{tot}^{oil} than OT, with some exception. Increased ϕ_{tot}^{oil} segmented by SAS in comparison to OT might be subjected to the manual segmentation. In the manual OT approach the tendency to discard doubtful oil signals, especially those just appearing in a single slice, needs to be considered. A direct comparison of ϕ_{tot}^{oil} on samples scanned with different voxel resolution and oil was thresholded by alike methods is difficult.

Comparison of ϕ_{oil} on frozen samples (Oil_{CT}) and reference measurements on melted samples showed that the reference measurements with the μ-CT (Oil_{CT}^{ref}) applied on the Svea samples generally underestimated ϕ_{oil} (Figure: 4.3b) . The UV fluorescent spectroscopy measurements Oil_{UV}^{ref} applied to HSVA and Norut I samples showed neither a systematic under- nor overestimation. The underestimation of Oil_{CT} can be explained by the resolution limitation of the μ-CT acquisitions. As figure 4.5 shows, more than 50 % of oil pore sizes detected in the Svea (56%) and HSVA (71%) experiment fell into the class of 1 voxel, and more than 10 % ranged into the category of 2 voxels (Svea: 14 %, HSVA: 12 %). The resolution of 25 μm in Norut I samples resolved the oil pore sizes better. About 16 % of the oil pores are found in the class of 1 voxel and 3% in the spectra of 2 voxels. Deviations can be explained as follows.

- The overestimation of Oil_{CT} on samples from the Norut I experiment scanned with a resolution of 18 μm at SLF can be explained as follows. Oil was lost from the acquisition at SLF until μ-CT scanning at NTNU and the final melting of the samples and oil mass concentration measurements. One example of oil loss from scanning at SLF until the acquisitions at NTNU is presented in figure 4.4.
- Underestimation of Oil_{CT}^{ref} in the Svea experiments can most probably be explained by the technique used to determine the oil mass on melted samples. Since we acquired the melted sample in the μCT, resolution limitations and diverse segmentation flaws might occur and lead to a general underestimation of the oil volume Oil_{CT}^{ref} .

It was observed that oil inclusions were often adjacent to air inclusions (Figure 4.8). In the upper layers of the ice, oil tended to appear dispersed. At the same time, filled channels (most likely emptied brine channels) with oil were found in the lower columnar part of the ice. Oil and brine were observed to be separated and not approximating each other.

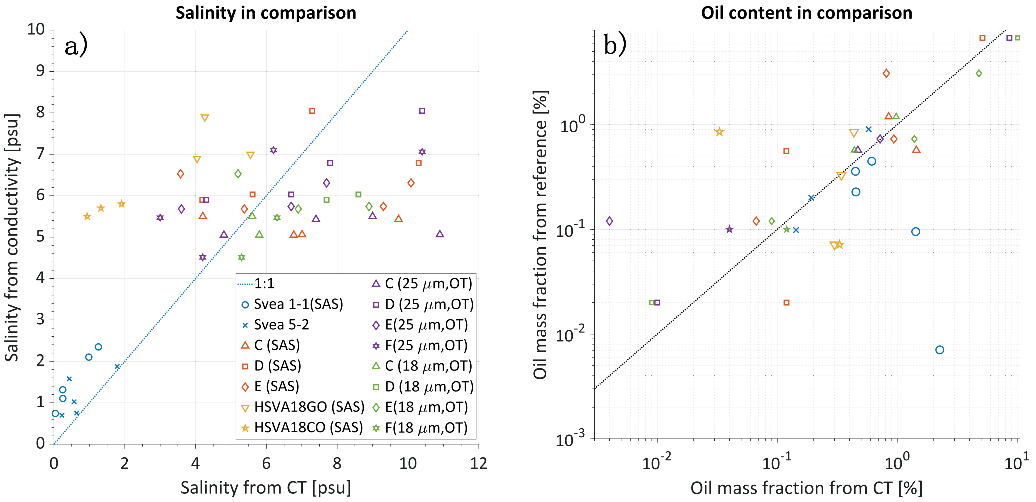

Fig. 4.3 a) Salinity measurements on melted samples in comparison with salinity derived by ϕ_b from CT-scan. b) Oil mass fraction derived from CT- image analysis in comparison with oil content measurements on melted samples. Blue dotted line representing perfect compliance.

4.3.6 Pore- and throat size distribution

The pore size distribution (PSD) was measured for ϕ^{air}_{open}, ϕ^{air}_{closed}, ϕ^{brine}_{tot} and ϕ^{oil}_{tot} in μm for cores from the Norut I, Svea, and HSVA experiment thresholded with SAS . ϕ^{air}_{open} and ϕ^{air}_{closed} are depicted in blue, ϕ^{brine}_{tot} in red and ϕ^{oil}_{tot} in yellow. The pore size distribution mode is demonstrated with a circle, and the median is plotted as a square. The throat size distribution is presented in the same manner (Figure 4.7) for ϕ^{oil}_{open} in yellow and ϕ^{air}_{open} in blue. In general larger pores were measured for ϕ^{air}_{open} (median PS: 0.16-2.6 mm) than ϕ^{air}_{closed} (median PS: 0.14-3.1 mm), with an exception in subsample Norut D3 where ϕ^{air}_{open} (median PS: 1.7 mm) was smaller than the median PS ϕ^{air}_{closed} (median PS:3.1 mm). We observed similar pore sizes for ϕ^{air}_{closed} in all the experiments.

The PSD ϕ^{brine}_{tot} started with a peak at the resolution limit of the CT-scans for samples imaged with a voxel size of 49 μm, indicating that the full spectrum of PS for ϕ^{brine}_{tot} was likley not resolved. Interestingly, a distinct local maximum in the size of 3-4 voxels in the ϕ^{brine}_{tot} PSD for the Svea and HSVA cores and at 5-6 voxels for the Norut experiment were observed. The mode of the PSD ϕ^{air}_{closed} in data from Svea and HSVA were always found at pore sizes slightly larger than the local maximum in the pore size distribution for ϕ^{brine}_{tot}, which is as expected as the air bubbles were accommodated in the brine channels.

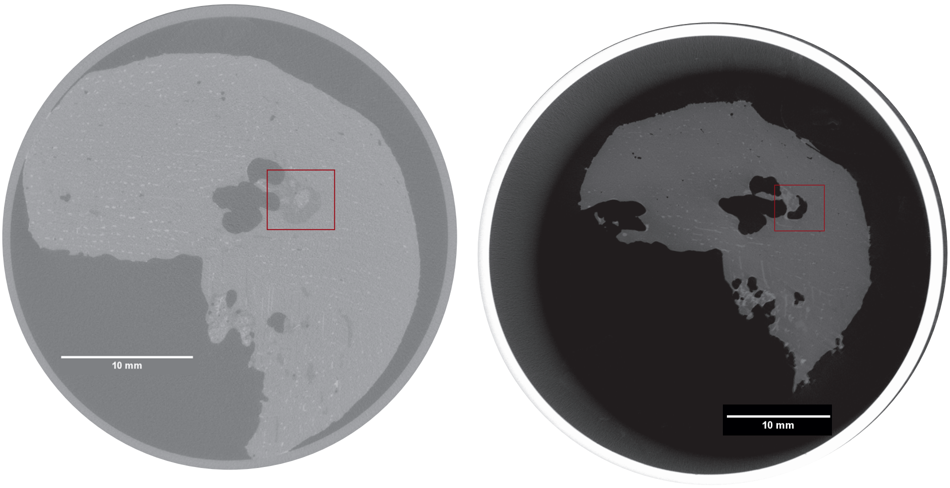

Fig. 4.4 Transversal cross-section from Norut I experiment (sample Norut C4). To the left the aquisition from SLF and to the right a scan from NTNU. Red box marks area were oil was lost during the two different μ-CT aquisitions.

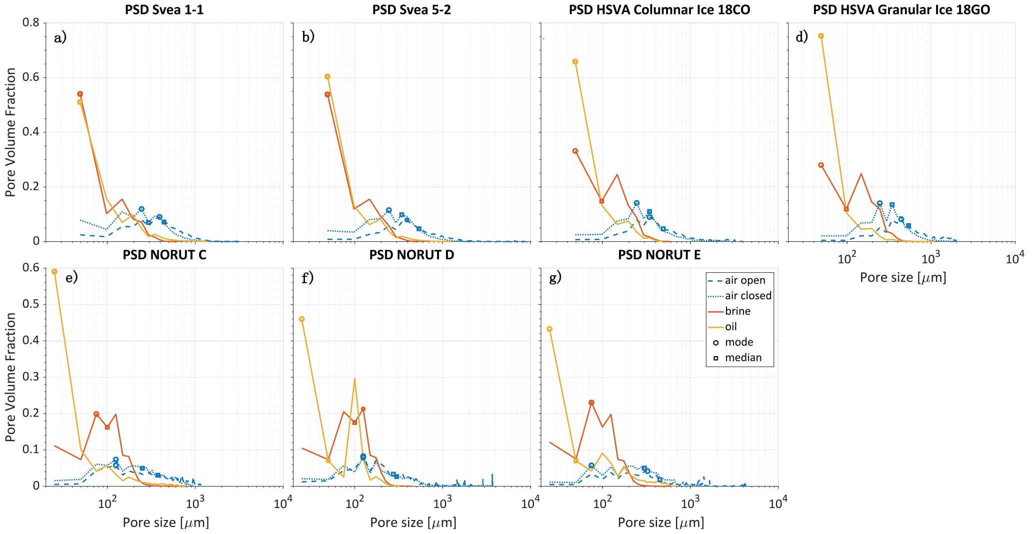

Fig. 4.5 Pore size distribution for oil porosity from SAS. (a-g) Pore volume fraction for oil in % plotted against the pore size in μm.

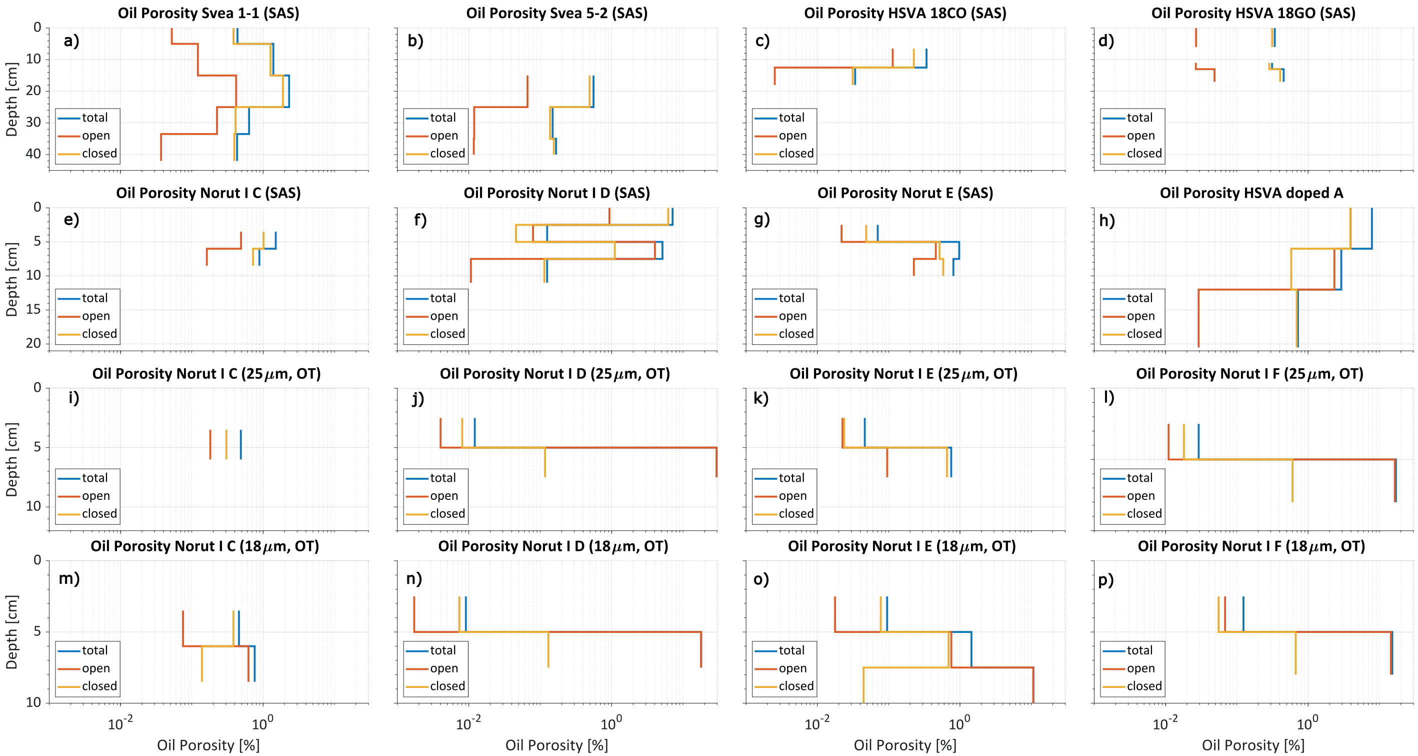

Fig. 4.6 Total-(blue) open-(red), and closed-(yellow) oil porosity in % for each sub-sample is plotted over the depth in cm at a temperature of -15 °C. Where 0 is the top. a-b) porosity from Svea experiment SAS-approach at a resolution of 49 μm. c-d) oil porosity from HSVA experiment SAS-approach at a resolution of 49 μm and e-g) oil porosities from Norut I experiment with a scanning resolution of 25 μm and segmented with SAS. h) Porosities from doped HSVA samples scanned with 49 μm resolution and visually segmented. l-p) Oil porosity from Norut I experiment segmented with OT on scans with 25 and m-p) 18 μm resolution respectively.

The largest brine pore (0.9 mm in diameter) was noted in core Norut C, while the median brine pore size in the subsamples varied between 0.08-0.2 mm. Observations made on the PSD for ϕ_{tot}^{oil} indicated that the smallest pore sizes are likley not resolved for both the voxel size of 49 μm and 25 μm, since a pronounced peak in the size of one voxel was observed. From the ϕ_{tot}^{oil} PSD we determined that more than half of the oil pores were not detected in the Svea and the HSVA experiments. 56 % of the oil pores in the Svea experiment were in the size of 1 voxel, and 14 % had a size of 2 voxels. The HSVA ϕ_{tot}^{oil} PSD showed that 71 % of the oil pores have the size of 1 voxel and 12 % the size of 2 voxels. Data acquired at higher resolution as for the Norut I experiment were better resolved. Around 16 % of the pores had the size of 1 voxel and 3% the size of 2 voxels. The largest oil pore was detected in the Svea cores with a diameter of 1.5 mm, with a median oil pore size between 0.04-0.2 mm. The largest oil-filled pores were larger than the biggest brine-filled pores.

Comparison of the PSD for ϕ_{oil}^{tot}, ϕ_{brine}^{tot}, ϕ_{air}^{open} and ϕ_{air}^{closed} (Figure 4.5) were interpreted as follows:

- The local maximum found in the PSD ϕ_{brine}^{tot} at approximately 170 μm (3-4 voxel) in the Svea and HSVA experiment and at 140 μm (5-6 voxel) in the Norut experiment can be assumed to resemble the actual mode of the brine pore distribution.
- A local maximum was observed in the PSD for ϕ_{oil}^{tot} at around 220 μm (4-5 voxel) in the data from the Svea and HSVA experiment and at around 110 μm (4-5 voxel). As for brine the local maximum in the oil pore size distribution can be interpreted as the actual mode.
- The peak in PSD ϕ_{open}^{air} at bigger pore sizes than the local maximum in PSD ϕ_{tot}^{brine} and ϕ_{tot}^{oil}, is conclusive, since oil and brine was hosted in ϕ_{open}^{air}.
- The local maximum in PSD ϕ_{tot}^{oil} was observed at slightly bigger pore sizes than ϕ_{tot}^{brine}, implementing that ϕ_{tot}^{oil} pore sizes were less affected by temperature changes than ϕ_{tot}^{brine} (Desmond et al., 2021).

Calculations for the throat size distribution were carried out for ϕ_{open}^{oil} and ϕ_{open}^{air}. Similar to the PSD for ϕ_{tot}^{oil} the distribution started with a peak at 1 voxel. Comparing PSD and TSD ϕ_{open}^{oil} revealed that the median for TSD (0.03-0.1mm) were smaller than for the median PSD (0.04-0.2 mm). The same observation applied for the relation between the median PSD (0.16-2.6 mm) and TSD (0.12-2.6 mm) ϕ_{open}^{air}. PSD and TSD forϕ_{open}^{air} were an order of magnitude bigger than for ϕ_{open}^{oil}.

4.4 Conclusion

The 3-dimensional distribution of oil within sea ice and the characteristic pore metrics were studied on selected samples from four different oil in ice experiments. The experiments covered two small-scale test tank experiments (Norut I & II) and a large tank experiment (HSVA) with artificial grown sea ice, as well as a field study (Svea) with naturally grown ice. The oil in the samples of these experiments was segmented using three different approaches: (i) a semi-automated segmentation (SAS), (ii) segmentation by manual object tracing (OT) and (iii) manual segmentation. Our main observations are:

- We detected oil throughout the whole sea ice column in granular and columnar ice. We observed that the oil was dispersed in granular ice and tends to accumulate in channels within columnar ice.
- The median oil pore size was 0.04-0.2 mm. The maximum oil inclusion found had a pore size of 1.5 mm.
- The throats connecting the open oil pores are slightly smaller than the median oil pores size of 0.03-0.1mm.

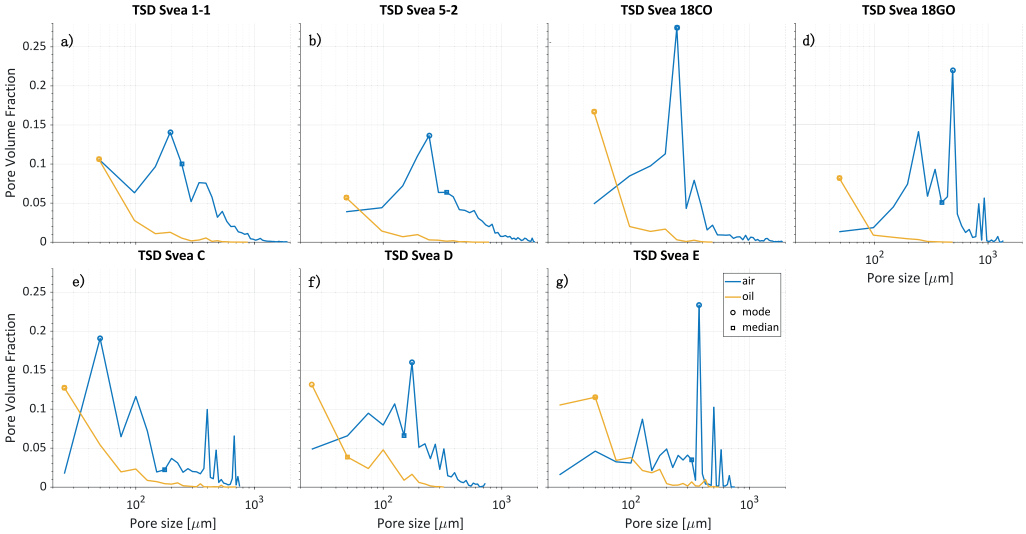

Fig. 4.7 Throat size distribution for the open air and oil porosity. The throat size distribution in μm is shown as a function of its frequency.The blue line represent the throatsize distribution for ϕ^{air}_{open} and the yellow line for ϕ^{oil}_{open}. The mode is presented circles and the median by squares.

- In general, we observed higher S_{free} than S_{oil} suggesting that some brine was replaced by oil.
- SAS and OT approach compared on samples from Norut I imaged with a resolution of 25 μm suggest that SAS detects more oil than OT since the OT approach is subjected to flaws in the manual segmentation.

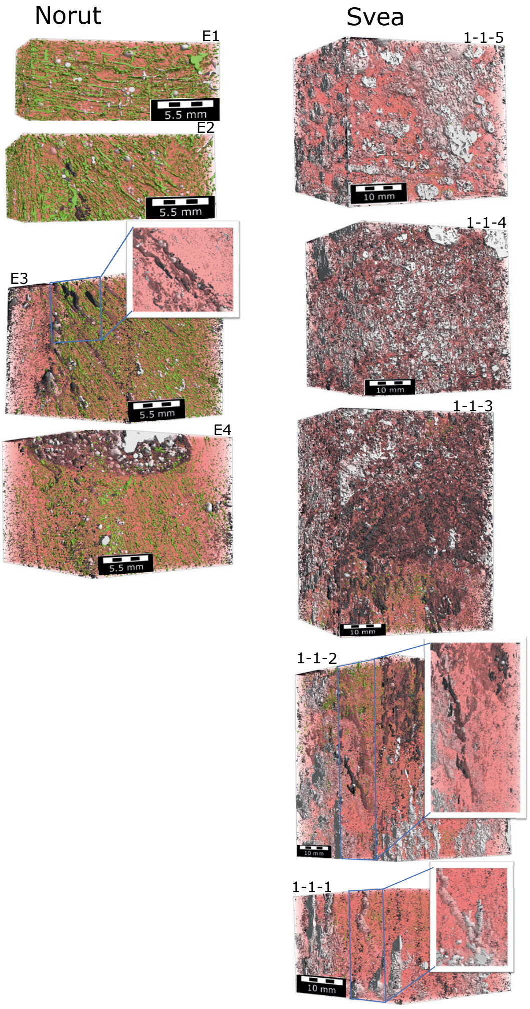

Fig. 4.8 3-D segmented core with (SAS): Norut E, Svea 1-1 and HSVA 18GO. In red ice, green, brine, white air and black oil. Norut E to the left had an average ϕ_{oil}: 0.46 % , ϕ_{brine}: 3.19%, ϕ_{air}: 2.11 %. Svea 1-1 in the middle had an average ϕ_{oil}: 1.04 % , ϕ_{brine}: 0.24%, ϕ_{air}: 5.32 % . HSVA 18GO to the right had an average ϕ_{oil}: 0.37 % , ϕ_{brine}: 2.05%, ϕ_{air}: 2.50 %

Chapter 5

Conclusion and future perspectives

Dum og deilig (Knutsen & Ludvigsen)

5.1 Conclusion

This thesis addresses i) microstructural investigations and the evolution of the sea ice pore scale and ii) the distribution of oil and diesel within sea ice. The microscopic sea ice properties of clean sea ice were defined at in situ temperature through a combined technique of (i) brine removal via centrifuging, (ii) μ-CT scans and (iii) morphological analysis. The distribution of oil and diesel has been studied on selected samples from different oil in ice experiments (small-, large- ice tank, and field experiment) and different μ-CT acquisition systems . Challenges met in the segmentation of the low absorption contrast between oil in ice met in μ-CT scans were overcome by (a) visual tracing of oil inclusions (OT) and (b) a novel semi-automated segmentation (SAS) method. Novel insights into the 3-dimensional distribution of diesel and oil within sea ice were made.

The main findings presented in the thesis are as follows:

- Observations on the brine porosity and related parameters are underestimated due to spatial resolution limitations in the μ- CT scans. The pore and size distribution of the closed brine volume fraction ($\phi_{bclosed}$) suggests that at a resolution of 25 μm, and at -15 °C imaging temperature, around 16 % of the detected pores fall into the range of the resolution limitation. For a resolution of 49 μm, the fraction of undetected brine pores is even higher, 54 % for the Svea experiment and 31% for the HSVA experiment. I.e, approximatly 50 % of the salinity is overlooked in scans with a voxel edge length of 49 μm, while in scans with a voxel edge length of 25 μm the salinity is overestimated by about 5 %. To estimate the number of undetected brine pores, one needs to obtain scans at a higher resolution. Although the CT derived brine porosity is limited, the strength of the technique is to investigate porosity metrics such as the open, closed and connected brine porosity, the local distribution, vertical connectivity and characteristic pore scales.
- Investigations of the time-dependent variation of salinity, density and pore sizes in Arctic young sea ice show that these parameters remained constant. At the same time, a decrease in the pore number linked to an increase in connection of the pores is observed.
- From observations of the 3-D oil distribution, it is reasonable to conclude that oil was found throughout the whole sea ice. The dispersed distribution of oil is mainly observed in the upper granular part of the sea ice, while oil tends to collect in channels in the columnar part of the ice. It was not possible to investigate the oil distribution in the fragile skeletal layer since the part of the samples was destroyed during sampling.
- The average median oil pore size detected was 0.04-0.2 mm. This is similar to the resolution limit observed for the brine pore fraction, therefore smaller oil pores remained undetected . We found that more than half of the oil inclusions observed from the Svea samples and more than $\frac{3}{4}$ of the oil pores from the selected HSVA samples were not detected. The data set of oil inclusions scanned at a higher resolution of 25 μm were better resolved, and around 19 % of the pores were not detected. Again the underestimation of oil pore sizes can be addressed by scanning at a higher resolution.

- Comparison of the different oil segmentation methods presented suggests that OT detects less oil than SAS. OT is based on manual segmentation and is therefore subjective, smaller oil signals might not have been visually detected, and doubtful signals are not segmented and analysed. On the contrary, the SAS approach raises concerns about the detectability of bigger homogeneous oil signals.

5.2 Future perspectives

Global warming is undeniable. According to the IPCC (2021) the Arctic surface air temperature has increased more than two times the global average temperature in the last 20 years. Sea ice falls as a victim to the increasing global temperatures. Observed reductions in the September sea ice extend suggests that 12.8% (± 2.3%) is lost per decade from 1979-2018. This rapid loss is unprecedented in the last 1000 years and contributes to increased warming. Linked to the current degradation of the sea ice extend, the shipping activity in the Arctic summer has increased.

By conducting this study and disseminating my findings with fellow researchers, I actively contributed to diminishing this thesis's core matter and material. A rough calculation of the CO_2 emission by solely travelling via plane throughout this study is 3071.6 kg CO_2. To limit the global temperature rise to below 2°C in the 21st century, the estimated maximum emission per person and year is 1610 kg CO_2 (O'Neill et al., 2018). Meaning that plane travels in this study consumed approximately the CO_2 emissions of one person in 2 years. Having said this, there are still plenty of questions that could be answered nearly emission-free with the acquired data sets during this PhD.

- The mechanism of oil and diesel migration throughout the sea ice pores on a micro scale remains uncertain. With the two collected data sets from a conducted field study (Svea) and a ship-tank experiment (HSVA), aspects of the oil migration could be studied, throughout the sea ice growth season until the onset of melt. Investigations on a larger data set could improve the semi-automated segmentation and allow the training of an AI-based algorithm.
- The investigation on the evolution and migration of oil in sea ice throughout a seasonal cycle on young arctic sea ice and data from a ship-tank experiment could be implemented in oil migration models to improve the hazard response, as the exact timing of oil surfacing could be predicted. Consequently, oil cleanup by in situ burning, as it is a widely implemented technique, can be timed, before the volatile components of oil have evaporated, which determine the success of burning.
- A study on sea ice density measurements by μ-CT scans compared to hydrostatic weighing and volume to mass estimations could diminish the uncertainty in the well established density evaluation methods. This could improve the sea ice thickness estimation by satellite.
- Improvements in the semi-automated segmentation algorithm could allow application in a broader field, for example in medical imaging, imaging in material science or the search for the perfect food texture. Simply, this could be applied in processes relying on imaging techniques where phases with a low absorption contrast appear, in addition to noise and brightness gradients.

And now, it is time to put some fresh air in my brain!

References

Assesment (2010) Oil and Gas Activities in the Arctic - Effects and Potential Effects. Tech. rep., Arctic Monitoring and Assessment Programme (AMAP), Oslo, Norway

Assur A (1960) Composition of Sea Ice and its Tensile Strength. SIPRE Research Report 44:54

Bartels-Rausch T, Bergeron V, Cartwright JH, Escribano R, Finney JL, Grothe H, Gutiérrez PJ, Haapala J, Kuhs WF, Pettersson JB, Price SD, Sainz-Díaz CI, Stokes DJ, Strazzulla G, Thomson ES, Trinks H, Uras-Aytemiz N (2012) Ice structures, patterns, and processes: A view across the icefields. Reviews of Modern Physics 84(2):885–944, DOI 10.1103/RevModPhys.84.885, 1207.3738

Brost DF, Foster A, Holmes M (2011) "No-Solvent" Oil-in-Water Analysis - A Robust Alternative to Conventional Solvent Extraction Methods, DOI 10.4043/21695-ms

Buist IA, Dickins DF (1983) Fate and Behaviour of Water-in-Oil Emulsions in Ice. Proceedings of the Arctic Marine OIl Spill Programm Technichal Seminar pp 263–279

Cox G, Weeks W (1986) Changes in the Salinity and Porosity of Sea-Ice Samples During Shipping and Storage. Journal of Glaciology 32(112):371–375, DOI 10.3189/s0022143000012065

Cox GF, Weeks WF (1982) Equations for Determining the Gas and Brine Volumes in Sea Ice Samples. CRREL Report (US Army Cold Regions Research and Engineering Laboratory) 29(102):306–316, DOI 10.3189/s0022143000008364

Cox GFN, Weeks WF (1983) CRREL Report 82-30, Equations for Determining the Gas and Brine Volumes in Sea Ice Samples. Journal of Glaciology 29(102):306–316

Crabeck O, Galley R, Delille B, Else B, Geilfus NX, Lemes M, Roches MD, Francus P, Tison JL, Rysgaard S (2016) Imaging air volume fraction in sea ice using non-destructive X-ray tomography. Cryosphere 10(3):1125–1145, DOI 10.5194/tc-10-1125-2016

Crabeck O, Galley RJ, Mercury L, Delille B, Tison JL, Rysgaard S (2019) Evidence of Freezing Pressure in Sea Ice Discrete Brine Inclusions and Its Impact on Aqueous-Gaseous Equilibrium. Journal of Geophysical Research: Oceans 124(3):1660–1678, DOI 10.1029/2018JC014597

Davies B (2022) What is the global volume of land ice and how is it changing? - AntarcticGlaciers.org

Desmond DS, Crabeck O, Lemes M, Harasyn ML, Mansoori A, Saltymakova D, Fuller MC, Rysgaard S, Barber DG, Isleifson D, Stern GA (2021) Investigation into the geometry and distribution of oil inclusions in sea ice using non-destructive X-ray microtomography and its implications for remote sensing and mitigation potential. Marine Pollution Bulletin 173:112996, DOI 10.1016/j.marpolbul.2021.112996

Dobinski W (2011) Permafrost. Earth-Science Reviews 108(3-4):158–169, DOI 10.1016/J.EARSCIREV.2011.06.007

Ebert EE, Curry JA (1993) An intermediate one-dimensional thermodynamic sea ice model for investigating ice-atmosphere interactions. Journal of Geophysical Research 98(6):10085–10109, DOI 10.1029/93jc00656

Eicken H, Bock C, Wittig R, Miller H, Poertner HO (2000) Magnetic resonance imaging of sea-ice pore fluids: Methods and thermal evolution of pore microstructure. Cold Regions Science and Technology 31(3):207–225, DOI 10.1016/S0165-232X(00)00016-1

Elmoutaouakkil A, Fuchs G, Bergounhon P, Péres R, Peyrin F (2003) Three-dimensional quantitative analysis of polymer foams from synchrotron radiation x-ray microtomography. J Phys D: Appl Phys 36:37–43

Everett KR (1989) Glossary of Permafrost and Related Ground-Ice Terms. Arctic and Alpine Research 21(2):213, DOI 10.2307/1551636

Fletcher N (1970) The Chemical Physics of Ice. Cambdrige University Press

Freitag J (1999) The hydraulic properties of Arctic sea ice: implications for the small-scale particle transport. PhD thesis, Alfred-Wegener-Institut (AWI) für Pola- und Meerforschung

Glaeser JL, Vance GP (1972) A study of the behavior of oil spills in the arctic. Tech. rep., U.S Coast Guard applied Technology Devision, DOI 10.4043/1551-ms

Glud RN, Rysgaard S, Kühl M (2002) A laboratory study on O2 dynamics and photosynthesis in ice algal communities: quantification by microsensors, O2 exchange rates, 14C incubations and a PAM fluorometer. Aquatic Microbial Ecology 27:301–311, DOI 10.3354/ame040251

Golden KM, Eicken H, Heaton AL, Miner J, Pringle DJ, Zhu J (2007) Thermal evolution of permeability and microstructure in sea ice. Geophysical Research Letters 34(16):2–7, DOI 10.1029/2007GL030447

Gough AJ, Mahoney AR, Langhorne PJ, Williams MJM, Haskell TG (2012) Sea ice salinity and structure: A winter time series of salinity and its distribution. Journal of Geophysical Research: Oceans 117(3):n/a–n/a, DOI 10.1029/2011JC007527

IPCC (2014) Climate Change 2014: Synthesis Report. Contribution of Working Groups I, II and III to the Fifth Assessment Report of the Intergovernmental Panel on Climate Change [Core Writing Team, R.K. Pachauri and L.A. Meyer (eds.)]. Tech. rep., Geneva, Switzerland

IPCC (2021) Technical Summary. Contribution of Working Group I to the Sixth Assessment Report of the Intergovernmental Panel on Climate Change. In Press

Karlsson J, Petrich C, Eicken H (2011) Oil entrainment and migration in laboratorygrown saltwater ice. In: Proceedings of the International Conference on Port and Ocean Engineering under Arctic Conditions, POAC, vol 1, pp 88–97

Kawamura T (1988) Observations of the internal structure of sea ice by X ray computed tomography. Journal of Geophysical Research 93(C3):2343, DOI 10.1029/jc093ic03p02343

Kulyakhtin A, Kulyakhtin S, Løset S (2013) Measurements of thermodynamic properties of ice created by frozen sea spray. Proceedings of the International Offshore and Polar Engineering Conference 9:1104–1111

Lake R, Lewis E (1970) Salt Rejection By Sea Ice During Growth. Journal of Geophyssical Research 75(3):583–597, DOI 10.1029/jc075i003p00583

Lange MA (1988) Basic properties of antarctic sea ice as revealed by textural analysis of ice cores. Annals of Glaciology 10:95–101, DOI 10.3189/s0260305500004249

Legendre L, Ackley S, Dieckmann G, Gulliksen B, Horner R, Hoshiai T, Melnikov I, Reeburgh W, Spindler M, Sullivan C (1992) Ecology of sea ice biota. Polar Biology 12(3-4):429–444, DOI 10.1007/bf00243114

Leppäranta M (2015) Freezing of lakes and the evolution of their ice cover. DOI 10.1007/978-3-642-29081-7

Leppäranta M, Manninen T (1988) BrineGasContent.pdf. Tech. rep., Finish Institute of Marine Research

Lieb-Lappen RM, Golden EJ, Obbard RW (2017) Metrics for interpreting the microstructure of sea ice using X-ray micro-computed tomography. Cold Regions Science and Technology 138:24–35, DOI 10.1016/j.coldregions.2017.03.001

Light B, Maykut GA, Grenfell TC (2003) Effects of temperature on the microstructure of first-year Arctic sea ice. Journal of Geophysical Research C: Oceans 108(2):33–1, DOI 10.1029/2001jc000887

Linden S, Cheng L, Wiegmann A (2018) Specialized methods for direct numerical simulations in poroous media. Tech. rep., Math2Market GmbH, DOI https://doi.org/10.30423/report.m2m-2018-01, Loose B, McGillis WR, Schlosser P, Perovich D, Takahashi T (2009) Effects of freezing, growth, and ice cover on gas transport processes in laboratory seawater experiments. Geophysical Research Letters 36(5), DOI 10.1029/2008GL036318

Maus S (2020) The plate spacing of sea ice. Annals of Glaciology 82, DOI 10.1017/aog.2020.65

Maus S, Huthwelker T, Enzmann F, Miedaner MM, Marone F, Hutterli MA, Hintermüller C, Kersten M (2009) Synchrotron-based X-ray micro-tomography: Insights into Sea Ice Microstructure. In: Proceedings of the Sixth Workshop on Baltic Sea Ice Climate, Lammi Biological Station Finnland, 61, pp 28 – 45

Maus S, Becker J, Leisinger S, Matzl M, Schneebeli M, Wiegmann A (2015) Oil saturation of the sea ice pore space. In: Proceedings of the International Conference on Port and Ocean Engineering under Arctic Conditions, POAC, vol 2015-Janua, pp 1–12

Maus S, Schneebeli M, Wiegmann A (2020) An X-ray micro-tomographic study of the pore space, permeability and percolation threshold of young sea ice. The Cryosphere Discussions pp 1–30, DOI 10.5194/tc-2020-288

Maykut GA, Grenfell TC, Weeks WF (1992) On estimating spatial and temporal variations in the properties of ice in the polar oceans. Journal of Marine Systems 3(1-2):41–72, DOI 10.1016/0924-7963(92)90030-C

Nakawo M (1980) Density of columnar-grained ice made in a laboratory. Tech. rep., National Research Council of Canada, DOI 10.4224/40000545

National Snow and Ice Data Center (2020) People and Frozen Ground | National Snow and Ice Data Center

Nelson KH (1953) A study of the freezing of sea water. PhD thesis, University of Washington, Seatle

Nelson KH, Thompson TG, Flend RH (1954) DEPOSITION OF SALTS FROM SEA WATER BY FRIGID CONCENTRATION. Tech. rep., University of Washington Department of Oceanography, Seattle., Washington

NORCOR Engineering and Research Ltd (1975) The Interaction of Crude Oil With Arctic Sea Ice. Tech. Rep. 27, Beaufort Sea Project, Dept. of the Environment, Victria, B.C.

Notz D, Worster MG (2009) Desalination processes of sea ice revisited. Journal of Geophysical Research: Oceans 114(5), DOI 10.1029/2008JC004885

Obbard RW, Troderman G, Baker I (2009) Imaging brine and air inclusions in sea ice using micro-X-ray computed tomography. DOI 10.3189/002214309790794814

Oggier M, Eicken H, Wilkinson JP, Petrich C, O'Sadnick M, O'Sadnick M, O'Sadnick M (2019) Crude oil migration in sea-ice: Laboratory studies of constraints on oil mobilization and seasonal evolution. Cold Regions Science and Technology 174:102924, DOI 10.1016/j.coldregions.2019.102924

O'Neill DW, Fanning AL, Lamb WF, Steinberger JK (2018) A good life for all within planetary boundaries. Nature Sustainability 1(2):88–95, DOI 10.1038/s41893-018-0021-4

O'Sadnick M, Petrich C, Phuong ND (2017) The entrainment and migration of crude oil in sea ice, the use of vegetable oil as a substitute, and other lessons from laboratory experiments. In: Proceedings of the International Conference on Port and Ocean Engineering under Arctic Conditions, POAC

Otsu N (1979) Threshold Selection Method From Gray-Level Histograms. IEEE Trans Syst Man Cybern SMC-9(1):62–66, DOI 10.1109/tsmc.1979.4310076

Otsuka N, Kondo H, Saeki H (2004) Experimental study on the characteristics of oil ice sandwich. Ocean '04 - MTS/IEEE Techno-Ocean '04: Bridges across the Oceans - Conference Proceedings 3:1470–1475, DOI 10.1109/oceans.2004.1406337

Perey FGJ, Pounder ER (1958) Crystal Orientation in Ice Sheets. Canadian Journal of Physics 36(4):494–502, DOI 10.1139/p58-050

Perovich DK, Gow AJ (1991) A statistical description of the microstructure of young sea ice. Journal of Geophysical Research 96(C9):16943, DOI 10.1029/91jc01594

Perovich DK, Gow AJ (1996) A quantitative description of sea ice inclusions. Journal of Geophysical Research C: Oceans 101(C8):18327–18343, DOI 10.1029/96JC01688

Peters GP, Nilssen TB, Lindholt L, Eide MS, Glomsrød S, Eide LI, Fuglestvedt JS (2011) Future emissions from shipping and petroleum activities in the Arctic. Atmospheric Chemistry and Physics 11(11):5305–5320, DOI 10.5194/acp-11-5305-2011

Petrich C, Eicken H (2016) Overview of sea ice growth and properties. In: Sea Ice: Third Edition, Wiley Blackwell, pp 1–41, DOI 10.1002/9781118778371.CH1

Petrich C, Karlsson J, Eicken H (2013) Porosity of growing sea ice and potential for oil entrainment. Cold Regions Science and Technology 87:27–32, DOI 10.1016/j.coldregions.2012.12.002

Petrich C, O'Sadnick M, Brekke C, Myrnes M, Maus S, Salomon ML, Woelk S, Grydeland T, Jenssen RO, Eicken H, Oggier M, Ferro-Famil L, Harkati L, Rebane O, Reimer N (2018) An overview of the Mosideo/Cirfa experiments on behavior and detection of oil in ice. In: 41st AMOP Technical Seminar on Environmental Contamination and Response, AMOP 2018, pp 112–122

Pringle DJ, Miner JE, Eicken H, Golden KM (2009) Pore space percolation in sea ice single crystals. Journal of Geophysical Research: Oceans 114(12):1–14, DOI 10.1029/2008JC005145

Pustogvar A, Kulyakhtin A (2016) Sea ice density measurements. Methods and uncertainties. Cold Regions Science and Technology 131:46–52, DOI 10.1016/j.coldregions.2016.09.001

Reay D, Sabine C, Smith P, Hymus G (2007) Intergovernmental Panel on Climate Change. Fourth Assessment Report. Geneva, Switzerland: Inter-gov- ernmental Panel on Climate Change. Cambridge; UK: Cambridge University Press; 2007. Available from: www. ipcc.ch. DOI 10.1038/446727a

Rutter JW, Chalmers B (1953) A PRISMATIC SUBSTRUCTURE FORMED DURING SOLIDIFICATION OF METALS. Canadian Journal of Physics 31(1):15–39, DOI 10.1139/p53-003

Salomon ML, Maus S, Arntsen M, Petrich C, Wilde F (2016) Distribution of oil in sea ice: Laboratory Experiments for 3-dimensional microCT investigations. In: Proceedings of the Twenty-sixth (2016) International Ocean and Polar Engineering Conference, Rhodes, Greece

Salomon ML, Arntsen M, Phuong ND, Maus S, O'Sadnick M, Petrich C, Schneebeli M, Wiese M (2017) Experimental and micro-CT study on the oil distribution in laboratory grown sea ice. In: Proceedings of the International Conference on Port and Ocean Engineering under Arctic Conditions, POAC, [Technical University of Norway]

Salomon ML, Maus S, Petrich C (2021) Microstructure evolution of young sea ice from a Svalbard fjord using micro-CT analysis. Journal of Glaciology pp 1–20, DOI 10.1017/JOG.2021.119

Schneider CA, Rasband WS, Eliceiri KW (2012) NIH Image to ImageJ: 25 years of image analysis. Nature Methods 2012 9:7 9(7):671–675, DOI 10.1038/nmeth.2089

Shokr M, Sinha N (2015) Sea Ice: Physics and Remote SensingTitle. John Wiley Sons

Sinha N (1977) Technique for Studying Structure of Sea Ice. Journal of Glaciology 18(79):315–324, DOI 10.3189/s0022143000021390

Själander M, Jahre M, Tufte G, Reissmann N (2019) EPIC : An Energy-Efficient , High-Performance GPGPU Computing Research Infrastructure. Tech. rep., Norwegian University of Science and Technology (NTNU), arXiv:1912.05848v4

Smith LC, Stephenson SR (2013) New Trans-Arctic shipping routes navigable by midcentury. Proceedings of the National Academy of Sciences of the United States of America 110(13):6–10, DOI 10.1073/pnas.1214212110

Stock SR (2018) MicroComputed Tomography. CRC Press, DOI 10.1201/9781420058772

Tsurikov VL (1979) THE FORMATION AND COMPOSITION OF THE GAS CONTENT OF SEA ICE. Journal of Glaciology 22(86)

Untersteiner N (1968) Natural desalination and equilibrium salinity profile of perennial sea ice. Journal of Geophysical Research 73(4):1251–1257, DOI 10.1029/JB073I004P01251

Vaughan D, Comiso J, Allison I, Carrasco J, Kaser G, Kwok R, Mote P, Murray T, Paul F, Ren J, Rignot E, Solomina O, Steffen K, Zhang T (2013) Observations: Cryosphere. In: Climate Change 2013 the Physical Science Basis: Working Group I Contribution to the Fifth Assessment Report of the Intergovernmental Panel on Climate Change, vol 9781107057, Cambridge University Press, Cambridge, United Kingdom and New York, NY, USA, pp 317–382, DOI 10.1017/CBO9781107415324.012

Weeks WF (2010) On Sea Ice - Willy Weeks - Google Bøker. University of Alaska Press, Fairbanks

Weeks WF, Hamilton WL, Woarsr WF, Urtron WLHQ, Branch MR (1962) Petrographic Characteristics of Young Sea Ice, Point Barrow, Alaska. Tech. rep., U.S Army Cold Regions Research and Engineering Laboratory, Hanover, New Hampchire

Weissenberger J, Dieckmann G, Gradinger R, Spindler M, Weissenberger, Jiirgen Dieckmann G, Gradinger R, Spindler M (1992) Sea ice: A cast technique to examine and analyze brine pockets and channel structure. Limnology and Oceanography 37(1):179–183, DOI 10.4319/lo.1992.37.1.0179

Whitman W (1926) Elimination of salt from sea-water ice. Journal of the Franklin Institute 202(3):321–322, DOI 10.1016/s0016-0032(26)91372-0

Wilkinson JP, Boyd T, Hagen B, Maksym T, Pegau S, Roman C, Singh H, Zabilansky L (2015) Detection and quantification of oil under sea ice: The view from below. Cold Regions Science and Technology 109:9–17, DOI 10.1016/j.coldregions.2014.08.004

Zack GW, Rogers WE, Latt SA (1977) Automatic measurement of sister chromatid exchange frequency. Journal of Histochemistry and Cytochemistry 25(7):741–753, DOI 10.1177/25.7.70454

Zubov N (1945) Arctic ice (Izdatel’stvo Glavsevmoputi). Translated for Air Force Cam-bridge Research Center by US Naval Oceano-graphic Office and American Meteorological Society

Part II

Papers

Declaration of authorship

- **Paper I**: Salomon, M. L., Maus, S., & Petrich, C. (2021). Microstructure evolution of young sea ice from a Svalbard fjord using micro-CT analysis. *Journal of Glaciology*, 1-20.
  The first author was responsible for designing and performing the experiment, μ- CT acquisition and data analysis. The co-authors helped periodically in the experimental work. The paper was structured and mainly written by the first author. Maus S. contributed to the writing, especially in discussing details on the total brine volume fraction dependence on the open and connected brine volume fraction. Discussions with the co-authors, comments and suggestions beneficially contributed to the writing of the manuscript.
- **Paper II**: Salomon, M. L., Maus, S., Petrich, C., & Høyland K. V. (2022). Quantitative analysis of oil and diesel distribution within sea ice pore space by micro-CT investigations. *submitted to the "Marine Pollution Bulletin"*.
  Petrich, C. was the leader of the experimental work. The first author was responsible for designing and performing the experimental part on the microstructural investigations of oil, μ- CT the acquisition and analysis of the data. Petrich, C. came with the initial idea on the pre-segementaton algorithm. The paper was structured and mainly written by the first author. Discussions with the co-authors, comments and suggestions beneficially contributed to the writing of the manuscript.
- **Paper III**: Salomon, M. L., Arntsen, M., Phuong, N. D., Maus, S., O'Sadnick, M., Petrich, C., Schneebeli, M. & Wiese, M. (2017). Experimental and Micro-CT Study on the Oil Distribution in Laboratory Grown Sea Ice. *In Proceedings of the International Conference on Port and Ocean Engineering Under Arctic Conditions*.
  The experimental work was conducted in cooperation with Arntsen, M.Phuong, N. D., Maus, S., O'Sadnick, M., Petrich. The first author was responsible for performing μ- CT acquisition and analysis of the data. The μ- CT acquisition at SLF was hosted and supported by Schneebeli, M. The paper was structured and mainly written by the first author. Discussions with Maus, S., and other co-authors, comments and suggestions beneficially contributed to the writing of the manuscript.
- **Paper IV**: Salomon, M. L., Maus, S., Arntsen, M., O'Sadnick, M., Petrich, C., & Wilde, F. (2016). Distribution of oil in sea ice: Laboratory Experiments for 3-dimensional microCT investigations. *In The 26th International Ocean and Polar Engineering Conference*.
  The experimental work was conducted in cooperation with Arntsen, M.Phuong, N. D., Maus, S., O'Sadnick, M., Petrich. The first author and Maus, S. were responsible for performing μ- CT acquisitions. The μ- CT acquisition at DESY was hosted and supported by Wilde, F. The paper was structured and mainly written by the first author. Discussions with Maus, S., and other co-authors, comments and suggestions beneficially contributed to the writing of the manuscript.

Paper I

Microstructure evolution of young sea ice from a Svalbard fjord using micro-CT analysis

Journal of Glaciology

Microstructure evolution of young sea ice from a Svalbard fjord using micro-CT analysis

Martina Lan Salomon[1,2], Sönke Maus[1] and Chris Petrich[3]

[1]Department of Civil and Environmental Engineering, The Norwegian University of Science and Technology (NTNU), Høgskoleringen 7a, 7034 Trondheim, Norway; [2]Arctic Technology Department, The University Centre on Svalbard (UNIS), P.O. Box 156, 9170 Longyearbyen, Norway and [3]SINTEF Narvik AS, Rombaksveien 47, 8517 Narvik, Norway

Article

Cite this article: Salomon ML, Maus S, Petrich C (2021). Microstructure evolution of young sea ice from a Svalbard fjord using micro-CT analysis. *Journal of Glaciology* 1–20. https://doi.org/10.1017/jog.2021.119

Received: 22 March 2021
Revised: 15 October 2021
Accepted: 18 October 2021

Keywords:
Sea ice; sea-ice geophysics; sea-ice growth and decay; ice coring; ice physics

Author for correspondence:
Martina Lan Salomon,
E-mail: martina.salomon@ntnu.no

Abstract

We analysed the three-dimensional microstructure of sea ice by means of X-ray-micro computed tomography. Microscopic (brine- and air- pore sizes, numbers and connectivity) and macroscopic (salinity, density, porosity) properties of young Arctic sea ice were analysed. The analysis is based on ice cores obtained during spring 2016. Centrifuging of brine prior to CT imaging has allowed us to derive confident relationships between the open, vertically connected and total porosity of young sea ice at relatively high temperatures. We analysed the dependence of the microscopic properties on vertical position and total brine porosity. Most bulk properties (salinity, density) and pore space properties (pore sizes and their distribution) show a strong dependence on total brine porosity, but did not change significantly over the course of the field work. However, significant changes were observed for pore numbers (decreasing over time) and pore connectivity (increasing over time). CT-based salinity determinations are subject to larger than standard uncertainties (from conductivity), while the CT method yields important information about the salinity contributions from closed and open pores. We also performed a comparison of CT-based air porosity with calculations based on density from hydrostatic weighing. The consistency is encouraging and gives confidence to our CT-based results.

Introduction

Sea ice is a key element in earth's climate system, it has an impact on the heat and moisture transfer between the ocean and the atmosphere and influences the global albedo (Ebert and Curry, 1993). Sea ice contains, unlike freshwater ice, brine in pore networks and inclusions. Often termed 'brine channels', these are the habitat to a whole ecosystem crucial for the arctic food web (Legendre and others, 1992). As the interest in exploring natural resources and shipping traffic in the Arctic is increasing (Peters and others, 2011), sea ice becomes an engineering challenge (Schwarz and Weeks, 1977). Human activities bear the risk of increased marine pollution and oil spills. The sea-ice porous space can act as a buffer (Petrich and others, 2013; Salomon and others, 2017; Desmond and others, 2021). Hence, physical, optical and mechanical characteristics of sea ice, relevant to its geophysical, biological and engineering properties, are strongly linked to its microstructure.

Early studies on sea-ice structure were mainly dominated by two-dimensional (2-D) macroscopic descriptions (cm-mm scale) of either vertical or horizontal sections. Destructive preparation of thin- or thick sections was necessary to allow studies on sea-ice structure. Based on such sections, Lake and Lewis (1970) illustrated the overall 3-D patterns of brine channels systems. Since then there have been a couple of microstructure studies based on optical thin section analysis summarised in Weeks (2010) and Shokr and Sinha (2015). Extended thin section analysis by electron microscope observation has resulted in detailed 2-D views of single brine inclusions (Sinha, 1977). 3-D insights and the application of X-ray computed tomography (CT) to sea-ice samples were first given by Kawamura (1988). This study allowed for the first time non-destructive observation of sea ice, with a resolution of 2 mm. Since then, advances in technology have allowed examination at much higher resolution with micro-X-ray CT (μ-CT). Applying μ-CT on laboratory sea ice has advanced understanding in the field. Golden and others (2007) and Pringle and others (2009) investigated brine inclusions within sea ice, its connectivity and permeability supporting the percolation theory. Crabeck and others (2016) conducted studies on the spatial distribution of gas bubbles and gas transport within sea ice. Insights into pollutant distribution within sea ice on the example of crude oil were given by Oggier and others (2019) and Petrich and others (2019). Eicken and others (2000) investigated microstructure and thermal evolution of brine inclusions with magnetic resonance imaging on laboratory and natural grown sea ice. The first μ-CT-images of field collected sea ice were published in 2009 (Maus and others, 2009; Obbard and others, 2009; Lieb-Lappen and others, 2017). To diminish the likelihood of changing pore structure during transport and storage from changing temperatures, Maus and others (2009) proposed a method that had earlier been used to obtain cast samples of the sea-ice pore space (Freitag, 1999; Weissenberger and others, 1992). Prior to μ-CT imaging, samples were transported close to their in situ temperature to the lab and were centrifuged. Removal of the brine allows that samples can be further stored and transported at sub-eutectic temperatures without altering the pore structure to reveal insights into pore size distribution and permeability of sea ice. These data were used to model oil entrapment in ice (Maus and others, 2009, 2013, 2015). This paper aims to investigate the sea-ice pore space, which is defined by its brine networks and air inclusions on a microscale. The physical parameters including sea-ice temperature, salinity, density, porosity, pore size, throat size and pore number per area were studied. Sea-ice density and salinity measurement based on CT-microstructural observation are compared with hydrostatical density evaluations and salinity determined from conductivity.

Methods

Study site

Fieldwork location was Sveasundet, south of Sveagruva in Van Mijenfjorden, Spitsbergen (77°53′13.0″ N 16°44′23.1″ E) (Fig. 1). From 16 March until 23 April 2016, eight site visits were conducted.

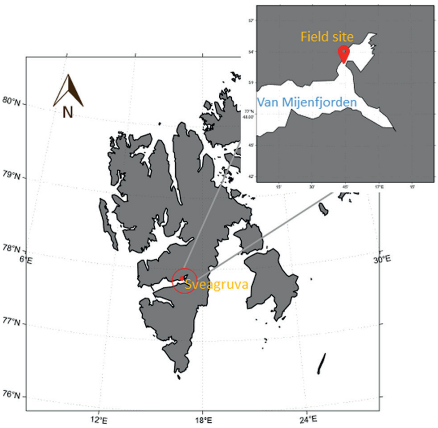

Fig. 1. Field work location: Sveasundet, south of Sveagruva in Van Mijenfjorden, Spitsbergen (77°53′13.0″ N 16°44′23.1″ E).

Field set-up

Field site preparation took place on 16 and 17 March 2017. Two sea-ice temperature profiles were logged throughout the field campaign, each with a set of six type T thermocouples. Registered sea-ice temperature was logged every 5 s with USB-5104 4-channel thermocouple loggers from Measurement Computing with a time accuracy of ±1 min per month at 25°C. Prior to the installation of the sea-ice temperature devices, thermocouples were mounted with a spacing of 10 cm inside a paperboard tube with an inner diameter of 7.8 cm and an outer diameter of 8.2 cm. An ice core with a diameter of 7.2 cm was drilled with a Kovacs 1 m core barrel and fitted into the paperboard tube. The tube equipped with thermocouples and filled with the ice core was re-positioned to its in situ position. The thermocouples were oriented such that one set of thermocouples was facing to the south and the other set was facing to the north. Unfortunately, the thermocouples started giving erroneous results after our second visit, probably due to a moisture problem.

A temperature sensor (SBE 56, Sea bird Scientific) with a resolution of 0.0001°C and an accuracy of ± 0.002°C (range: − 5 to + 35°C) was installed 1.2 m below the ice surface to register ocean temperatures. The ocean temperature was logged in an interval of 2 min.

Snow depth above the ice cover was measured at several locations on each field day with a commercial benchmark with a resolution of 1 mm. The snow temperature was measured at the surface as well as the slush-ice interface with a portable thermometer (HI 93510 from Hanna Instruments, accuracy: 0.4°C, resolution: 0.1°C).

After the installation of temperature loggers, two salinity cores, two temperature cores, two cores for microstructure analysis and one for density determination were drilled. This coring regime was repeated on 30 March, 06, 12 and 23 April.

All cores except cores from 30 March were drilled with a core barrel of 7.2 cm in diameter. Cores from 30 March were drilled with a core barrel of 12 cm in diameter, due to technical issues with the core barrel of 7.2 cm in diameter. Bulk salinity, temperature and density cores were drilled next to each other. Temperature cores were extracted one by one and measured immediately after coring. The temperature was measured with a portable thermometer (HI 93510 from Hanna Instruments) from bottom to top every 2.5 cm. Bulk salinity cores were measured in length and sub-sampled from bottom to top in 2.5 cm steps. Subsamples were packed into watertight plastic containers and transported back to the laboratory in Longyearbyen. Density cores were measured in length, sub-sampled to a height of 5 cm, packed into plastic containers and transported at ambient temperature in an upright position to the laboratory.

Microstructure cores were measured in length and sub-sampled to a height of 2.5 cm from bottom to top. The subsamples were packed in conical plastic boxes to avoid the sample touching the floor of the container and transported in an upright postion in active cooling boxes (WAECO T22,T32 and WAECO Cool Freeze CDF35) as close as possible to their in situ temperature to the UNIS laboratories.

Laboratory set up and methods

Bulk salinity (S_{ice}) of melted samples from the field was measured. We used a HI 98 188 conductivity/salinity meter from Hanna instruments to determine the salinity measured in practical salinity unit (psu). Sea-ice density (ρ) was determined by hydrostatic weighing in paraffin (Fritidsparafin by Wilhelmsen Chemicals), based on Archimedes' law (Kulyakhtin and others, 2013; Pustogvar and Kulyakhtin, 2016).

$$\rho_{\mathrm{ice}} = \frac{M_{\mathrm{air}}}{M_{\mathrm{air}} - M_{\mathrm{par}}} * \rho_{\mathrm{par}} \tag{1}$$

Ice samples were weighed in air (M_{air}) and submerged in paraffin (M_{par}) using a Kern KB 2000-2NM scale (resolution 0.01 g and accuracy 0.1 g). The paraffin density (ρ_{par}) was determined with an aerometer (resolution: 1 kg m^{-3}) to calculate the sea-ice density (Eqn (1)). Density measurements were performed in a cold lab at − 15°C, except for the cores from 17 and 30 March, which were measured at − 2.7°C. Air porosity from density was determined using equations by Cox and Weeks (1982), with density values from hydrostatic weighing and measured bulk salinity.

Samples for microstructure analysis were first weighed using a scale from PCE Group, BT 2000, and then reduced utilising a core barrel to a diameter of 4 cm. The cut-off from drilling was collected after this step. Afterwards, the reduced sample was centrifuged for 10 min at a set temperature of − 3°C and 900 revolutions per minute, corresponding to 40 G in a cooled centrifuger (Minifuge Heraeus Christ). The centrifuged samples were packed in plastic bags, stored at − 15°C and transported at this temperature to the Norwegian University of Technology (NTNU). Samples were stored at NTNU for 11 months at − 15°

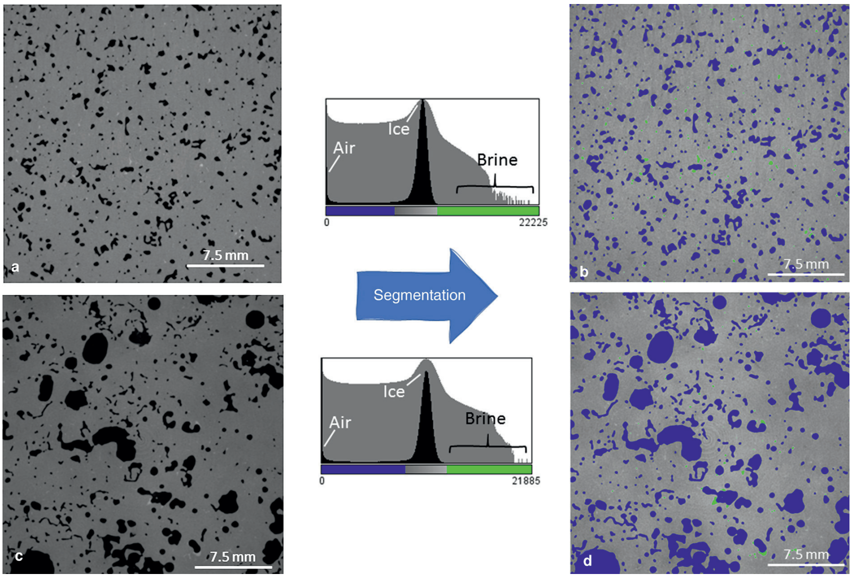

Fig. 2. Filtered grey scale CT-scans for (a) a sample with a small number of macro pores and (c) a large number of macro pores. Filtered data are segmented into air (blue), brine (green) and ice (grey). The histograms in the middle show the linear grey value distribution in black and the logarithmic distribution in grey with a significant ice peak.

C before further investigations. Centrifuging of ice samples makes it feasible to transport and investigate the microstructure of sea-ice samples, close to in situ conditions, without uncontrolled loss of brine and preserving the sea-ice microstructure. The amount and salinity of dripped brine (S_{bdrip}) during transport was determined, as well as the amount and salinity of the cut-off (S_{rest}) and the centrifuged brine (S_{bcent}). The salinity of the centrifuged microstructure samples (S_{cent}) was measured after μ-CT analysis at NTNU.

Micro computed-tomography imaging and post imaging processing

We conducted 3-D X-ray micro-tomographic imaging at the Norwegian Centre for X-ray Diffraction, Scattering and Imaging (RECX), NTNU, with a XT H 225 ST micro-CT system from Nikon Metrology NV, equipped with a Perkin Elmer 1620 flat panel detector with a 2048 × 2018 pixel field of view. Image acquisition was performed with a current source of 250 μA, an acceleration voltage of 150 kV and a Wolfram target. Scans were performed with 3142 rotation per 360° and an exposure time of 708.00 ms. The field of view (FOV) was 50 mm and corresponds to a pixel size of 25 μm. Samples were placed in an alumina sample holder with 1 mm wall thickness. The top and bottom temperature of the sample holder was controlled by a self-assembled cooling system, based on thermoelectric assemblies (www.lairdtech.com). The temperature during scanning was set to $-$ 15°C, the same temperature as during transport and storage. Nikon Metrology XT Software was used for reconstruction of the datasets. During reconstruction, we applied a beam hardening correction. Data were stored as 16-bit grey value stacks.

Data stacks were first processed in Image J. First, we cropped the cross-sections into a FOV of 1150 × 1150 pixel and cut to an average vertical extend of 400–650 slices. Images were then filtered using a combination of a Median filter (radius: 2 voxel) and a Gaussian filter (radius: 1.5 voxel), where a voxel is a 3-D pixel. In the next step, images are segmented into three classes: ice, air or brine. Otsu's algorithm (Otsu, 1979; Maus and others, 2015) was applied for differentiation between the air and ice signal. This was done in a semi-automatic manner. Therefore, five subareas in a 2-D slice were chosen. Each area contained a similar fraction of ice and air, on which the threshold based on Otsu's algorithm was computed. The mean of these thresholds was selected for air segmentation. For segmentation of brine from ice, the Triangle algorithm (Zack and others, 1977) was applied. The Triangle algorithm was chosen for brine segmentation, as Otsu's algorithm gave brine volumes that were too high (Hullar and Anastasio, 2016). First, the threshold was estimated for 41 samples, where in each of the samples five subregions containing a similar amount of brine and ice, without containing air, were investigated. Based on these 41 samples, it was found that the ratio of this threshold and the histogram peak corresponding to ice was 1.13 (±0.03). In the second step, brine segmentation was based on a threshold 1.13 times the ice histogram peak (Fig. 2).

Pore space analysis

Bulk properties: porosity, salinity and density

We used the software GeoDict 2018 and 2019 (Linden and others, 2018) to determine different porosity metrics of the pore space, salinity and density. We are interested in the following porosity metrics in situ:

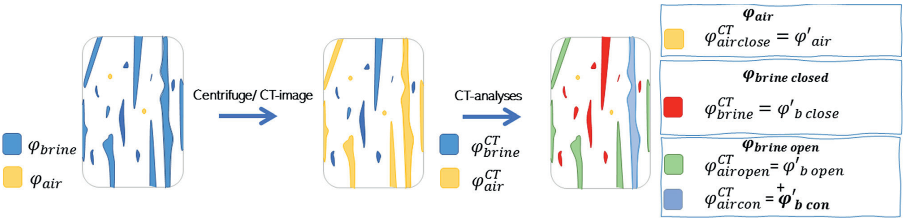

Fig. 3. Classification of pores under in situ conditions after sampling transport centrifuging and CT-imaging and after CT-image analysis.

ϕ_b = brine porosity
ϕ_{bopen} = open brine porosity
$\phi_{bclosed}$ = closed brine porosity
ϕ_{bcon} = connected brine porosity
ϕ_{air} = air porosity

The CT output is the segmentation into air and brine:

ϕ^{CT}_{brine} = brine and solid salt porosity in CT image (residual)
ϕ^{CT}_{air} = air porosity in CT image

The air porosity from the CT output consists of centrifuged brine pores and disconnected air pores. Open air pores might have existed, but are further considered as open brine pores. It can be further geometrically analysed by taking directional information into account (see Fig. 3 for illustration):

$\phi^{CT}_{air\ closed}$ = closed air porosity in CT image
$\phi^{CT}_{air\ open}$ = open air porosity in CT image
$\phi^{CT}_{air\ con}$ = vertically connected air porosity in CT image

In Geodict, the fractions of open and closed pores can be determined with respect to the six sides of a 3-D image. Where the x-axis (±) and the y-axis (±) do describe the horizontal plane and the z-axis (±) specifies the vertical position in the sample. The open porosity $\phi^{CT}_{airopen}$ contains all air pores connected to one of the sample surfaces in any Cartesian direction. A closed pore is considered to be isolated and unreachable from the surfaces. GeoDict does not distinguish connected pores. In order to calculate the connected pore fraction we looked into the open pore space from different intrusion directions: $z+$ (upper surface); $z-$ (lower surface) and $z\pm$ (upper and lower surface). The connected pore space can be calculated with the above described metrics as in Eqn (2). Firstly, pores opened to $z+$ and $z-$ direction are counted, the sum of these pores takes all opened pores into account. Since some of the opened pores are counted twice, as they were reached from both $z+$ and $z-$ directions, pores in $z+-$ direction need to be subtracted in a second step in order to get the true number of connected pores. For the example given in Figure 3, two air pores are reached from $z+$, three pores are opened towards $z-$, and four pores are opened in $z+-$ direction. Applying Eqn 2 on this example results in one connected pore. At this point, it should be noted that the connected porosity is a subset of the open porosity.

$$\varphi_{con} = \varphi_{z+} + \varphi_{z-} - \varphi_{z\pm}, \tag{2}$$

Air pores defined in this way are illustrated in Figure 3. Note that we do not divide the brine porosity, ϕ^{CT}_{brine}, into open and closed pores. In general, this could be useful to further refine the fraction of closed brine pores that may have been cut and emptied by centrifuging and thus resulted in open air pores. However, the open fraction was found to account for just a few per cent of residual brine and will not be considered here. Figure 3 illustrates how these CT-based porosity metrics are related to in situ metrics. Formally, we use the following relations:

$\phi'_{bopen} = \phi^{CT}_{airopen}$
$\phi'_{bcon} = \phi^{CT}_{aircon}$
$\phi'_{air} = \phi^{CT}_{airclosed}$
$\phi'_{bclosed} = f(T,\ T_{CT}\ \phi^{CT}_{brine})$
$\phi'_b = \phi'_{bopen} + \phi'_{bclosed}$,

where the prime denotes CT-image derived in situ porosities. Hence, pores classified as $\phi^{CT}_{airopen} \simeq \phi'_{bopen}$ in the CT image are identified with pores that were brine filled and open at in situ conditions and emptied by centrifuging. Closed air pores $\phi^{CT}_{airclosed} \simeq \phi'_{air}$ and connected brine pores $\phi^{CT}_{aircon} \simeq \phi'$bcon are directly identified in the CT images. The brine and solid salt porosity observed in the CT, ϕ^{CT}_{brine}, is identified with the disconnected brine and salt that could not be centrifuged. However, as CT imaging was performed at lower temperature (T_{CT}) than the in situ temperature (T) one needs to convert the closed brine fraction $\phi'_{bclosed}$ by a factor $f(T,\ T_{CT})$ to a higher temperature. We use the brine volume dependence from Cox and Weeks (1982, Eqn (6)), or $f = F1(T_{CT})/F1(T)$, to obtain this conversion factor with a small correction: as the conversion is between brine volumina, while the CT imaged brine porosity also contains solid salts, we divide f by 1.031 (F_{SS}) to account for this effect of solid salt volume at $T_{CT} = -15$°C.

Based on these porosity determinations, the CT-based bulk salinity in psu is obtained:

$$S_{CT} = \frac{\phi'_b \rho_b(T) S_b(T)}{\rho}, \tag{3}$$

where ρ_b and S_b are the brine density and brine salinity at temperature T. Furthermore, the ϕ'_b and ϕ'_{air} observations were used to estimate the density. First the ϕ'_{bopen} fraction needed to be converted from higher centrifuging temperature (T_{cent}) to lower T_{CT}. We used the brine volume dependence as described above to estimate the brine volume correction. In the density calculations based on CT measurements, the solid salt fraction in $\phi'_{bclosed}$ was calculated following Cox and Weeks (1982, Eqn (8)) at − 15°C.

$$F_{SS} = (c(T_{CT}) + 1) * \frac{\rho_b(T_{CT}) - \rho_{ss}(T_{CT})}{\rho_b(T_{CT})}. \tag{4}$$

Since the solid salt fraction is not resolved in the CT-scans, a factor F_{SS} of 1.031 was applied to calculate the solid salt fraction

Table 1. Field activities

Date	Work	H_{ice}	T_{ocean}	T_{ice}	S_{ice}	ρ_{ice}	μCT_{ice}
16 March	Prepare						
17 March	Prepare	35.6 cm	×	×	×	×	
30 March	Sampling	40.4 cm	×	×	×	×	×
06 April	Sampling	38.9 cm	×	×	×	×	×
12 April	Sampling	42.2 cm	×	×	×	×	×
23 April	Sampling	47.5 cm	×	×	×	×	×

from the volume brine fraction at − 15°C (Eqn (4)). c gives the phase relation between brine and the solid salt mass in brine in dependence of the temperature following Cox and Weeks (1982, Table 1). ρ_b and ρ_{ss} are the brine density and solid salt density at temperature T_{CT}.

$$\rho_{CT} = \rho_{air} * \phi'_{air} + \rho_b * \phi'_b + \rho_{ice} * (1 - \phi'_b - \phi'_{air}). \quad (5)$$

The bulk density was calculated using Eqn (5) at − 15°C, except for the cores from 17 and 30 March, which were performed at − 2.7°C.

Pore sizes

Two characteristic length scales are determined for the pore space:

(1) The pore size distribution (granulometry) (Fig. 18b) is determined by fitting spheres of different sizes into every single point of the pore volume. A point is classified by the diameter of the largest sphere that can be fitted in the pore around it. This frequency of sphere diameters is then binned into classes with 1 voxel (25 μm) bin size. Such a pore size distribution is determined for the pore space classified as closed and open air and brine, corresponding to ϕ'_{air}, ϕ'_{bopen} and $\phi'_{bclosed}$, respectively.

(2) The throat size distribution (porosimetry) (Fig. 18c) is not only based on the pore sizes alone, but also considers the connectivity of the pore space to the surfaces. In contrast to the pore size distribution, spheres are injected from the surfaces, and any point is classified by the largest sphere that can reach it via any path. For example, a larger pore that is reached via a bottle neck would be assigned the size of the bottle neck. Porosimetry was determined by considering injections from all sample surfaces and binned into classes with 1 voxel (25 μm) bin size. The approach is comparable to laboratory tests known as Mercury Intrusion Porosimetry (MIP) or Liquid Extrusion Porosimetry (LEP), yet it is a virtual experiment. Using MIP and LEP, a non-wetting fluid or gas is pressed through the pore space while measuring the absorbed volume and the applied pressure. It has recently been applied to analyse the oil uptake and saturation of the sea-ice pore space (Maus and others, 2015).

The pore and throat size distributions obtained with Geodict have been further analysed statistically in Matlab R2017b and R2019b. In particular, we aim to classify them into two size classes that we term micro- and macro-pores, with a division between them at 700 μm. This threshold was chosen, as this value corresponds to the sea-ice plate spacing (or brine layer spacing) at moderate growth rates of 0.5–2 cm d^{-1}(Weeks, 2010; Shokr and Sinha, 2015; Maus, 2020). This concept interprets macro pores as secondary pores that form by connection of original brine layers upon elimination of an ice subgrain or plate. The micro-porosity refers to the primary pores that are located within the elemental brine layers during columnar freezing of sea ice. Note that observed average growth rates between the field sampling dates were 0.3–1.0 cm d^{-1} and we consider 0.5–2 cm d^{-1} as typical for the upper 35–40 cm of the ice. Freitag (1999) has used a similar classification, yet with a larger threshold of 1.0 mm.

The pore size distribution results for ϕ'_{air}, $\phi'_{bclosed}$ and ϕ'_{bopen} were smoothed with a running mean over three pore classes. The pore size distribution per sampling day was calculated on the basis of two cores. The depth dependence of the mode (maximum in the distribution) and the median for the micro pores, as well as the median for the macro pores, were also determined by averaging results from two cores at each depth in the ice and for each sampling day. The same analysis was performed for the throat size distribution of ϕ'_{bopen}. For the overview in the discussion, the overall mode (maximum), median and mean of pore and throat size distributions were calculated for each sampling date, showing their evolution over time. Columnar and granular ice was distinguished on vertical CT-reconstructions, where elongated, vertical inclutions air inslucions (centrifuged brine) are characteristic for columnar ice and random orientation of air inclusions are interpreted as granular sea ice (Fig. 19). The boundary between granular and columnar ice per sampling day was interpreted on the basis of two cores.

Results

Sea-ice parameters including temperature, salinity and density are described in the following section. Observations of the sea-ice structure for the parameters for the porosity, number density, throat size and pore size are also described.

Bulk properties

Ice thickness

The average ice thickness gradually increases from 35.6 cm on 17 March, and towards 46.3 cm at the end of the experiment (23 April). The average ice growth over the entire experiment is 10.7 cm, with an average growth rate of 0.3 cm per day.

Temperature

In Figure 4a, we show air temperature observations from The Norwegian Meteorological institute (Sveagruva målestasjon, 99 760, 9 m a.s.l. 1 km from the site). The vertical black dotted lines indicate days with field work activity. Over the field period, the mean air temperature was − 11.1°C with a standard deviation of 7.5°C. The minimum of − 29.2°C was reached on 21 March and the maximum air temperature was observed on 23 April with 0.1°C. The coldest sampling day was 17 March with an average temperature of − 20.2°C. The highest air temperature on a sampling day was measured on 23 April with an average temperature of − 0.5°C.

Green and blue circles in Figure 4b give the temperatures observed at the snow surface and at the snow slush/sea-ice interface, respectively (this interface was slushy in all cases). Figure 4b shows temperature profiles collected on each sampling day in °C over the ice thickness in cm. The profiles are averaged over two temperature profiles per day, where 0 cm refers to the sea-ice surface. On 30 March, the temperature sensor broke, so no temperature profile measurements are available for this day. We have, however, results from the installed logger that worked properly until this date. Temperatures are relatively constant and vary, at any level in the ice, by < 0.5 K over the sampling period. The low near bottom temperature on 12 April is very likely erroneous due to cooling of the sample during measurements.

In Figure 4c, ocean temperatures in °C are shown over the course of the field work. Ocean temperature was recorded at a

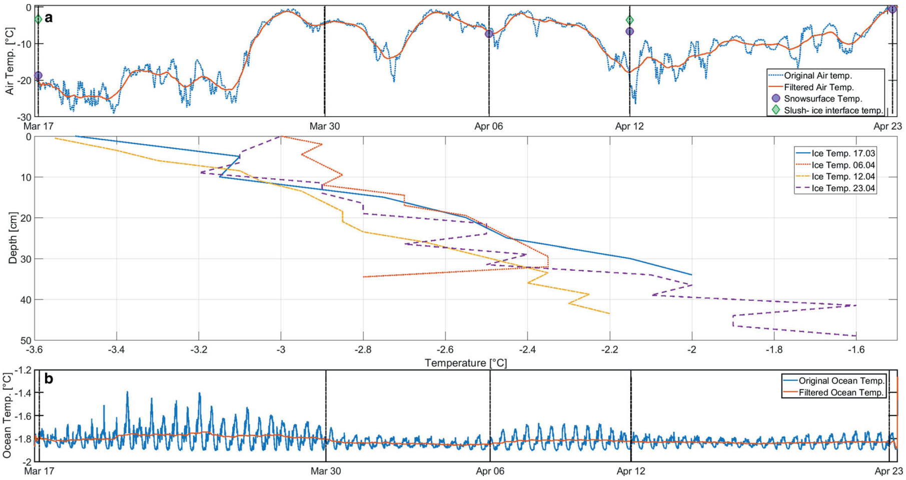

Fig. 4. Air, ice and ocean temperatures over the course of the fieldwork period from 17 March to 23 March 2016. (a) Blue line represents the original air temperature data, measured every hour from The Norwegian Meteorological institute at Sveagruva målestasjon (99 760) 9 m a.s.l. The red line shows air temperature data from the same source, filtered by a moving mean with an interval of 24 h. (b) Sea-ice temperature profiles over the course of the fieldwork period from 17 March to 23 April 2016. In dark blue the temperature profile for 17 March is shown, the red dotted line represents temperature measurements for the 06 April, temperature profile for 12 April is presented as the yellow line and the purple dashed line presents the temperature profile from 23 April. Measured snow surface temperature is presented as purple circles, snow-slush interface temperature is represented as green diamonds. (c) Ocean temperature measured at a depth of 1.2 m (0.7–0.8 m below the ice) is plotted in blue. The red line represents filtered data with a running mean of 24 h.

depth of 1.2 m below the ice-air interface. There is a strong tidal signal present. Removing the latter using a simple running mean of 24 h, the mean ocean temperature was −1.8°C with a standard deviation of 0.1°C. The minimum of −1.9°C was reached on 26 March and the maximum ocean temperature was observed on 23 April with − 1.3°C.

Salinity

In Figure 5, salinity profiles are shown for each sampling day over the course of the field work. The salinity in psu is plotted over the ice thickness in cm. For each sampling day, the values shown were averaged from two cores. The two profiles in Figures 5a–e correspond to salinity based on conductivity of melted samples (blue), further called S_{con}, and the salinity based on CT-scans (red), further referred to as S_{CT}. S_{CT} was calculated from porosity values at centrifuging temperature (mean −2.0°C) (Fig. 12a). S_{CT} data are not available for 17 March, when samples were lost due to a cooling box failure. The vertical resolution of the measured S_{con} as well as S_{CT} was 2.5 cm. However, S_{CT} are based on an approximately 10 times smaller volume. The salinity profiles based on the two methods are largely consistent with each other, while S_{CT} are smaller than S_{con} in the lower half of the ice. An exception to this is the very bottom on 30 March, yet here the cores had very different lengths. The vertical and time-averaged salinities, however, are consistent with each other with an average S_{con} of 6.7 psu with a standard deviation of 2.1 psu, and S_{CT} of 6.1 psu with a standard deviation of 4.2 psu. Note that all CT cores are slightly shorter because the weak skeletal layer was often destroyed during the cutting process.

Density

Density measurements are presented in Figures 5f–j. The plots show the density in kgm^{-3} over the measured ice thickness in cm. Hydrostatic density (ρ_{hydro}) profiles are plotted in blue. ρ_{hydro} was performed at −2.7°C for samples from 17 March and 30 March. ρ_{hydro} measurements from the remaining field days were performed at −15°C. Density calculations based on evaluated air and brine porosity from CT-images (ρ_{CT}) are presented in red. ρ_{CT} was calculated on porosities at the same temperature as ρ_{hydro} was conducted. On 17 March, samples for ρ_{CT} were lost due to cooling problems, hence no density was calculated. The overall average ρ_{hydro} from hydrostatic weighing is 900.5 kgm^{-3} with a standard deviation of 21.6 kgm^{-3}. In comparison, ρ_{CT} has a mean of 911.8 kgm^{-3} with a standard deviation of 9.8 kgm^{-3}. ρ_{CT} is on average 11.3 kgm^{-3} larger than ρ_{hydro}, with a standard deviation of 4.4 kgm^{-3}. The difference varies systematically over the thickness. Above a depth of 10 cm (with respect to the ice surface) the ρ_{CT} is higher than ρ_{hydro}, with differences of up to 20−80 kgm^{-3}. This upper part of the ice includes the freeboard and snow ice.

Porosity

The porosity is given as volume fraction in % over the total analysed sample volume, shown in Figure 6 for both air (a–e) and brine porosity (f–j). Brine porosity measurements based on CT scans (ϕ'_{b}) at centrifuging temperature (mean −2.0°C) in red are compared to brine porosity calculations based on salinity measurements ϕ_{brinecal} at in situ temperature assuming thermal equilibrium given by Cox and Weeks in blue. For air porosity, CT-based values ϕ'_{air} in red are compared to porosity estimates based on ρ_{hydro}, ϕ_{aircal} in blue. ϕ'_{bcon} shows the connected part of ϕ'_{b} presented in yellow. Again, all data points are based on averaging two cores, except for 17 March where CT samples were lost. It is seen that air porosities based on the two methods are largely consistent with each other, except in the upper 10–15 cm, where ϕ_{aircal} values are considerably larger. At the ice surface, air

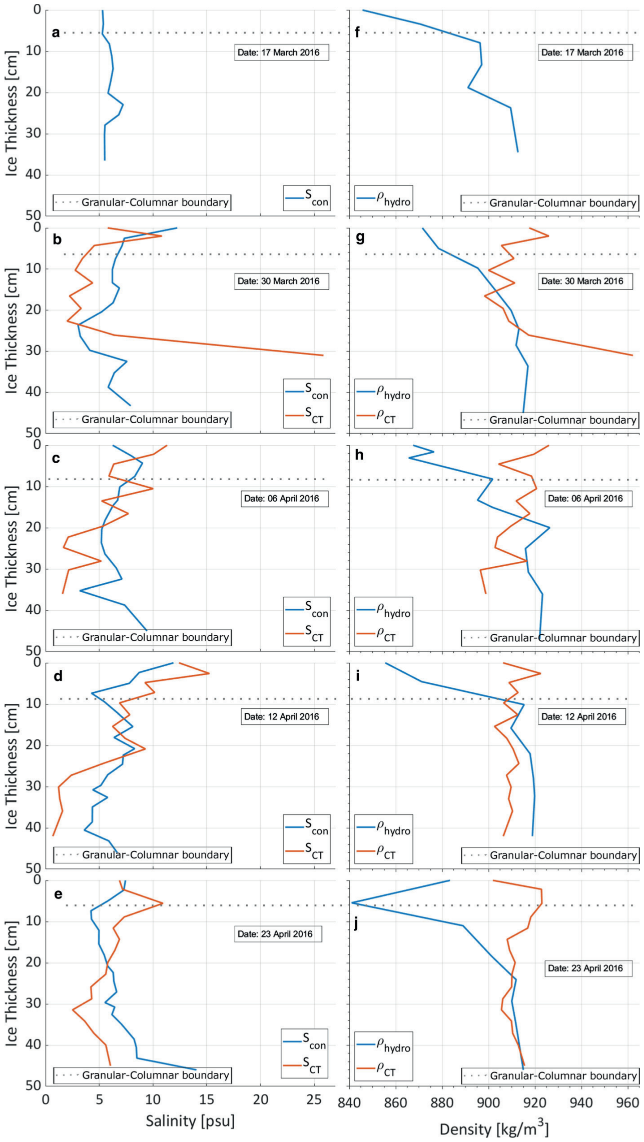

Fig. 5. Salinity profiles in psu and density proflies in kgm^{-3} plotted over the ice thickness in cm over the course of the fieldwork period from 17 March to 23 April 2016. 0 represents the sea-ice surface in contact with the atmosphere, numbers increase in depth towards the ocean. Grey dotted line represnets the boundary between columnar and granular ice. (a–e) Blue line represents conductivity measured salinity S_{con} plotted over ice thickness and red shows the calculated salinity from porosity observed in CT-scans S_{CT} at centrifuging temperature. (f–j) Blue line represents measurements from hydrostatic weighing ρ_{hydro} and the red line presents calculated density from CT-Data ρ_{CT}. ρ_{hydro} and ρ_{CT} at −2.7°C for 17 and 30 March and at −15°C for the sampling days in April.

porosity ϕ_{aircal} based on hydrostatic density ρ_{hydro} measurements reaches values from 3 to 9 vol.%. ϕ_{aircal} shows a mean of 2.6 vol.% with a standard deviation of 2.0 vol.% and is by an average of 0.8 vol.% with a standard deviation of 0.6 vol.% larger than ϕ'_{air}. ϕ'_{air} has a mean value of 1.6 vol.% with a standard deviation of 0.6 vol.% Total ϕ'_b shows a mean of 17.8 vol.% with a standard

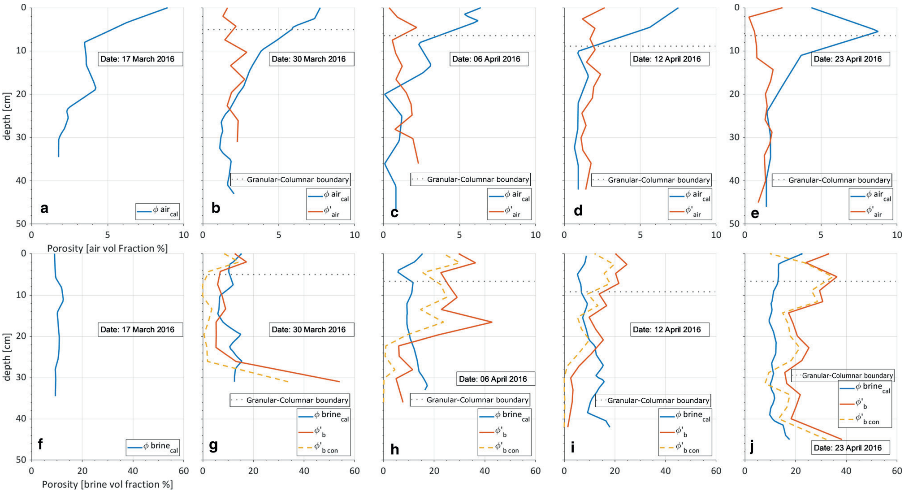

Fig. 6. Total air ϕ'_{air}, brine porosity ϕ'_b and connected brine porosity ϕ'_{bcon} in depth. Porosity in volume fraction % over the total sample volume. Ice thickness measured in cm, 0 is ice surface. Number increase as ice thickness increase towards the ocean. Blue line presents theoretical air ϕ_{aircal} and brine porosity $\phi_{brinecal}$ according to Cox and Weeks at in situ temperature. Red line shows porosity data for brine ϕ'_b and air ϕ'_{air} at centrifuging temperature observed from CT-images. Yellow line presents connected brine porosity ϕ'_{bcon}. Grey dotted line represnets the boundary between columnar and granular ice. (a) Air porosity from 17 March at −2.7°C, in (b) air porosity from 30 March is shown at −2.7°C, (c) presents air porosity from 06 April at −15°C, (d) shows air porosity from 12 April at −15 °C and (e) represents air porosity from 23 April at −15°C. (f) Brine porosity from 17 March, in (g) brine porosity from the 30 March is shown, (h) presents brine porosity from 06 April, (i) shows brine porosity from 12 April and (j) represents brine porosity from 23 April.

deviation of 11.4 vol.% at centrifuging temperature (mean −2.0°C). Roughly two-third of ϕ'_b are connected, with ϕ'_{bcon} on average 12.2 vol.% and a standard deviation of 10.2 vol.%. ϕ'_{bcon} correspond to the vertically connected brine porosity fraction of ϕ'_{bopen}. ϕ'_{bopen} shows a mean of 14.8 vol. % with a standard deviation of 10.0 vol.%.

Pore scale characteristics

Pore number densities

We use two metrics for the number of pores in a sample, (i) the total number of open pores per area (OPN, for brine only) and (ii) the number of closed pores per volume (CPN for air and brine). The first is a measure of the number of connected brine channels; the second counts the air bubbles and brine inclusions. In Figure 7a, the profiles of OPN are based on counting the brine pores open to the lower side of the samples. Open pore numbers OPN fall between 5 and 50 per cm^2. Except an increase in the bottom 5 cm of the ice, they do not show a pronounced depth dependence. The number decreases during the field work period. The number density of closed brine pores CPN$_{brine}$ (Fig. 7b) falls mostly in the range 10^3 to 10^4 per cm^3. The profiles show an increase both towards the top and the bottom. The number density of closed air pores CPN$_{air}$ (Fig. 7c) falls mostly in the range 200 to 1000 per cm^3. The profiles also show an increase towards the top and the bottom. The profile from 23 April indicates vertical fluctuations with 5–10 cm thicker regimes of high and low pore numbers.

Pore size distributions

Pore and throat size distributions are presented in Figures 8–11a–d. The overall distribution for each sampling date from 30 March to 23 April is given for ϕ'_{air}, $\phi'_{bclosed}$, ϕ'_{bopen} and the throats. It is shown for a bin size of 25 μm as a volumetric distribution, rather than measuring the volume in each pore size class then counting their number. Again, all data points are based on an average of two cores per field day. The vertical dotted line indicates the separation into micro pores with pore sizes in the range 25 −700 μm and macro pores larger than 700 μm. The mode (maximum) and the median for the micro pores are presented as a red circle and a yellow square respectively. The median for macro pores is shown as a purple star. Analyses of the micro and macro pore fraction show that most of the pores appear as micro pores. The spatial resolution of the pore and throat size distribution is given in Figures 8–11e–h as the spatial resolution of the micro median and mode and the macro median in μm over the sea-ice thickness in cm. The median for micro pores is presented as a solid blue line, mode for micro air pores is shown as a dash-dotted green line, and the red solid line represents the median for macro pores.

Air pores

The air pore size distribution is presented in Figure 8 for the four sampling dates. The distribution shows the broadest spectrum of pore sizes on 30 March with pore sizes up to 2575 μm. The micro mode typically lay in the range of 200–225 μm. The micro median is also here slightly larger with typical values from 225 to 275 μm. No change in these characteristics is apparent over time. For the macro pores, the mode decreases from 1000 μm to 800 μm over time. This, however, is related to two samples from 30 March (at 3 and 25 cm depth) with some extremely large pores. The macro pores show a larger vertical variation with the biggest variety at the very beginning of the experiment. The smallest air pore medians are, for both the micro and macro pores, observed near the ice-ocean interface.

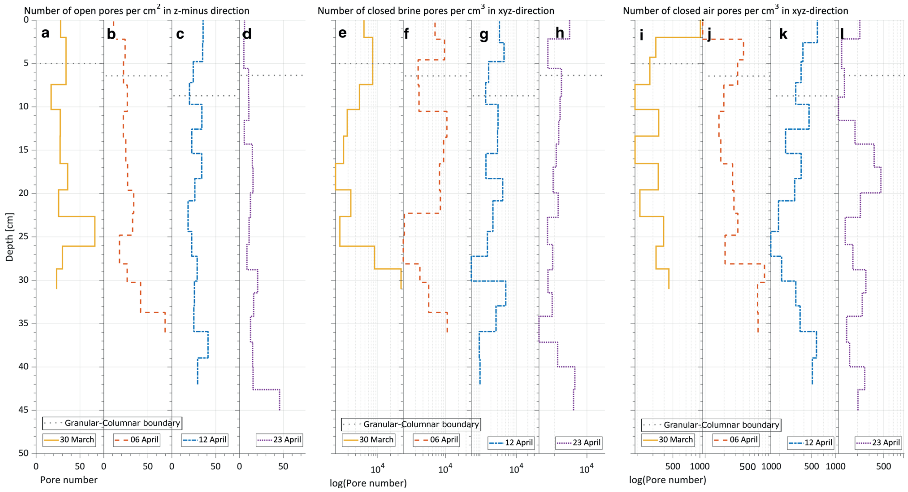

Fig. 7. Number of pores per area in cm^2, respectively by volume cm^3 over ice thickness in cm. Grey dotted line represnets the boundary between columnar and granular ice. (a–d) Number of open pores per cm^2 in *z*-minus direction. (e–h) Number of closed brine pores per cm^3 in *xyz*-direction. (k–l) Number of closed air pores per cm^3 in *xyz*-direction. The yellow line shows results for 30 March, red dashed line for 06 April, blue dashed dotted line for 12 April and the purple dotted line data for 23 April.

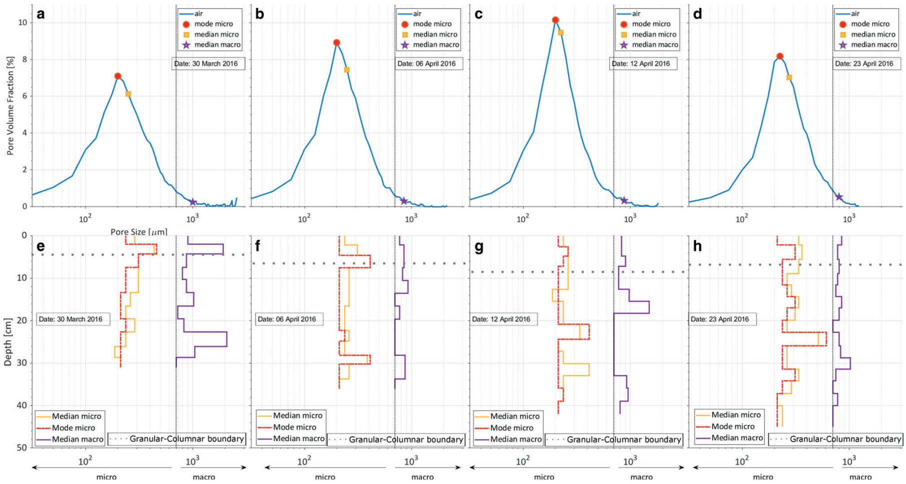

Fig. 8. Pore size distribution for air porosity. (a–d) Pore volume fraction for air in % plotted against the pore size in μm. Red circle presents mode, yellow square marks median of micro pores and the purple star represents the macro median. (e–h) Median and mode for air pore size distribution in μm plotted over ice thickness in cm. Grey dotted line represnets the boundary between columnar and granular ice.

Closed brine pores

Pore size distribution of the closed brine fraction at −15°C shows pore sizes up to 875 μm (Fig. 9). Most pores are smaller than 700 μm, and just an insignificant part of the pores can be found in the spectrum of the macro pores. Therefore no differentiation between micro and macro pores for the closed brine fraction is made. A constant mode of 50 μm is found over all the sampling days, with the median varying between 75 and 100 μm. These values indicate the limitation in our spatial resolution (Nyquist limit of two times voxel size is 50 μm). For both the mode and the median, no significant evolution over time and temperature can be observed. The spatial distribution over median and mode for the brine closed volume fraction are typically found between 60 and 160 μm.

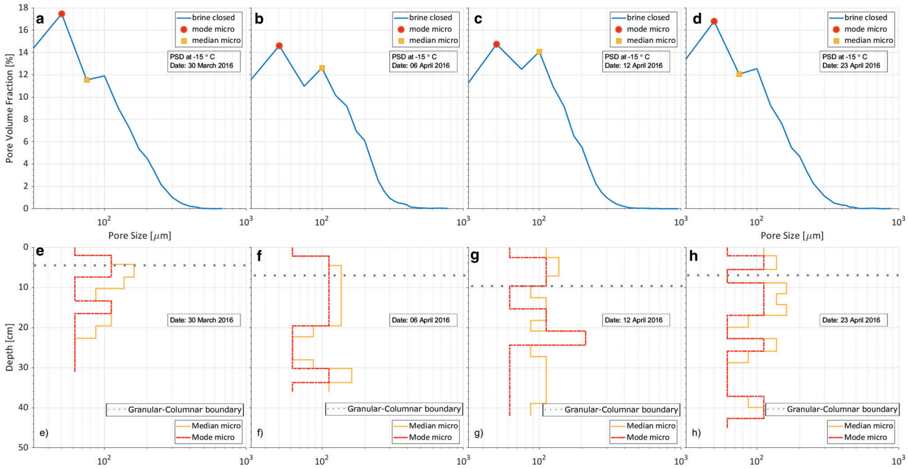

Fig. 9. Pore size distribution for closed brine porosity at − 15°C. (a–d) Pore volume fraction for closed brine in % plotted against the pore size in μm. Red circle presents mode and yellow square marks median of micro pores. (e–h) Median and mode for closed brine at − 15°C pore size distribution in μm plotted over ice thickness in cm. Grey dotted line represnets the boundary between columnar and granular ice.

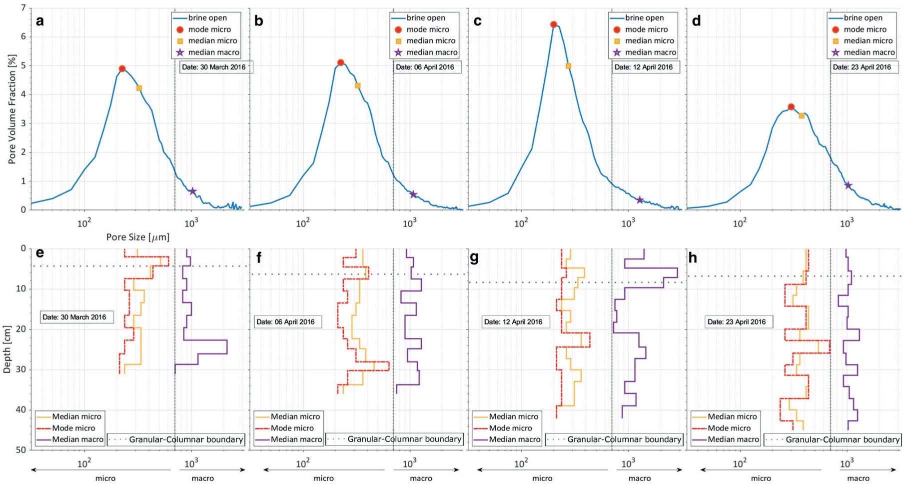

Fig. 10. Pore size distribution for open brine porosity. (a–d) Pore volume fraction for open brine in % plotted against the pore size in μm. Red circle presents mode, yellow square marks median of micro pores and the purple star represents the macro median. (e–h) Median and mode for open brine pore size distribution in μm plotted over ice thickness in cm. Grey dotted line represnets the boundary between columnar and granular ice.

Open brine pores

Pore size distribution for the open brine volume fraction shows a spectrum up to 3125 μm (Fig. 10). The micro mode can be found between 200 and 300 μm and the micro median ranges from 275 −375 μm. The macro pore median varies from 1025 −1275 μm. The biggest macro pore median is found on 12 April in the top 4–10 cm. The smallest macro pore median can be found in the bottom most samples towards the ocean interface.

Throat size distribution

The throat size distribution (Fig. 11) stretches up to 7425 μm with constant micro modes and a value of 200 μm. The micro median varies from 275−375 μm, the minimum can be seen on 12 April and the maximum on 23 April. The macro pore median increases from 1075 μm on 30 March up to 1275 μm before it decreases again to the minimum macro median of 975 μm on 23 April. Spatial resolution of the micro median and mode varies typically

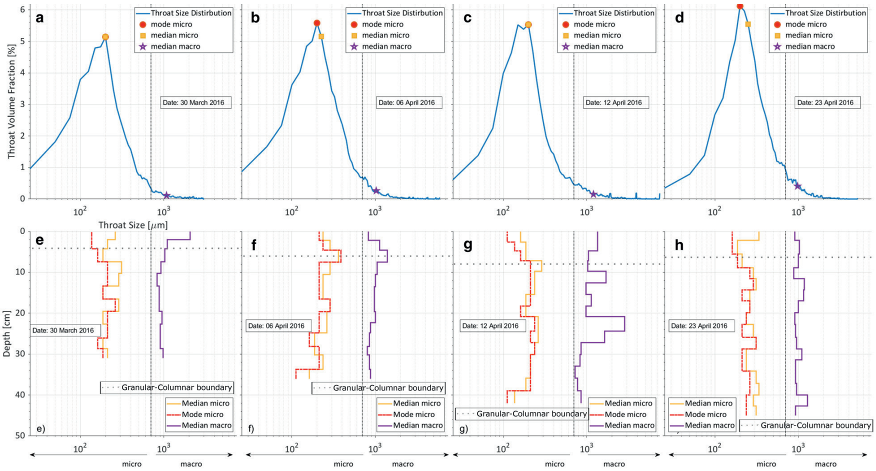

Fig. 11. Throat size distribution for open brine porosity. (a–d) Throat volume fraction for open brine in % plotted against the pore size in μm. Red circle presents mode, yellow square marks median of micro pores and the purple star represents the macro median. (e–h) Median and mode for throat size distribution in μm plotted over ice thickness in cm. Grey dotted line represnets the boundary between columnar and granular ice.

from 125–375 μm. The spatial resolution of the macro median ranges from 725–2852 μm with the maximum found on 12 April.

Discussion

The goal of our study has been to obtain 3-D microstructure information on natural sea ice that reflects its in situ stage as closely as possible. This is a challenge because on the one hand we have to minimise changes in sea-ice microstructure due to temperature, internal freezing and brine drainage, and on the other hand we need to ensure that samples are sufficiently stable during 3-D μCT acquisition of up to several hours. Moreover, the approach requires sufficient X-ray contrast to distinguish between ice and brine. To do so, we have applied a three-step procedure. First, we have transported and stored sea-ice samples at temperatures close to their in situ values in the field. Next, we have centrifuged these samples on the following day (also close to their in situ temperatures), which removes the highly mobile connected brine volume fractions. Finally, we have stored these samples at low temperatures until X-ray scanning. The latter approach is essential to obtain high-quality images for pore space analysis at high temperatures Maus (2020). Other approaches, like adding a contrast agent (Pringle and others, 2009) or imaging samples at high enough brine concentration and low temperature (Obbard and others, 2009), are not practical for warm natural sea ice. Overall, the procedures bear potential for a number of errors and biases, of which the following are considered most important:

(1) Transport and storage have been performed with mobile freezers with a nominal temperature accuracy of ± 0.5 K, which can be improved by calibration with other temperature sensors. However, we found that the response of the temperature control of the mobile freezers was less predictable for rapidly changing environmental conditions (from − 20°C in the field to 10–20°C in different labs and storage rooms).

(2) A similar problem as for the transport and storage was observed with the temperature stability in the centrifuge. Overall, this resulted in sample temperatures during processing that were 0.3–1.3 K lower than in situ values.

(3) The quality of salinity calculations based on CT observations depends on several factors related to the determination of the salinity in open and closed pores. For the open pores the assumption is made that all these pores were filled with brine with the same salinity as the centrifuged brine. This assumption may be wrong in the upper part of the ice including the freeboard and snow-ice, where pores may have drained. For the closed brine-filled pores, the quality depends on the spatial resolution and the question of how many pores have sizes below the latter and thus remain undetected. It also depends on proper choice of the segmentation threshold.

Despite these problems in obtaining CT images exactly at in situ conditions, the present study has not only collected a new dataset of 3-D microstructure and pore scale properties of young sea ice, but has also provided information about the change of these properties over the course of 3 1/2 weeks. In the following discussion, the focus will be on sea-ice bulk and pore space property changes over time and on its dependence on the brine porosity ϕ'b. The vertically averaged bulk properties and pore space characteristics for the sampling dates are summarised in Figures 12 and 13.

Bulk properties

Temperature

Over the course of the field work, the temperature gradient was relatively weak. This made it feasible to transport and centrifuge the ice close to its in situ temperature with limited logistics. The comparison of the average ice temperature per day with the average centrifuge temperature (Fig. 12a) suggests that the centrifuge temperature, computed from the salinity of centrifuged brine, was systematically higher than the in situ ice temperature, with an average difference of 0.7°C. Larger temperature differences were observed in the uppermost and lowermost parts of the ice cores and are related to the above-mentioned imperfect temperature control. Since the difference was not constant (being 0.3 K on 30 March and 12 April compared to 1.2 K on 06 April and 23 April), this has to be taken into account in the interpretation of brine fraction

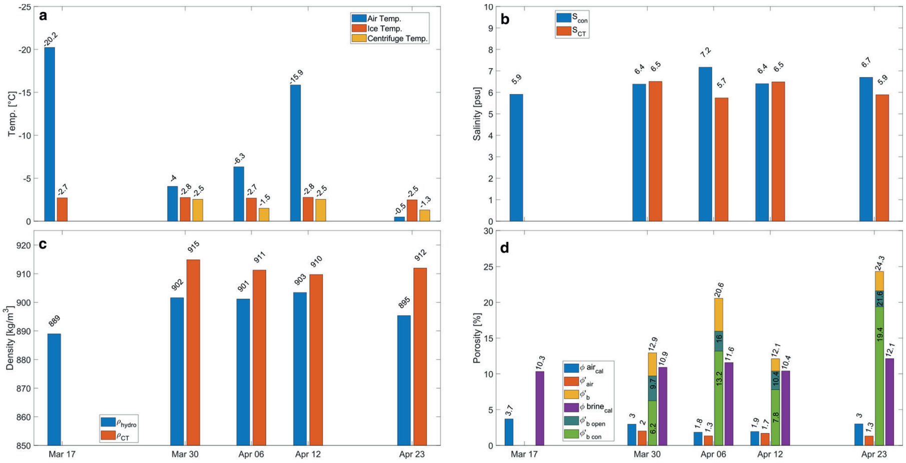

Fig. 12. Overview over measured parameters: (a) average air temperature in °C for each sampling day, plotted in blue. Average ice temperature for each sampling day over ice depth plotted in red. (b) Average measured salinity S_{con} for each sampling day over ice depth in psu plotted in blue. Mean salinity in psu calculated S_{CT} for each sampling day at centrifuge temperature over ice depth, observed from brine porosity in CT-scans are shown in red. (c) Average hydro-static determined density ρ_{hydro} in kg/m^3 for each sampling day over ice depth plotted in blue. Calculated density ρ_{CT} from CT-images plotted in red. (d) In blue theoretical air porosity ϕ_{aircal} following Cox and weeks in vol. %, in red air porosity observed from CT-images ϕ'_{air}, in yellow the observed brine porosity from CT-scans ϕ'_{b} at centrifuge temperature, in purple the theoretical brine porosity $\phi'_{\mathrm{brinecal}}$ at in situ temperature following Cox and weeks, in dark green the open brine porosity ϕ'_{bopen} at centrifuge temperature and in light green the connected brine porosity at centrifuge temperature ϕ'_{bcon} for each sampling day over the ice depth is shown.

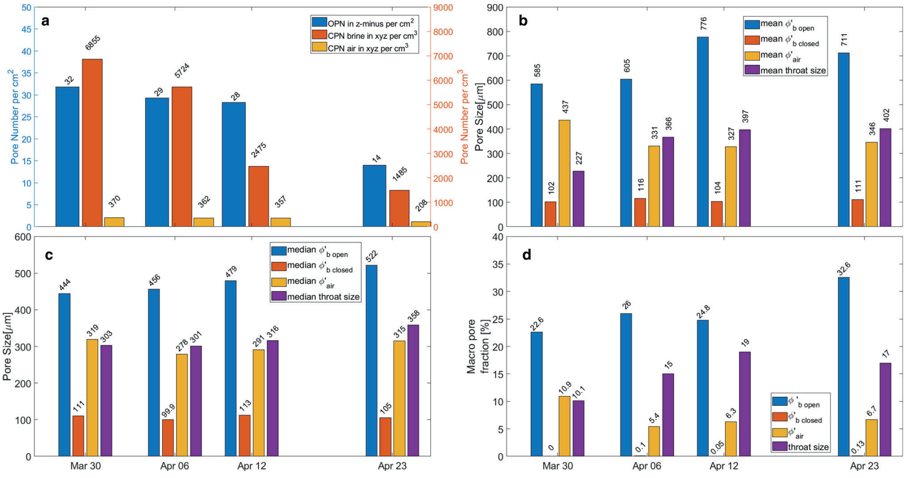

Fig. 13. Overview over measured parameters: (a) average OPN in z-minus direction per cm^2 for each sampling day, plotted in blue. Average CPN$_{\mathrm{brine}}$ in xyz-minus direction per cm^3 for each sampling day plotted in red and the average CPN$_{\mathrm{air}}$ per cm^3 in yellow. (b) Mean pore size in μm for ϕ'_{bopen} plotted for each day in blue, ϕ'_{bclosed} in red, ϕ'_{air} in yellow and the mean throat size in purple for each day at a temperature of −15 <. (c) Median pore size in μm for ϕ'_{bopen} plotted for each day in blue, ϕ'_{bclosed} in red, ϕ'_{air} in yellow and the median throat size in purple for each day at −15 °C. (d) Macro pore fraction in % for ϕ'_{bopen} plotted for each day in blue, ϕ'_{bclosed} in red, ϕ'_{air} in yellow and the macro throat size in purple for each day at −15°C.

observations and all associated parameters as well as pores size changes, and will be discussed below.

Salinity

Figure 12 summarises the evolution of average temperature and salinity during our field work. The vertically averaged salinity S_{con} during our field work shows typical values in the range 5.9–7.4 psu, at the upper end of the range 3.5–6.5 ppt that Høyland (2009) reported for sea ice of a similar age (3–4 months) from different locations in Van Mijenfjorden. The average salinity did not change significantly during the field work. The average S_{CT} at temperature T_{CT} shows a mean of 6.1 psu with a standard deviation of 4.2 psu and is on average 0.6 psu lower than S_{con} (Fig. 12b) with a mean of 6.7 psu and a standard deviation of

2.1 psu. For the individual sampling dates, the differences range between 1.4 psu larger S_{con} and 0.1 psu larger S_{CT}. Natural variability between different cores, internal variability of samples and the fact that S_{con} is based on ten times smaller sample volumes may all contribute to the differences. The comparison between vertical profiles of S_{con} and S_{CT} shows broad agreement, yet considerable scatter (Fig. 5).

An underestimation of salinity based on CT data can result from resolution limitations in the CT images, as objects smaller than two times the voxel size of 25 μm pixel cannot be resolved (Nyquist–Shannon theorem). Looking at the pore size distribution of closed brine pores (Figs 9a–d) we find that around 16% of the closed pores have diameters of 2 voxel (50 μm) and 13% are in the 1 voxel size class of 25 μm. Combining this with our finding that the detected closed pores contain about one-sixth of the salt (see discussion below), these correspond to fractions of 3 and 2% of total brine porosity (and salinity). To estimate the number of undetected pores one would need reference data at a higher resolution. Light and others (2003) observed numerous brine pockets with a size below the resolution of this study, and as small as 10 μm, which they classified according to their length (in 2-D optical images) and their aspect ratio. Brine inclusions with diameters <50 μm in our study would roughly correspond to the classes of brine pockets with lengths <100 μm in their Figure 8, containing roughly 3% of the total brine volume. Hence, this comparison would not indicate a considerable fraction of undetected pockets. However, there is general lack of data on small inclusions, and Light and others (2003) noted that they were only able to visually detect 2/3 of the conductivity-based brine volume. Maus and others (2021) also noted the difficulty of segmenting brine, because ice has a similar absorption as a mixed air-brine pixel, ending up with uncertainties of 1% for closed brine porosity. Related to total porosity of 10–20%, this would change the salinity by 5–10% or 0.3–0.7 psu. Hence, the difference of $+0.8$ to -0.5 psu between conductivity and CT-based salinity is within the error bounds expected from image analysis and a resolution limit of brine pore detection.

However, more critical is the systematic vertical distribution of the difference, with S_{CT} larger than S_{con} in the upper ice, and lower in the lower portion of the ice. For the lower portion, a possible source of error is loss of brine during sampling. Normally, one would expect that S_{CT} based on the open pore space is not affected by the loss of brine during sampling. However, if slow brine loss is considered (leakage of brine during transport and prior to centrifuging), then the leaked brine would have a higher salinity than the centrifuged brine. Due to cutting samples to a smaller diameter prior to centrifuging, only the centrifuged brine salinity S_{cent} is considered to compute S_{CT} with Eqn (3), and this would lead to an underestimated S_{CT} value. In a different study, one of the authors determined that, during similar storage and transport procedures, 28% of the total connected brine (leaked and centrifuged) leaked out prior to centrifugation Maus and others (2021). If this brine had two times the centrifuged brine porosity, this would increase the bulk salinity due to connected brine pores by 28%. Considering that another 25% of salt is contained in closed brine pores, the bulk salinity would be underestimated by 20%, or for our profiles by 1–2 psu. A vice versa argumentation holds for the upper part of the ice – the freeboard. Here, the ice has drained naturally, many connected pores are empty, yet are interpreted as connected brine pores in the CT-based analysis. Hence, here the estimates of S_{CT} will overestimate the in situ salinity. Note that all these contributions could be quantified by accurate determination of the masses of leaked and centrifuged brine, which in our study by sampling and centrifuging samples of different diameters, was not done. However, the estimates indicate that differences between conductivity S_{con} and CT-based salinity S_{CT} of 3–4% as found near the bottom on 12 April cannot be explained by brine leakage alone. Here, the low salinity of the CT samples must be related to natural variability on a scale of a few centimeters.

Brine porosity

Salinity is a largely conservative property, while the brine porosity depends on temperature, and is thus different for the in situ and centrifuged-based calculations. Figure 6 shows that most centrifuge-based porosities are larger, simply because the centrifuge and storage temperatures were larger. We also see that the in situ porosities show a decrease towards the top, where the ice is colder, while the centrifuge and CT-based porosities often show an increase towards the ice surface. The reason for this is that the transport temperature for individual samples was often lower than the in situ temperature near the bottom, but larger than the surface in situ temperatures. The overall CT-based porosities cover the range of 2–40%, while the in situ values were in the range 5–18%, and most of this difference is temperature-related.

Density and air porosity

On average, the density based on hydrostatic weighing ρ_{hydro}, is smaller than the CT-based density ρ_{CT}, the mean difference being 11.3 kgm^{-3}, see Figure 12c. ρ_{hydro}, with a mean of 900.5 kgm^{-3}, has a much higher standard deviation of 21.6 kgm^{-3}, compared to ρ_{CT} with an average of 911.8 kgm^{-3} and a standard deviation of 9.8 kgm^{-3}. The difference between the density estimates is strongly dependent on the vertical position (Figs 5f–j). In the upper ice, including the freeboard and snow-ice, the CT-based densities are much larger, while in the rest of the ice, below 10–15 cm depth, the values are similar or the CT-based values are slightly lower. An exception to this, as for the salinity, is the bottom sample on 30 March, where an exceptionally high CT-based density is related to an exceptionally high salinity.

For the large difference between ρ_{hydro} and ρ_{CT} in the upper part of the ice cores, we have, as for the salinity, the following explanation. ρ_{CT} is calculated on the air and brine porosity observed from centrifuged samples, where the entire open air space was assumed to be brine filled at in situ conditions. However, as the brine in the upper part of the ice including the freeboard and snow-ice has often drained, and thus the open air space is not brine-filled, the latter assumption overestimates the density. The correct value at the surface is thus the hydrostatic density ρ_{hydro}. Below the freeboard, the values are much more consistent. Comparison of the density profiles without the uppermost 15 cm show a mean difference of 4.1 kgm^{-3} with a standard deviation of 7.7 kgm^{-3} where ρ_{hydro} tends to be larger than the ρ_{CT}. Temperatures during CT core storage and centrifuging were larger than in situ values in the upper ice, and lower near the ice bottom. This may result in lower ρ_{CT} near the bottom and larger values close to the top. Nakawo and Sinha (1981) describes decreasing density profiles and an increase in air porosity towards the top, as it is observed from ρ_{hydro} profiles in Figures 5f–j and 6a–e.

Based on the same consideration, it follows that the CT-based air volume fraction ϕ'_{air} is underestimated in the upper part of the ice including the freeboard and snow-ice (see Figs 6a–e). Averaging over the whole ice thickness gives a mean ϕ'_{air} of 1.6% with a standard deviation of 0.6%. The mean ϕ_{aircal} based on hydrostatic weighing is 2.6% with a standard deviation of 0.6%. The CT-based vertically averaged ϕ'_{air} is thus on average 0.8% smaller than ϕ_{aircal}. However, the CT-based air porosity ϕ'_{air} can be expected to be valid for ice below the freeboard. Comparison of ϕ'_{air} and ϕ_{aircal} without the top 15 cm, gives larger CT-based air porosities, with a mean difference of 0.4% in comparison to ϕ_{aircal} with a standard deviation of 0.5%. A look into the profiles indicates this difference may be related to natural

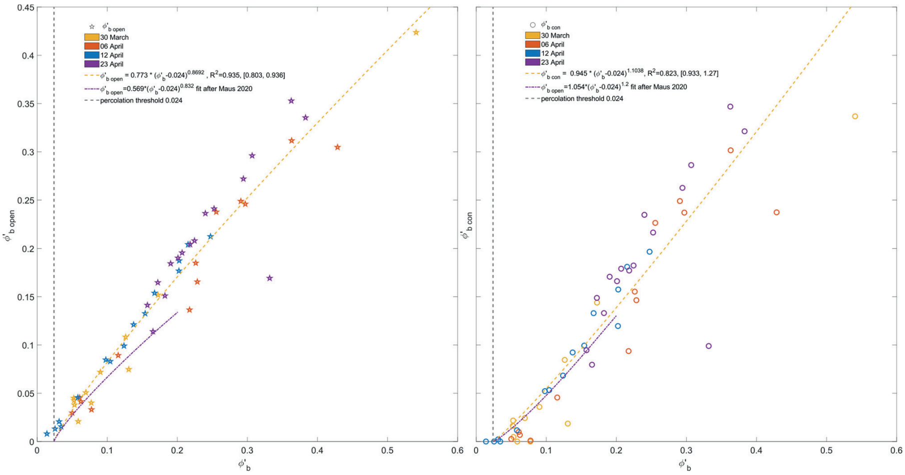

Fig. 14. (a) Open brine porosity ϕ'_{bopen} and (b) connected brine porosity ϕ'_{bcon} plotted against total brine volume fraction ϕ'_{b} for each day. 30 March is represented in yellow, 06 April is shown in red, 12 April is plotted in blue and 23 April is represented in purple. Grey line representing the percolation threshold. Yellow line least square fit for ϕ'_{bopen} and ϕ'_{bcon} against ϕ'_{b}. Purple line fit following Maus and others (2021) for total brine porosity ≤ 2%.

variability, but also resolution and/or measurement errors may be relevant. Firstly, CT-based air porosities may be too small due to undetected air pores below our spatial resolution. A look into the air pore size distribution in Figure 8 indicates that this effect is likely negligible for our samples. Secondly, the density calibration during hydrostatic weighing is limited by the aerometer's uncertainty to obtain the density of paraffin (in our case 0.2%). Thirdly, one could suspect that hydrostatic weighing overestimates the air porosity, because it cannot distinguish between leaked brine and closed air pores. The latter seems not to be a problem in our study. As air porosity is a rarely measured property, there are not many observations for comparison. Lieb-Lappen and others (2017) observed in a micro-CT study of non-centrifuged first year sea ice, that the air phase represents <1% in a volume of 7.5 mm^3. Nakawo (1983) has obtained air porosity based on density measurements as well as the volume of released gas during melting of samples. He reports a range 0.3–1% air porosity below the freeboard, and values of up to 5% in the freeboard of 1 m thick first-year ice. Values Nakawo (1983) reports are slightly below our observed range. Pustogvar and Kulyakhtin (2016) reports air porosities based on hydrostatic weighing, with similar values to what we found in the upper part of the ice. Below the freeboard they observe a range from 0.1 to 2.7%, which is comparable to our measurements, yet with larger variation. Crabeck and others (2016) observed, based on mass-volume density measurements, air volume fractions of 1–2% in the lowermost layer, in the middle part of the profiles air volume fractions of typically 1.5–4% and in the uppermost part 4–10%. However, these values were subject to large uncertainties, as the density was not obtained by the hydrostatic method. Crabeck and others (2016) obtained much lower CT-based air porosities, often less then half the density-based values (their Figure 10), in all levels of the ice. This underestimation can be attributed to their spatial resolution (pixel size 97 μm, Nyquist criterion of 194 μm). Since we find most median air pore sizes between 225 and 275 μm, see Figure 8, this would imply that roughly half of the air pore volume would not have been detected at such a resolution. Obbard and others (2009) reported an air volume fraction of 1.96% for one sea-ice sample imaged with a resolution of 15 μm and comparable to samples below the freeboard of the present study.

Pore space characteristics

Open and connected brine porosity

The CT-based values allow to determine the aspects of the pore space which are not given by the in situ bulk properties as the open brine porosity ϕ'_{bopen}, the closed brine porosity ϕ'_{bclosed} and the vertically connected brine porosity ϕ'_{bcon}. ϕ'_{bcon} ranges, with a vertical average over the four sampling dates, between 6.2 and 19.4% (Fig. 12), corresponding to 48–80% of the total brine porosity ϕ'_{b}. Individual values for ϕ'_{bcon} in dependence on ϕ'_{b} are plotted in Figure 14 and range from 0 to 35%. An almost linear increase in ϕ'_{bcon} with the total brine porosity ϕ'_{b} is observed. For a total brine porosity below 3% no vertical connection within the samples is found, e.g. near the bottom on 12 April, where the minimum CT-based salinities S_{CT} also occur (Fig. 5). ϕ'_{bopen} ranges with a vertical average between 9.7 and 21.6%. As the residual brine porosity ϕ'_{bclosed} is related to ϕ'_{bopen} by ($\phi'_{\mathrm{bclosed}} = 1 - \phi'_{\mathrm{bopen}}$) this corresponds to a relative closed brine pore fraction in the range of $11\% < \phi'_{\mathrm{b\ closed}}/\phi'_{\mathrm{b}} < 25\%$. This range is consistent with other centrifuge studies at high porosities and temperatures Maus and others (2021); Weissenberger and others (1992). The individual values of open brine porosity ϕ'_{bopen} are shown in Figure 14a dependent on the total porosity. A close to linear increase in open porosity with total brine porosity is apparent. Maus and others (2021) discusses ϕ'_{bopen} and ϕ'_{bcon}, and their dependency on ϕ'_{b} for slightly younger ice, and describes the relationship by

$$\phi'_{\mathrm{bopen}}/\phi'_{\mathrm{bcon}} = C(\phi'_{\mathrm{b}} - \phi_{\mathrm{bcrit}})^{\beta}, \tag{6}$$

where C is a constant and ϕ_{bcrit} is a threshold porosity that was determined as $\phi_{\mathrm{bcrit}} \simeq 0.024$ for young ice. The exponent β is related to the percolation theory. Maus and others (2021) determined $\beta \simeq 0.83$ for the open brine porosity ϕ'_{bopen} and as $\beta_2 \simeq 1.2$ for the connected brine porosity ϕ'_{bcon}, from data of columnar young ice in the

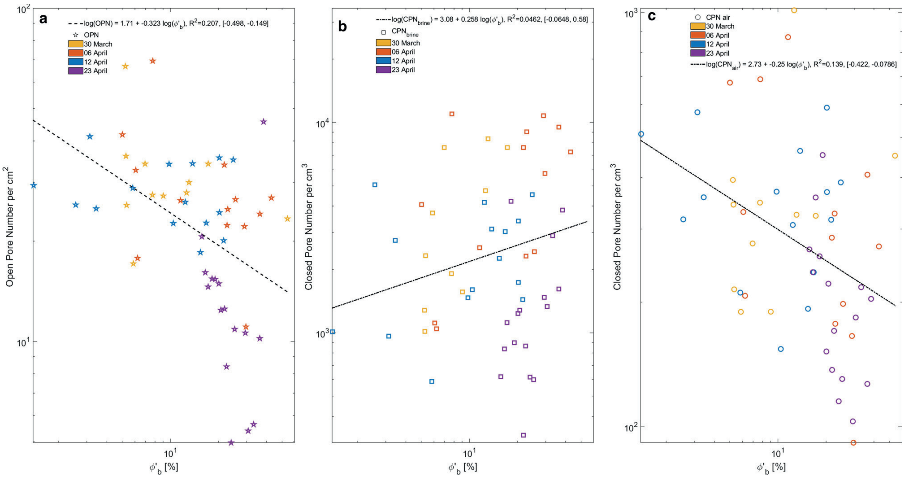

Fig. 15. (a) Open pore number per cm^2 in *z*-direction plotted against total volume brine fraction ϕ'_b for each day. (b) Closed brine pore number per cm^3 shown against the total brine volume fraction ϕ'_b. (c) Closed air pore number per cm^3 in *xyz*-direction plotted against total brine volume fraction ϕ'_b for each day. Yellow represents data from 30 March, red shows data from 06 April, in blue measurements from 12 April and in purple data points from 23 April.

porosity range of 1–20%. The relationships given by Maus and others (2021) are shown in Figures 14a and 14b as dashed magenta curves. In the present study, little data close to the percolation threshold were found, thus an assumption of $\phi_{bcrit} \simeq 0.024$ is made, and obtained comparable fits by application of a double-logarithmic regression. For ϕ'_{bopen}, $\beta \simeq 0.87 \pm 0.07$, while for ϕ'_{bcon}, $\beta \simeq 1.10 \pm 0.17$ is found. As discussed by Maus and others (2021), the open brine porosity exponent is consistent with the theoretical estimate $\beta \simeq 0.82$ for directed percolation. Data presented are from ice cores taken over the period of one month, containing both columnar and granular ice, with a brine porosity ϕ'_b range from 1 to 55%, while Maus and others (2021) studied columnar ice sampled over one week, at lower temperatures and a brine porosity range from 1 to 20%. Data presented in our study start to deviate from the relationship given by Maus and others (2021) at porosities above 10–15%. Though there is overall good agreement between these studies, more detailed analysis should take differences in high and low porosity regimes and the difference between granular and columnar ice into account. The connected porosity ϕ'_{bcon} increases with a higher exponent $\beta \simeq 1.10 \pm 0.17$ than the open porosity, in close agreement with the exponent of $\beta \simeq 1.2 \pm 0.1$ by Maus and others (2021). Based on our least square fits, ϕ'_{bopen} and ϕ'_{bcon} match at a total brine porosity of 45%, where they both are predicted as 36.8%. Due to the uncertainties in the fits, we do not attribute a physical meaning to this value, but rather interpret it as a validity limit, as the connected porosity cannot be larger than the open porosity.

Figures 14a and 14b also indicate a difference between sampling dates, as seen when focussing on the colour code. For brine porosities above 20%, ϕ'_{bopen} and ϕ'_{bcon} values from 23 April at the same total brine porosity ϕ'_b, are higher than values from 06 April and 12 April. Hence, there appears to be a relative increase in the open porosity ϕ'_{bopen} and a corresponding decrease in the closed porosity $\phi'_{bclosed}$. This increase is only observed for the sampling date 23 April, but not between 30 March and 12 April, and thus it is not happening constantly over time. As shown in Figure 16 and discussed below, 23 April is also exceptional in terms of pore numbers. The evolution is thus consistent with a transition from a higher number of smaller and disconnected pores to a smaller number of connected pores with larger diameter and length.

Pore number density

Pore numbers shown in Figure 7 are further investigated depending on the total brine porosity in Figure 15. We recall that open brine pore numbers are given per cross-sectional area, while closed air and brine pore numbers are given per volume. The vertical average for the sampling dates is given in Figure 13, with a minimum for the OPN on 23 April with 14 pores per cm^2 and a maximum of 32 pores per cm^2 on 30 March. As seen in Figure 7a, the overall variation in OPN is between 5 and 80 per cm^2. A correlation between the measurements taken for the OPN and the brine porosity suggests a slight but significant decrease in OPN with increasing brine porosity (Fig. 15a). Most of this decrease is related to the much lower OPN on 23 April, compared to the other sampling dates.

For the CPN$_{brine}$ closed brine pore numbers, no significant trend dependent on the brine porosity ϕ'_b is observed (Fig. 15b). Most data fall in the range 1–10 pores per mm^3, with an average of 3.8 pores per mm^3 and a large standard deviation of 5.2 pores per mm^3. An exception to this are the significantly lower pore numbers from 23 April (on average 1.5 pores per mm^3). This change is consistent with the decrease in closed brine porosity $\phi'_{bclosed}$ described above, and likely related to merging, coarsening and opening of pores. The results can be compared to reported pore statistics from other studies. Light and others (2003) reported an average number density of 24 pores per mm^3 for thicker first-year ice. This higher number is likely related to the higher resolution in that study (down to 10 μm compared to our 25 μm voxel size). Our results are comparable to the brine pocket numbers reported by Perovich and Gow (1996) for young and first-year ice, being in the range 1–6.9 pores per mm^3. Perovich and Gow (1996) obtained these numbers from optical analysis of 2-D thin sections with a similar pixel size (0.03 mm) as in our study. It is noteworthy that Perovich and Gow (1996) found a complex change in number density of brine pockets with porosity: at high porosities they observed a

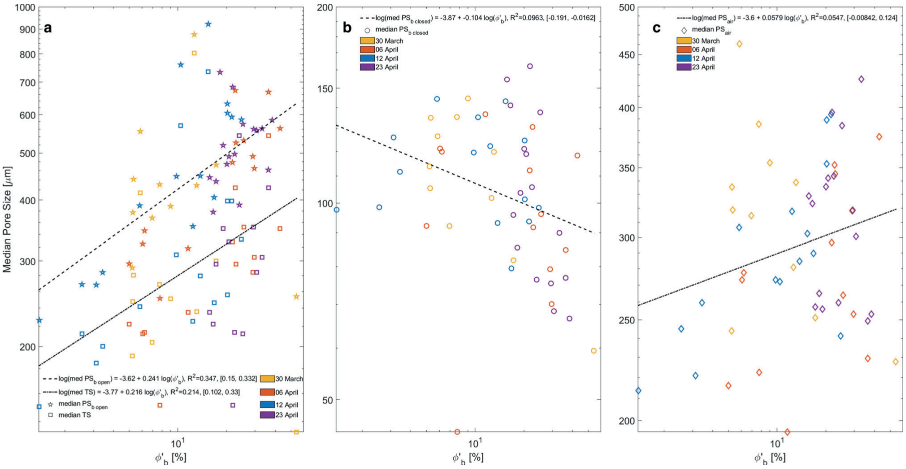

Fig. 16. (a) Median pore size in μm for ϕ'_{bopen} plotted with stars, throatsize represented as squares are plotted against the total brine volume ϕ'_{b} in % for each day. (b) Median pore size in μm for ϕ'_{bclosed} and (c) median pore size for ϕ'_{air} are plotted against ϕ'_{b} in % for each day. 30 March is represented in yellow, 06 April is shown in red, 12 April is plotted in blue and 23 April is represented in purple.

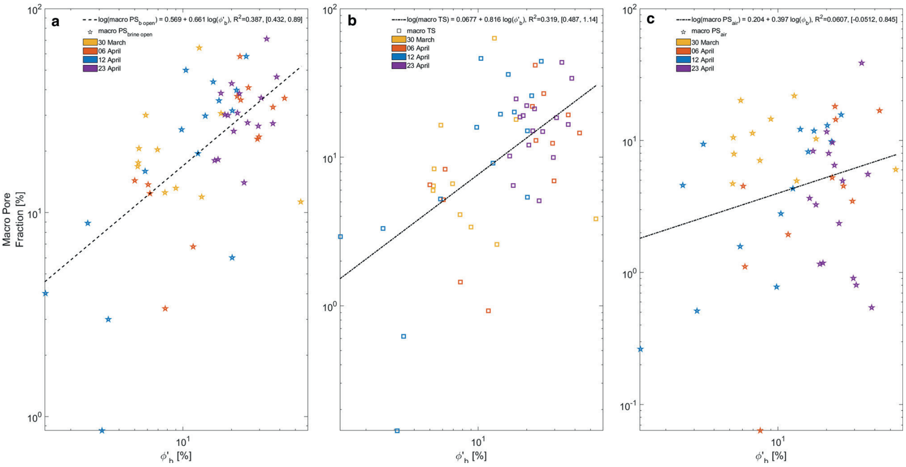

Fig. 17. (a) Macro pore size fraction in % for ϕ'_{bopen} (b) throatsize and (c) ϕ'_{air} the throatsize represented as diamonds are plotted against the total brine volume ϕ'_{b} in % for each day. 30 March is represented in yellow, 06 April is shown in red, 12 April is plotted in blue and 23 April is represented in purple.

decrease in the brine pore number densities with porosity, attributed to coalescence of pores. However, for the porosity range from 3 to 20%, they observed an increase which they attributed to the increase in pore sizes above their detectability threshold. Our data show too high variability to indicate such behaviour. However, we observe, for porosities above 15%, a continuous decrease in close brine pore numbers over time from 06 April to 23 April (seen in the colour coding in Fig. 15b).

The number densities of closed air pores, CPN$_{\mathrm{air}}$, are mostly found in the range 0.1–1 pores per mm^3, an order of magnitude of 10 smaller than for the closed brine pores CPN$_{\mathrm{brine}}$ (Fig. 15c), and with an average of 0.32 pores per mm^3. Also here, the decreasing trend with porosity is mostly related to the significantly lower pore numbers from 23 April (on average 1.5 pores per mm^3). This change is consistent with the decrease in closed brine porosity described above, and likely related to merging, coarsening and opening of pores. The results can be compared to reported pore statistics from other studies. Also here the average number density of 1.2 per mm^3 reported by Light and others (2003) is significantly larger, which again can be attributed to the higher resolution in the latter study. Light and others (2003) also reported earlier observations of air bubble numbers in young ice that were an order of magnitude lower than ours (0.03 pores per mm^3). Our study does not resolve the smallest air pores, but provides two other interesting findings. First, an observed decrease in air pore numbers at high porosities, that is likely attributable to the reopening and coalescence of brine pores. Second, as shown in Figures 7i–l, air pore numbers are larger near the bottom and surface of the ice, than in the middle.

Pore and throat size

Both the median (Fig. 16) as well as the macro pore fraction (Fig. 17) for the open pores and throat sizes show a significant increase with the total brine porosity ϕ'_b. Comparison of pore- and throat sizes shows that pore sizes are by a factor of roughly 1.5 larger (Fig. 16a). An increase in pore and throat sizes is expected during warming when internal melting increases the brine porosity and thus widens the pores. If no pores coalesce or split, a diameter $D \sim \phi_b'^{\,1/2}$ for brine tubes and $D \sim \phi_b'^{\,1/3}$ for spherical brine inclusions are expected. However, we observe smaller exponents of 0.24 for the median pore and 0.22 for throat diameters. This indicates a different pore widening process than for simple cylindrical pores. In general, this observation is not inconsistent for widening processes in sea ice. For example, if pores develop from original vertical brine layers, they tend to be anisotropic in a horizontal cross section Perovich and Gow (1996), if those pores primarily expand in longitudinal direction by dissolution of ice, the shorter direction of the pore (measured with the sphere fitting algorithm in Geodict) will be less affected by porosity changes.

A similar weak dependency of pore diameters on porosity has been observed by Perovich and Gow (1996) for a warming sequence. For young ice that was cooled than warmed prior to X-ray imaging, and with most data in the porosity regime between 3 and 15%, Maus and others (2021) obtained exponents of 0.34 for pore and 0.46 for throat sizes. Hence, the details of pore size redistribution during warming and cooling appear to be complex, and should be studied in more detail. The median throat and pore sizes obtained in the present study exceed those obtained by Maus and others (2021) by roughly a factor of 1.5. This may be attributed to the greater thickness and age of the present ice (2 months compared to 3 weeks in the latter study) and the higher number of wider brine channels in the older ice. It is further noted that neither for throat nor pore sizes exceptional values are observed for 23 April, quite in contrary to the pore numbers.

The pore sizes for closed brine PS_{bclosed} show an insignificant decrease in pore size with total brine porosity. This is not surprising, as the closed brine pores were all imaged at the same temperature of -15 °C, and were unaffected by the centrifuging technique and temperature. We interpret the slight decrease towards 06 and 23 April, for the warmer cores and higher porosity, with a likely merge between the larger brine pores and the open porosity, leaving pores with smaller diameters back.

Also for the closed air pores PS_{air} no significant correlation with the brine porosity was found, again not surprising as the samples were all scanned at the same temperature and air pores should not be affected by centrifuging. Most air pores median diameters fall between 200 and 450 μm. The air pore population from 23 April does not appear as exceptional as for other properties of the pore space.

Analysis of the throat sizes showed that between 0.3 and 2.5 vol. have a diameter above 2 mm and increases from 30 March (0.3 vol.) to 06 April (2.5 vol.) before it decreases towards 12 April (2.4 vol.) and increases again towards 23 April (1.3 vol.). Throats above 2 mm are just presented in the upper 7.5 cm in the beginning of the experiment, at the end of the experiment they could be found from the bottom to the top of the ice core 11.

Conclusion

We have observed macroscopic and microscopic properties of young Arctic sea ice over the course of 1 month, prior to the onset of melting. Microscopic properties have been derived from the combination of two non-destructive techniques (i) centrifuging of brine for separation of the connected and disconnected pore space and (ii) 3-D micro-CT imaging followed by analysis of the pore size characteristics. Our main findings are

1. Density and air porosity determinations based on hydrostatic weighing and CT images show good consistency within the range measurement accuracy (≈ 0.2 %) and natural variability (≈ 0.5 %).
2. CT-based salinity determinations are subject to larger than standard uncertainties. Since, we reached the limitation of spatial resolution to resolve brine pores, while the strength is to distinguish different porosity metrics and to give a better understanding of where the salt is located (open, closed, vertically connected).
3. The variation of different pore categories (open and closed brine pores, closed air pores) with vertical position in the ice is remarkably small – most variability is related to changes in the brine porosity.
4. Most bulk properties (salinity, density) and pore space properties (pore sizes, proportion of secondary ‘macro’ pores) remained constant, while we observe significant changes in pore numbers (decreasing over time) and pore connectivity (increasing over time).
5. We obtain confident relationships between the open (centrifuged) porosity ϕ'_{bopen}, connected ϕ'_{bcon} and total porosity ϕ'_{b} of young sea ice.
6. We further find that results are consistent with a connected brine porosity threshold of 2–3% as recently proposed by Maus and others (2021).

The agreement between our density and air porosity estimates ϕ'_{air} and ϕ_{CT} based on hydrostatic weighing and CT imaging below the freeboard is encouraging, as these properties have so far been mostly observed with high uncertainties. The difference in the upper part of the ice cores is related to our method centrifuging and imaging method, and would not be a problem for non-centrifuged samples. Here, future studies focussing on density only will be useful. The present approach, however, has provided important information about the morphology of the drained low-density surface regime, and the fractions of connected and disconnected air pores and will be useful to better understand the surface drainage and evolution of low-density layer.

The present study has provided pore space and pore size information with a spatial resolution (25 μm pixel/voxel size) two to four times better than in earlier work obtaining similar statistics on brine and air inclusions at relatively high temperature Eicken and others (2000), Crabeck and others (2016). To obtain pore sizes and connectivity metrics in this high temperature regime, centrifuging the samples is essential, as the absorption contrast between brine and ice would be too low to obtain high-quality 3-D images, with drainage during imaging being an additional problem. Imaging at a temperature as low as -15°C Obbard and others (2009), Lieb-Lappen and others (2017) would give sufficient contrast but cannot be used to derive the pore space connectivity metrics outlined here. Lieb-Lappen and others (2018) performed network analysis on CT-images on sea ice with an in situ temperature as high as −7°C, yet they found differences between the CT-derived and salinity-derived brine volumes that increased with temperature, exceeding a factor of two. Due to such uncertainties, concise observations and modelling of pore size, number and connectivity (e.g. Figs 14 and 15) remain challenging tasks. An important issue for future studies is the scale-dependence of properties (e.g. connectivity, permeability, percolation threshold), that should be addressed by scanning larger samples with a larger FOV.

Acknowledgements. We gratefully acknowledge Aleksey Marchenko for hosting us at the Arctic Technology Department at The University Center in Svalbard (UNIS), Alkesey Shestov and UNIS Logistics for assistance and expertise regarding field and laboratory work, as well as Ole Tore Buset and Leander Michels for guidance and help during CT measurements at the Norwegian University of Science and Technology (NTNU). A big thanks to the field assistants Astrid Strunk, Eef van Dongen and Sarah Elise Sapper. Special thanks to Math2Market, GeoDict for providing the imaging analysis software. This work was supported by the Research Council of Norway PETROMAKS2 program, project number 243812 (MOSIDEO) and the Arctic Field Grant (AFG).

References

Cox GF and Weeks WF (1982) Equations for determining the gas and brine volumes in sea ice samples. *CRREL Report (US Army Cold Regions Research and Engineering Laboratory)* **29**(102), 306–316. doi:10.3189/s0022143000008364

Crabeck O, Galley R, Delille B, Else B, Geilfus NX and 5 others (2016) Imaging air volume fraction in sea ice using non-destructive X-ray tomography. *Cryosphere* **10**(3), 1125–1145. doi:10.5194/tc-10-1125-2016

Desmond DS, Crabeck O, Lemes M, Harasyn ML, Mansoori A and 6 others (2021) Investigation into the geometry and distribution of oil inclusions in sea ice using non-destructive x-ray microtomography and its implications for remote sensing and mitigation potential. *Marine Pollution Bulletin* **173**, 112996. doi:10.1016/j.marpolbul.2021.112996

Ebert EE and Curry JA (1993) An intermediate one-dimensional thermodynamic sea ice model for investigating ice-atmosphere interactions. *Journal of Geophysical Research* **98**(6), 10085–10109. doi:10.1029/93jc00656

Eicken H, Bock C, Wittig R, Miller H and Poertner HO (2000) Magnetic resonance imaging of sea-ice pore fluids: methods and thermal evolution of pore microstructure. *Cold Regions Science and Technology* **31**(3), 207–225. doi:10.1016/S0165-232X(00)00016-1

Freitag J (1999) Untersuchungen zur Hydrologie des arktischen Meereises: Konsequenzen für den kleinskaligen Stofftransport. *Berichte zur Polarforschung* **325**, 1–170.

Golden KM, Eicken H, Heaton AL, Miner J, Pringle DJ and 1 others (2007) Thermal evolution of permeability and microstructure in sea ice. *Geophysical Research Letters* **34**(16), 2–7. doi:10.1029/2007GL030447

Høyland KV (2009) Ice thickness, growth and salinity in Van Mijenfjorden, Svalbard, Norway. *Polar Research* **28**(3), 339–352. doi:10.1111/j.1751-8369.2009.00133.x

Hullar T and Anastasio C (2016) Direct visualization of solute locations in laboratory ice samples. *Cryosphere* **10**(5), 2057–2068. doi:10.5194/tc-10-2057-2016

Kawamura T (1988) Observations of the internal structure of sea ice by X ray computed tomography. *Journal of Geophysical Research* **93**(C3), 2343. doi:10.1029/jc093ic03p02343

Kulyakhtin A, Kulyakhtin S and Løset S (2013) Measurements of thermodynamic properties of ice created by frozen sea spray. In Chung JS, Langen I, Kokkinis T and Wang AM eds. *Proceedings of the Twenty-third International Offshore and Polar Engineering Conference*. Anchorage, Alaska: The International Society of Offshore and Polar Engineers, 1104–1111.

Lake R and Lewis E (1970) Salt rejection by sea ice during growth. *Journal of Geophysical Research* **75**(3), 583–597. doi:10.1029/jc075i003p00583

Legendre L, Ackley S, Dieckmann G, Gulliksen B, Horner R and 5 others (1992) Ecology of sea ice biota. *Polar Biology* **12**(3–4), 429–444. doi:10.1007/bf00243114

Lieb-Lappen RM, Golden EJ and Obbard RW (2017) Metrics for interpreting the microstructure of sea ice using X-ray micro-computed tomography. *Cold Regions Science and Technology* **138**, 24–35. doi:10.1016/j.coldregions.2017.03.001

Lieb-Lappen RM, Kumar DD, Pauls SD and Obbard RW (2018) A network model for characterizing brine channels in sea ice. *Cryosphere* **12**(3), 1013–1026. doi:10.5194/tc-12-1013-2018

Light B, Maykut GA and Grenfell TC (2003) Effects of temperature on the microstructure of first-year Arctic sea ice. *Journal of Geophysical Research C: Oceans* **108**(2), 33–1. doi:10.1029/2001jc000887

Linden S, Cheng L and Wiegmann A (2018) *Specialized methods for direct numerical simulations in porous media*. (Technical Report). Math2Market GmbH (doi:10.30423/report.m2m-2018-01).

Maus S (2020) The plate spacing of sea ice. *Annals of Glaciology* **61**(83), 408–425. doi:10.1017/aog.2020.65

Maus S, Becker J, Leisinger S, Matzl M, Schneebeli M and 1 others (2015) Oil saturation of the sea ice pore space. *Proceedings of the 23rd International Conference on Port and Ocean Engineering under Arctic Conditions, POAC*, The International Society of Offshore and Polar Engineers, Trondheim, Norway.

Maus S, Huthwelker T, Enzmann F, Miedaner MM, Marone F and 3 others (2009) Synchrotron-based X-ray micro-tomography: insights into sea ice microstructure. *Proceedings of the Sixth Workshop on Baltic Sea Ice Climate.* University of Helsinki Department of Physics, Helsinki, Finland. 61, 28–45.

Maus S, Leisinger S, Matzl M, Schneebeli M and Wiegmann A (2013) Modelling oil entrapment in sea ice on the basis of 3d micro-tomographic images. *Proceedings of the 22th International Conference on Port and Ocean Engineering under Arctic Conditions, POAC*, The International Society of Offshore and Polar Engineers, Espoo, Finland, June 2013.

Maus S, Schneebeli M and Wiegmann A (2021) An X-ray micro-tomographic study of the pore space, permeability and percolation threshold of young sea ice. *The Cryosphere* **15**(8), 4047–4072. doi:10.5194/tc-15-4047-2021

Nakawo M (1983) Measurements on air porosity of sea ice. *Annals of Glaciology* **4**, 204–208. doi:10.3189/s0260305500005486

Nakawo M and Sinha NK (1981) Growth rate and salinity profile of first-year sea ice in the High Arctic. *Journal of Glaciology* **27**(96), 313–328. doi:10.3189/s0022143000015409

Obbard RW, Troderman G and Baker I (2009) Imaging brine and air inclusions in sea ice using micro-X-ray computed tomography. *Developments in Geotectonics* **55**(194), 113–115. doi:10.3189/002214309790794814

Oggier M, Eicken H, Wilkinson JP, Petrich C and O'Sadnick M (2019) Crude oil migration in sea-ice: laboratory studies of constraints on oil mobilization and seasonal evolution. *Cold Regions Science and Technology* **174**, 102924. doi:10.1016/j.coldregions.2019.102924

Otsu N (1979) Threshold selection method from gray-level histograms. *IEEE Trans Systems Man and Cybernetics* **9**(1), 62–66. doi:10.1109/tsmc.1979.4310076

Perovich DK and Gow AJ (1996) A quantitative description of sea ice inclusions. *Journal of Geophysical Research: Oceans* **101**(C8), 18327–18343. doi:10.1029/96JC01688

Peters GP, Nilssen TB, Lindholt L, Eide MS, Glomsrød S and 2 others (2011) Future emissions from shipping and petroleum activities in the Arctic. *Atmospheric Chemistry and Physics* **11**(11), 5305–5320. doi:10.5194/acp-11-5305-2011

Petrich C, Karlsson J and Eicken H (2013) Porosity of growing sea ice and potential for oil entrainment. *Cold Regions Science and Technology* **87**, 27–32. doi:10.1016/j.coldregions.2012.12.002

Petrich C, O'Sadnick M, Brekke C, Myrnes M, Maus S and 10 others (2019) MOSIDEO/CIRFA tank experiments on behavior and detection of oil in ice. *25th International Conference on Port and Ocean Engineering under Arctic Conditions (POAC)*, The International Society of Offshore and Polar Engineers, Delft.

Pringle DJ, Miner JE, Eicken H and Golden KM (2009) Pore space percolation in sea ice single crystals. *Journal of Geophysical Research: Oceans* **114**(12), 1–14. doi:10.1029/2008JC005145

Pustogvar A and Kulyakhtin A (2016) Sea ice density measurements. Methods and uncertainties. *Cold Regions Science and Technology* **131**, 46–52. doi:10.1016/j.coldregions.2016.09.001

Salomon ML, Arntsen M, Phuong ND, Maus S, O'Sadnick M and 3 others (2017) Experimental and micro-CT study on the oil distribution in laboratory grown sea ice. *Proceedings of the International Conference on Port and Ocean Engineering under Arctic Conditions, POAC.* [Technical University of Norway].

Schwarz J and Weeks WF (1977) Engineering properties of sea ice. *Journal of Glaciology* **19**(81), 499–531. doi:10.3189/s0022143000029476

Shokr M and Sinha N (2015) *Sea Ice: Physics and Remote Sensing*. Hoboken, New Jersey: John Wiley and Sons. ISBN 978-1-119-02789-8.

Sinha N (1977) Technique for studying structure of sea ice. *Journal of Glaciology* **18**(79), 315–324. doi:10.3189/s0022143000021390

Weeks WF (2010) *On Sea Ice – Willy Weeks – Google Bøker*. Fairbanks: University of Alaska Press, ISBN 978-1-60223-079-8.

Weissenberger J, Dieckmann G, Gradinger R and Spindler M (1992) Sea ice: a cast technique to examine and analyze brine pockets and channel structure. *Limnology and Oceanography* **37**(1), 179–183. doi:10.4319/lo.1992.37.1.0179

Zack GW, Rogers WE and Latt SA (1977) Automatic measurement of sister chromatid exchange frequency. *Journal of Histochemistry and Cytochemistry* **25**(7), 741–753. doi:10.1177/25.7.70454

Appendix A

Table of variables

β	exponent related to the percolation theory
c	gives the phase relation between brine and solid salt
C	constant
CPN	number of closed pores per volume
F_{SS}	Factor to calculate the solid salt fraction from brine vol.
$f(T, T_{\mathrm{CT}})$	factor to convert brine fraction from T_{CT} to T
M_{air}	mass in air
M_{par}	mass in paraffin
OPN	total number of open pores per area
ϕ_{air}	air porosity
ϕ'_{air}	air porosity (CT-image derived in situ porosity)
ϕ_{aircal}	calculated air porosity based on hydrostatic density
$\phi_{\mathrm{airopen}z+}$	open air porosity to upper sample surface (CT)
$\phi_{\mathrm{airopen}z-}$	open air porosity to lower sample surface (CT)
$\phi_{airopenz+-}$	open air porosity to lower and upper sample surface (CT)
ϕ^{CT}_{air}	air porosity (CT)
$\phi^{CT}_{\mathrm{airclosed}}$	closed air porosity (CT)
$\phi^{CT}_{\mathrm{aircon}}$	vertically connected air porosity (CT)
$\phi^{CT}_{\mathrm{airopen}}$	open air porosity (CT)
ϕ_{b}	brine porosity
ϕ_{bclosed}	closed brine porosity
ϕ_{bcon}	vertically connected brine porosity
ϕ_{bcrit}	threshold porosity
ϕ_{bopen}	open brine porosity
ϕ'_{b}	brine porosity (CT derived in situ porosity)
ϕ'_{bclosed}	closed brine porosity (CT derived in situ porosity)
ϕ'_{bcon}	connected brine porosity (CT derived in situ porosity)
ϕ'_{bopen}	open brine porosity (CT derived in situ porosity)
ϕ_{brinecal}	calculated brine porosity based on conductivity
$\phi^{\mathrm{CT}}_{\mathrm{brine}}$	brine porosity and solid salt (CT)
ϕ_{con}	connected porosity
ϕ_{z+}	open porosity to the upper sample surface
ϕ_{z-}	open porosity to the lower sample surface
ϕ_{z+-}	open porosity to the upper and lower sample surface
ρ	sea-ice bulk density
ρ_{air}	air density
ρ_{b}	brine density
ρ_{CT}	bulk density from CT parameters at − 15°C
ρ_{hydro}	bulk density based on hydrostatic measurements
ρ_{ice}	ice density
ρ_{par}	paraffin density
ρ_{ss}	solid salt density
S_{b}	brine salinity
S_{bdrip}	dripped brine salinity
S_{bcent}	centrifuged brine salinity
S_{cent}	bulk salinity after centrifuging based on conductivity
S_{con}	bulk salinity based on conductivity
S_{CT}	bulk salinity based on CT
S_{ice}	sea-ice bulk salinity
S_{rest}	bulk salinity of cut-off
T_{cent}	centrifuge temperature
T_{CT}	CT temperature
T	in situ Temperature

Appendix B

Illustration of granolometry and porosimetry

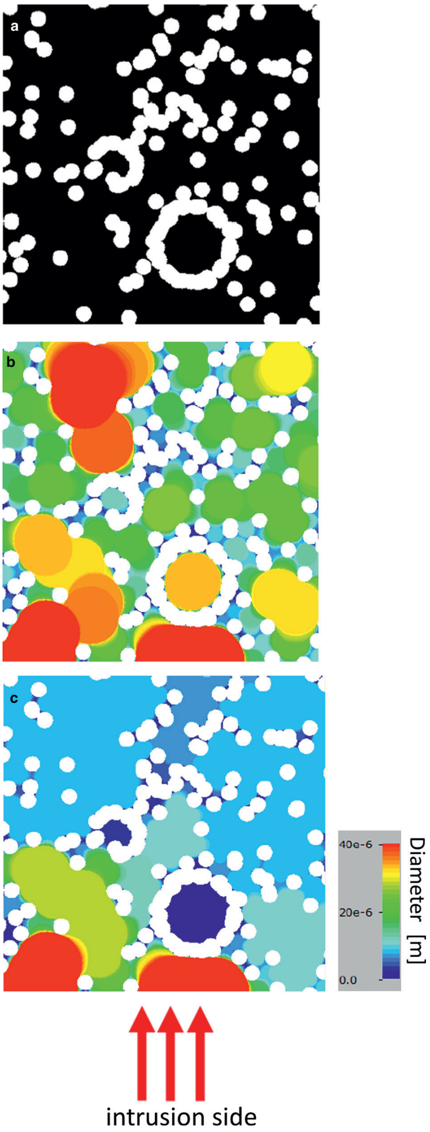

Fig. 18. (a) Shows a structure with the solid material in white and the pore space in black. (b) Granulometry: shows the same structure with coloured pore volume, where the red volume describes the pore diameters around 40 μm and larger, green areas represent diameters around 20 μm and the blue-coloured area below 15 μm. (c) Porosimetry: structure shown in (a) gets penetrated with a non-wetting fluid, indicated by the red arrows. Pores found by porosimetry must be connected to the non-wetting phase. (after Linden and others, 2018).

Appendix C

Illustration of vertical CT- reconstruction: Core 2-2 from 30 March

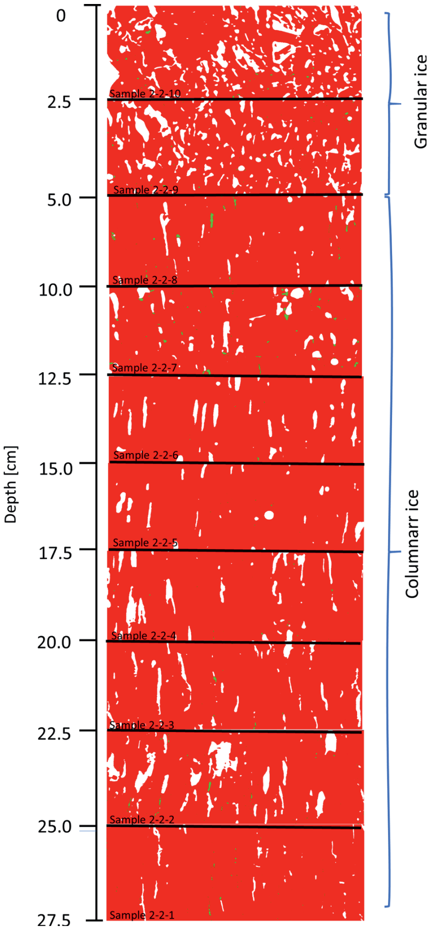

Fig. 19. Vertical CT-reconstructions, showing ice in red, brine in green and air in white. Elongated, vertical oriented air inclusions (centrifuged brine) from sample 2-2-9 and downwards indicate granular sea ice. Sample 2-2-10 and 2-2-9 show a random pattern of air inclusions and are therefore interpreted as granular sea ice.

Paper II

Quantitative analysis of oil and diesel distribution within sea ice pore space by micro-CT analysis

This paper is awaiting publication and is not included

Paper III

Experimental and micro-CT study on the oil distribution in laboratory grown sea ice

POAC'17
Busan, KOREA

Proceedings of the 24th International Conference on
Port and Ocean Engineering under Arctic Conditions
June 11-16, 2017, Busan, Korea

Experimental and Micro-CT study on the Oil Distribution in laboratory grown Sea Ice

Martina Lan Salomon[1], Martin Arntsen[2], Nga Dang Phuong[2], Sönke Maus[1], Megan O' Sadnick[2], Chris Petrich[2], Martin Schneebeli[3], Mareike Wiese[3]

[1] Norwegian University of Science and Technology, Trondheim (NTNU), Norway
[2] Northern Research Institute Narvik (NORUT), Narvik, Norway
[3] WSL Swiss Federal Institute for Snow and Avalanche Research SLF, Davos, Switzerland

ABSTRACT

Increasing activities in Arctic waters bare a risk of oil spills under ice-covered conditions and afford sound understanding of the interplay between sea ice and oil. Towards better knowledge, this study focuses on X-ray- micro computed-tomography (µ-CT) investigations of a laboratory oil- in ice experiment. The 3-dimensional distribution of oil in the porous space of 11- 13 cm columnar ice grown in a laboratory was investigated. Two different oil content measurement methods are discussed. (i) The first method quantifies the oil volume fraction based on µ -CT-scan investigations, allowing spatial oil distribution analysis in the porous space of sea ice. Oil inclusions were mapped manually over the acquired CT-scans with a resolution of 18 µm and 25 µm, respectively. Results give higher oil contents for smaller resolutions. Oil migration of 4 cm was observed. (ii) The second method quantifies the present oil concentration with fluorescent measurements. CT- scans give in comparison to fluorescent measurements a root mean square error of 1.27 % (18 µm) 0.76 % (25 µm), respectively. Bulk salinity determined from melted samples is compared with salinity estimated from µ –CT data.

KEY WORDS: Sea ice, Computer Tomography, Microstructure, Oil, Porosity

INTRODUCTION

Activities in polar marine areas are increasing. Including interest in Arctic resources. Oil exploration in potentially ice-covered regions and growing shipping activities in high latitudes, bare a risk of accidental oil spills. Giving objective to study the interaction of sea ice and oil for environmental and sustainable risk management.

Networks of brine channels and air inclusions make sea ice to a permeable material and a potential entrapment medium for oil. Investigations on the interaction of oil and sea ice have been published since the 1970's (Glaeser & Vance, 1971; NORCOR, 1975). Several field studies and experimental work were conducted since then. Studies were mainly based on destructive two- dimensional observations of thin sections and macroscopic descriptions, characterizing processes from oil encapsulation over oil migration to oil surfacing on sea ice (c.f Martin, 1979; Nelson, 1981; Buist & Pistruzak, 1981; Buist et al., 1983; Otsuka et al. 2004; Karlsson, 2009; Karlsson et al., 2011). Experiments quantifying the oil content in sea ice were conducted by Karlsson et al., (2011) and Otsuka (2004), reporting that the ability of oil to penetrate sea ice is limited by its porosity. A porosity threshold of 0.1 to 0.15 was determined and an oil saturation up to 4.5 to 7 mass percent oil by mass of sea ice was reported. Based on these observations and model assumptions (Petrich, Karlsson, & Eicken, 2013)) computed the potential oil penetration depth and concluded on oil entrainment volumes from less than 1 L/ m^2 as high as 5 to 10 L/ m^2 with increasing ice temperatures. 3-dimensional insights and application of X-ray tomography (XRT) to sea ice samples were first given by Kawamura (1988) with a resolution of 1 mm. Maus, 2009, 2013, 2015 applied XRT and synchrotron- XRT on sea ice with a resolution of 18 to 25 µm, respectively a resolution of 2 x 5.6 µm. Based on 3- dimensional micro- CT data, oil infiltration rate was computed, concluding on entrainment volume not solely depending on porosity. Furthermore, the control mechanism are described by parameters such as, pore size, pore necking and convection driven desalinization. (Maus et al., 2013) Salomon et al. (2016) give preliminary results on the detection of oil in sea ice based on synchrotron- XRT.

The present experiment was designed to detect the 3-dimensional distribution and the concentration of oil in the porous space of sea ice based on µ -CT investigation. Oil concentration measurements were achieved with two different approaches. (i) First method is based on µ-CT-scans and mapping the oil content over the 2- dimensional µ-CT sections. (ii) Second approach focused on UV-light stimulation and emitted fluorescence measurements of hydrocarbons. Resulted brine volume fraction from µ-CT-scans were converted into bulk salinity and are compared with measured bulk salinity.

METHODS

Experimental Setup

Ice growth was performed in a cold lab at NORUT Narvik in slightly conical double-walled plexiglas container with outer-dimensions of 51 x 51 x 51 cm and inner-dimensions of 50 x 50 x 50 cm. Approximately 100 liter of artificial saltwater (Blue Treasure Synthetic Salt) with an initial salinity of 31.5 ppt was filled into the tank. The plexiglas tank allowed visual access to the freezing process and facilitated the oil injection. The double-tank arrangement, surrounded by a 5 cm thick Styrofoam- isolation and air-cooling allowed one-dimensional ice growth. Heat supply from the bottom of the tank avoided supercooling of the water column and led to columnar ice growth. Fans beneath the tank assured homogenous heat distribution.

Prior to ice growth initiation, artificial seawater had a water temperature of approximately 0 °C. Referred starting point of the experiment is the set of ambient temperature to –15 °C. After 64 hour ice reached a thickness of 8 cm and oil was injected below the ice with a silicon syringe of 5 mm diameter. 28 h hours after oil release, room temperature was raised to -10 °C, to facilitate oil migration, to ensure that the surface temperature well above the nominal pour point of crude oil at -15 °C. Sampling commenced 91.5 hours after experimental start when the ice thickness reached 11-13 cm. Cores were taken with a drill 50 mm in diameter. Samples were stored over night at -80 °C and than transported on dry ice (-78.5 °C) from NORUT Narvik (Norway) to NTNU Trondheim (Norway). After storage at - 50 °C over a period of 9.5 months they were prepared for imaging with X-ray- micro computed-tomography (µ-CT). The cores were cut into subsamples of 2 to 3.5 cm thickness and a diameter of 35 mm. During the cutting process it was attempted to preserve the oil lenses.

During transport from and to WSL Swiss Federal Institute for Snow and Avalanche Research SLF (Davos,Switzerland), where the first µ-CT measurements were performed at -15 °C, sample temperature was kept at the same temperature by eutectic cooling elements. Back to NTNU samples were stored for another 2 months at -50 °C. Imaging of the same samples was conducted at the RECX, Norwegian Centre for X-Ray diffraction, scattering and imaging at the Norwegian University of Science and Technology (NTNU, Trondheim, Norway). Before imaging was performed samples were warmed up to the imaging temperature of -15 °C over night. Prior to fluorescent measurements sample were molten in airtight glass containers and shipped to NORUT Narvik.

X-ray micro computed- tomography (μ-CT) imaging

μ-CT measurements were conducted with three instruments (i) ScancoMedical AG micro-CT 40 at SLF, (ii) SacancoMedical AG micro-CT 80 at SLF and (iii) XT H 225 ST micro-CT system from Nikon Metrology NV at NTNU. (i & ii) were operated with a micro focus X-ray source (7 μm diameter) current of 177 μA and an acceleration voltage of 45 kV. Detector panels of 2048 x 256 and 2048 x 128 pixels, respectively were used. Tomographic scans were performed in high resolution mode with 2000 rotation per 360°. The height of scans could be chosen according to the sample height. Scans were operated with a field of view (FOV) of 37 mm, resulting in a pixel size of 18 μm. Samples were acquired in a cold- room at ambient temperatures of -15 °C at SLF. Acquisition time at SLF was limited to a window of 5 days, therefore two CTs were used simultaneously. Settings were the same and a difference at the acquisition is not assumed. (iii) a current source of 250 μA and an acceleration voltage of 150 kV. Scans were performed with 3142 rotation per 360°. A Perkin Elmer 1620 with a pixel size of 200 x 200 μm and 2048 x 2018 pixels operated as flat panel detector. The FOV of 50 mm corresponds to a pixel size of 25 μm. Scanning temperature (-15 °C) was controlled with a thermoelectric assembly (www.lairdtech.com) by top and bottom sample cooling.

CT- data provide a 2-d map of the variation of X-ray absorption of substructures within the imaged sea ice. Those 2-d maps are called radiographs and are acquired over a finite number of radiographic viewing directions to reconstruct the distribution of X-ray absorptivity within a horizontal cross-section of the imaged sample. The cross sections are stored as 16-bit grey value stacks and give a 3- dimensional view of the scanned object.The resulting 3-d images of ice cores were processed in ImageJ (rsb.info.nih.gov/ij). First a rectangular cylinder with the largest possible horizontal cross-section was cropped. After cropping a 2 pixel median and 1.5 standard deviation Gaussian blur filter were applied. Segmentation of air and ice was based on using Otsu's algorithm (Otsu, 1979; Maus, 2015) For segmentation of brine from ice the Triangle algorithm was applied (Zack et al., 1977). A different segmentation method was chosen for setting the brine threshold, as the Otsu algorithm was found to give too high brine volumes (Hullar et al., 2016).

Absorption contrast between ice and oil was insufficient for automatic segmentation. Segmentation was performed manually using the Wand Tool in ImageJ. Oil inclusions were selected by tracing objects. Therefore an initial pixel (iP) value was chosen for each oil bubble in the acquired 2-D slices. The Wand Tool checked the 4 neighbouring pixels of the iP. If the adjoining pixel was within the tolerance range of 3-5 of the iP value, it was detected as oil and its neighbouring pixels were checked in the same manner. If one pixel did not fulfil the criterion of falling into the range of the iP value, it was not accounted longer for oil and a border was set. Manual selection of oil was repeated on every 5th to 20th slice of an image stack. The selected areas were interpolated between the 2-D slices with the Region of Interest (ROI) manager and edited with the Segmentation Editor (Schindelin et al., 2012) giving a 3-D view of the oil inclusion. Segmentation results in 3-d images, where any voxel is either air, ice, oil or brine. The respective volume fraction were computed by GeoDict(2017).

The brine volume fraction Vb_{CT} was used to estimate the bulk sea ice salinity S_{CT} from

$$S_{CT} = \frac{S_b * \rho_b * Vb_{CT}}{\rho_i} \qquad (1)$$

where S_b is the brine salinity at imaging temperature, ρb is the brine density at imaging temperature and ρi is the bulk sea ice density. *Sb* 177.96 ppt was interpolated from the table given by Cox and Weeks (1983), ρb was taken as *1000+0.8Sb* and bulk sea ice density ρi [kgm^{-3}] was computed from CT- data, knowing the analyzed volume as well as the ice, air, oil and brine fractions. For pure ice the density of 920 kgm^{-3} was assumed.

Oil density was estimated as 877 kgm^{-3} from measured Crude oil Troll B density of 0.879 Mgm^{-3} at a temperature of 20 °C, assuming a linear increase of oil density with 0.01 Mgm^{-3}/15 °C. The oil volume fraction Vo_{CT} was converted to oil mass fractions by multiplication with $\rho oil/\rho i$.

Salinity and oil content of melted samples

Bulk salinity *S* of melted samples is based on electric conductivity measurements. Conversion from conductivity to ppt were conducted with the Gibbs Sea Water (GSW) Oceanographic Toolbox of TEOS- 10 (Dougall et al. 2011).

The mass fraction $Mo_{Fluroescent}$ oil in the melted samples was extracted with heptane by adding an equal volume of heptane to oil-containing samples. The concentration of oil in the heptane was subsequently analysed using a UV-fluorescence meter TD500^{TM} (Turner Designs Hydrocarbon Instruments, Inc). Under UV or near UV light, aromatic hydrocarbons in the oil are stimulated or excited to fluoresce. The intensity of fluorescent emission reflects the concentration of aromatic hydrocarbons in the oil. Since the UV-fluorescence meter was calibrated with the same crude oil, the intensity of fluorescent emission corresponds to the concentration of the oil (Brost et al., 2011).

RESULTS

In our laboratory experiment columnar sea ice grew over the course of 91.5 hours to a thickness of 11-13 cm at an air temperature of -15 °C. 63.75 hour after the experiment start, ice thickness reached 8 cm and oil was released. Four lenses of Troll B crude oil were injected under the ice, each with a volume of 20-25 ml and a thickness of approximately 4 mm. Injected oil migrated along the ice-water interface before it collected at the highest points of small under-ice undulations.[1] Within 4 hours, a thin rim of horizontal platelets formed around the oil lenses. After 5.5 hours, a thin layer of ice platelets had formed beneath all four oil lenses. Ice cores were taken was taken when the ice layer underneath the oil lenses was 2-3 cm and an overall thickness of 11- 13 cm. Table 1 summarizes the analysis of cores taken as described in the method section and presented in the following figures.

---

[1] Phenomena of oil collecting in concave under- ice cavities and encapsulation process are for e.g. described by Glaeser & Vance (1971), NORCOR (1975), Goodman and Fingas (1983) Buist et al. (1983) and Wilkinson et al. (2007).

Air fraction

CT- based results for total and closed air volume are given for both acquisitions at SLF and at NTNU and are compared with each other in Figure 1. Open porosity is defined by a continuous path from the pore to one of the surface edges in x-, y-, or z- direction, whereas closed pores are not connected to any surface.

Total and closed air volume fraction Va_{SLF} and Va_{NTNU} are plotted in % over the ice thickness [cm] for cores C,D,E and F each with a length of 13, 12,11 and 12 cm. Air porosity for sample C4 is not shown in Figure 1 as $\mathrm{Va}_{\mathrm{SLF}}$ and $\mathrm{Va}_{\mathrm{NTNU}}$ the sample broke during transport. Therefore different areas were analysed resulting in a significant variance for $\mathrm{Va}_{\mathrm{SLF}}$ and $\mathrm{Va}_{\mathrm{NTNU.}}$ Results from Closed air porosities in NTNU-acquisition excluding samples with oil lenses tend to be with a mean of 0.60% and a standard deviation of 0.23% higher than results from SLF with a mean of 0.52% and a standard deviation of 0.16%.

Brine fraction and salinity

Comparison of estimated bulk salinity S_{SLF} and S_{NTNU} determined from Vb_{SLF} and Vb_{NTNU} with measured bulk salinity S are shown for each core over the ice thickness in Figure 2. Salinity profiles show a characteristic C-Shape profile (Eicken, 1992). All salinity derived from µ-CT measurements is compared with direct measurements in Figure 4(a). Salinity calculation for S_{SLF} differs from direct measurements with a root mean square deviation of 1.64 %. S_{NTNU} differs from measurements with a root mean square error of 2.10 % from measured salinity.

Oil fraction

Oil content for samples imaged at the SLF and NTNU are expressed in oil mass fraction [%] to be comparable with fluorescent measurements (Figure 3 & 4). Oil injection level is highlighted in the plots at an ice thickness of 8 cm. Measurements displayed with a black circle, correspond to highlighted results in Table 1. The highest oil volume was found in sections close to the injection levels, i.e. at and near the location of the oil lenses. Results of oil content Mo_{SLF} and Mo_{NTNU} are compared with fluorescent oil content measurements in Figure 4. Differences between Mo_{NTNU} and $Mo_{Fluorescenct}$ are given by a root mean square deviation of 0.76%. Mo_{SLF} deviates from fluorescent measurements $Mo_{Fluorescence}$ with a root mean square error of 1.27%. While µ -CT measurements seem to be biased slightly high or low, agreement with fluorescent measurements is very good. With the notable exception of C4 acquired with a resolution of 18 µm. Oil and ice absorption contrast was too low in the mentioned sample for visual detection.

Table 1: Summary of key parameters and experiment results.

Sample	Sample Depth from air-ice interface	Air Volume Fraction (SLF) Va_{SLF}		Air Volume Fraction (NTNU) Va_{NTNU}		Brine Volume Fraction (SLF) Vb_{SLF}		Brine Volume Fraction (NTNU) Vb_{NTNU}		Bulk Salinity S_{SLF} from Vb_{SLF}	Bulk Salinity S_{NTNU} from Vb_{NTNU}	Bulk Salinity S	Oil Mass Fraction (SLF) Mo_{SLF}	Oil Mass Fraction (NTNU) Mo_{NTNU}	Oil Mass Fraction (Fluorescent) $Mo_{Fluorescent}$
-	cm	%		%		%		%		ppt	ppt	ppt	%	%	%
-	-	total	closed	total	closed	total	closed	total	closed			-	-	-	-
C1	0-2.5	-	-	3.42	0.99	-	-	4.94	3.69	-	10.9	6.8	-	0.00	-
C2	2.5-3.5	-	-	0.57	0.51	-	-	3.34	2.34	-	7.4	5.1	-	0.00	-
C3	3.5-6	0.89	0.61	0.95	0.58	2.61	2.30	2.18	1.97	5.8	4.8	6.4	0.44	0.47	0.57
C4	6-8.5	26.45	0.19	0.65	0.12	2.54	1.99	4.09	2.27	5.6	9.0	5.3	0.98	0.00	1.19
D1	0-2.5	-	-	0.79	0.71	-	-	3.54	2.5	-	7.8	6.7	-	0.00	-
D2	2.5-5	0.63	0.48	0.60	0.50	3.66	2.77	3.04	2.44	8.6	6.7	6.4	0.008	0.01	0.02
D3	5-7.5	1.76	0.85	4.54	3.75	3.49	2.99	1.94	1.63	7.7	4.3	5.9	10.09	8.61	6.74
D4	7.5-11	-	-	0.48	0.44	-	-	4.72	4.22	-	10.4	9.1	-	0.00	0.56
E1	0-2.5	-	-	1.26	0.95	-	-	3.47	2.71	-	7.7	6.8	-	0.00	
E2	5-7.5	0.61	0.52	0.66	0.58	4.01	3.30	2.85	0.62	8.9	6.7	5.8	0.09	0.04	0.12
E3	7.5-10	0.97	0.67	1.04	0.55	3.10	2.75	1.61	1.53	6.9	3.6	5.3	1.39	0.72	0.73
E4	10-11.5	5.81	0.78	-	-	2.35	1.98	-	-	5.2	-	6.9	4.77	-	3.09
F1	0-2.5	-	-	6.38	0.78	-	-	2.79	2.07	-	6.2	7.1	-	0.00	-
F2	2.5-5	0.86	0.66	0.84	0.72	2.85	2.33	1.36	1.23	6.3	3.0	5.5	0.12	0.02	0.10
F3	5-8	4.47	1.05	3.60	3.52	2..40	2.18	1.85	1.54	5.3	4.2	4.5	6.88	5.07	-
F4	8-10	-	-	0.59	0.36	-	-	4.69	3.26	-	10.4	7.1	0.00	0.00	-
Temperature [°C]						Brine Density ρb [Mgm^{-3}]					Brine Salinity Sb [ppt]			Oil Density [Mgm^{-3}]	
-15						1.14236					177.95			0.877	

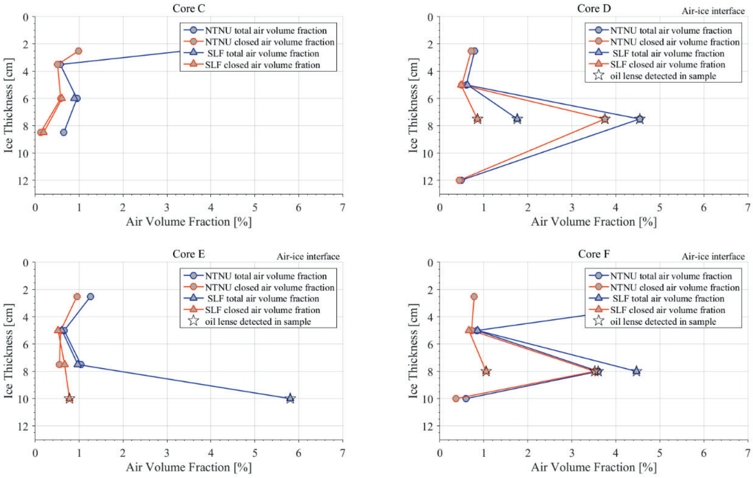

Figure 1: Closed and total air volume fraction from μ-CT- scans at SLF and NTNU in comparison.

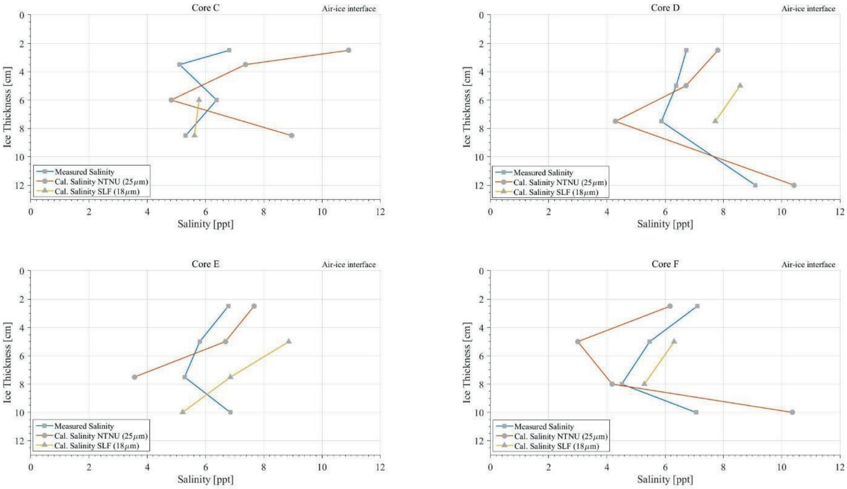

Figure 2: Measured bulk ice salinity in comparison with approximated bulk salinity based on segmented brine volume fractions of SLF-scans and NTNU-scans.

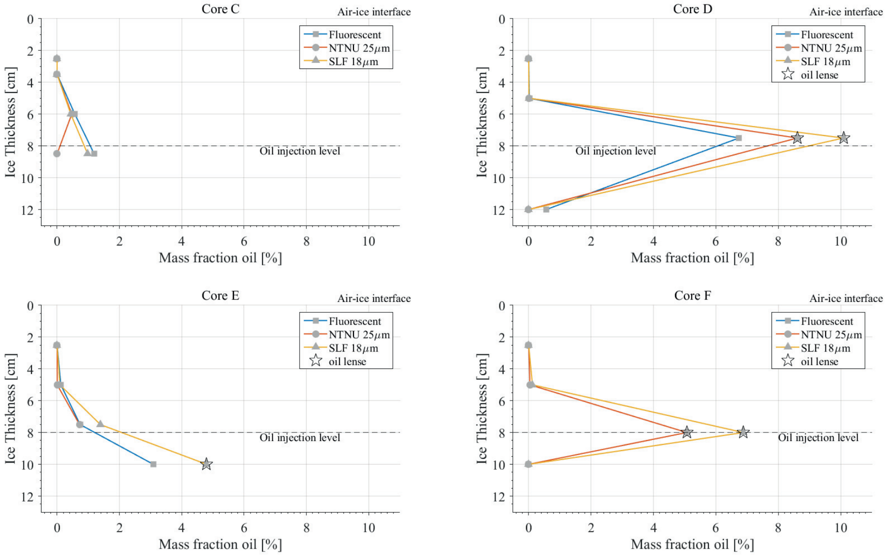

Figure 3: Oil content expressed in mass fraction in comparison between fluorescent measurement, µ-CT images from SLF and NTNU. Results highlighted with a black circle are averaged over the whole volume.

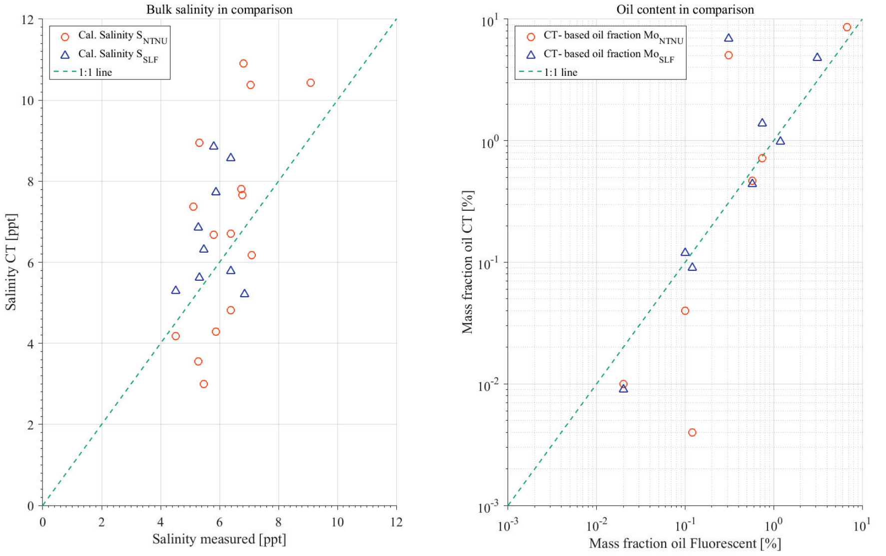

Figure 4: Bulk salinity of three different sources CT-scans (NTNU), CT-scans (SLF) and measured in comparison; Oil content from CT-scans (NTNU), CT-scans (SLF) and fluorescent in comparison.

DISCUSSION

Air fraction

Air segmentation with Otsu algorithm gives reasonable and consistent results for SLF and NTNU scans in comparison (Fig. 1). Total porosity is influenced by the open porosity, which might result from brine drainage. Values for closed porosity are there for more reliable. Spikes in air volume fraction are observed for samples containing oil concentrated in lenses (Figure 1), with one exception for sample F1. Sample F1 shows higher air content in the top most part. Observed air volume are open pores, indicating that potentially brine was leaking during sampling, storage and transportation.

We noticed larger air volumes above all oil lenses. Samples F3 and D3 where sectioned in a way, that preserved the closed air volume forming channels above the oil lens (Figure 6). Air volumes of 73.6 and 226.3 mm^3, respectively were found. Additionally smaller air bubbles were detected within the lenses of oil with a volume of 1 to 3 mm^3. However, we cannot be sure whether these are real due to air content of the oil or resulting from thermal cycling.

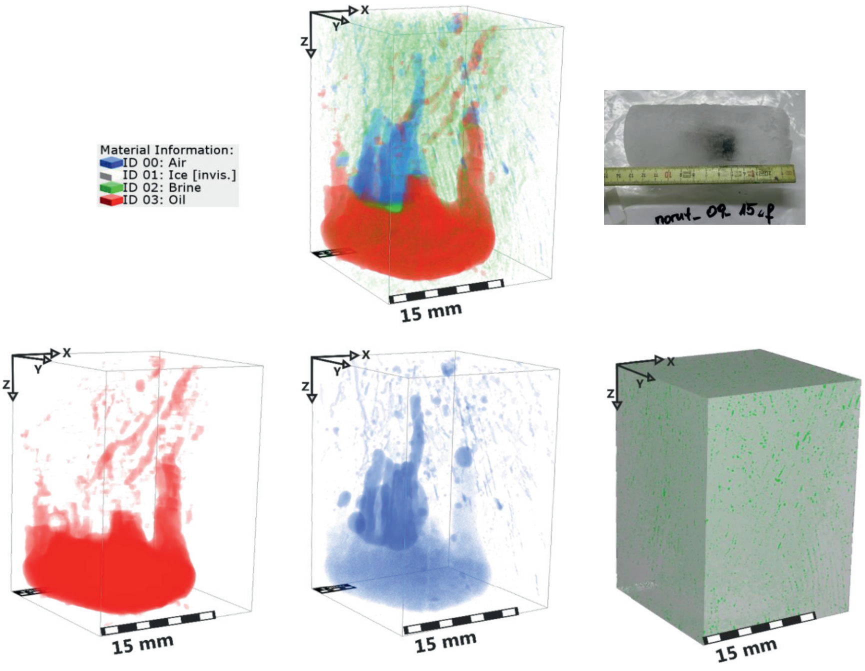

Figure 5: 3-D image of segmented oil (red) air (blue) and brine (green) for sample F3 resulting from μ-CT at SLF. Ice is invisible, except of the last image where ice is shown in white.

Too high closed air porosities in sample F3 and D3 from images at NTNU are observed in comparison to SLF data. Short thermal cycles above –15 °C might have occurred during scanning at SLF. As the temperature in the CT was controlled over the room temperature in the cold lab. Exposure to temperatures above the crude oil pour point (-15 °C) might lead to oil migration and drainage within the sample. Consequently the initial oil filled space is replaced by air. By cooling the sample afterwards down to the transport temperature, refreezing processes start and leave a closed pore.

While the source of these volumes could not been established unambiguously candidates include:

a. Unintended air release during first oil injection.
b. Air collected by the oil droplets migrating beneath the ice prior to freeze-in leading to an estimated air volume of 300 mm^3, for a prior freeze migration length of 10 mm by an oil lens diameter of 20 mm;
c. fluid loss during repeated warming and cooling cycles.

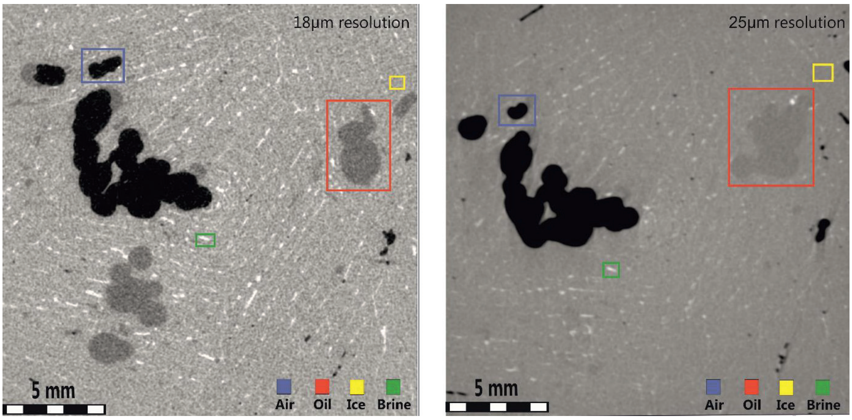

Figure 6: 2-D sections 18 µm respectively 25 µm resolution. Showing typical grey values for air, oil, ice and brine.

Brine fraction and salinity

CT- based salinity evaluation results in comparison to measured salinity in an error of approximately 2% (Fig. 4). Where S_{SLF} shows a slightly higher salinity than S_{NTNU}. Error can possibly result from different:

(a) chosen energy setting for SLF and NTNU acquisition. Higher energy resolve the ice to brine contrast better, resulting in higher evaluated salinity. Furthermore, plastic sample holder (SLF) with a lower X-ray absorption in comparison to aluminum holder (NTNU) were chosen, having a possible effect on the results. Systematically evaluation on a bigger data set is needed to determine influences.

(b) pixel size of 25 µm and 18 µm results in resolving objects ≥ 50 µm and 36 µm respectively, i.e. 2x pixel size. This assumption would lead to an higher estimated salinity for smaller pixel sizes. Relevance of resolution for brine volume segmentation is not certain.

(c) imaging temperature was chosen to be -15°C for both acquisitions, the actual temperature in the CT at the SLF, was controlled over the room temperature and might therfore be slightly different.

Oil fraction

Manual oil segmentation is time consuming and subjective. Figure 5 shows the air, brine, and oil distribution in sample F3 acquired at the SLF. In general, most oil was found a few mm underneath and above the respective oil injection level. Above the oil lenses, oil was found in channels with a similar orientation to the brine layer direction and as individual, tiny oil pockets. Oil was detected in inclusions as small as 0-36 µm in images acquired at SLF. Whereas observation of acquisition NTNU show that the smallest oil inclusions was found in pockets with a diameter in between 0- 50 µm, which is actually 2x the pixel size. Largest inclusion was found in a pore with 19 mm in diameter. Oil migration was observed up 2.5 to 5 cm above the respective lenses. Where oil was detected in the lower third up to 2/3 of the sample, approximately to a level 4 cm from the air- ice interface. I.e., within 46 hours oil migrated approximately 4 cm upwards from the oil injection level.

Oil content in CT- data in comparison with fluorescence measurements tend to be higher for samples with oil lenses and underestimated for samples with smaller oil inclusions.Inclusions were classified as oil only if they appeared over more than one slice. More objective results could be expected from automated segmentation. However, this was not possible in the current experiments since the oil and ice absorption contrast was too low. Enhancement of the oil-ice contrast could be achieved by doping the oil, e.g. with iodoheptane (Brown et al., 2014).

The oil content compared in Figure 3 shows that trends were consistent. However, Vo_{SLF} tends to be higher than Vo_{NTNU}. Observed trend can be explained by several factors:

a. due to subjective manual segmentation and the tendency to discard doubtful oil signals, just appearing in a single slice
b. Lower resolution data do show a coarser vertical grid, smaller inclusions were therefore easier excluded and accounted for ice;
c. choice of energy during CT-acquisition show a significant effect on the oil detectability (Fig.6), lower energies used for acquisition at 18 µm result in a higher absorption contrast between oil and ice, and are easier to detect.
d. oil loss and drainage during transport and acquisition at SLF.

CONCLUSIONS

µ-CT is a powerful instrument to obtain non-destructive 3-dimensional insights into the interior of sea ice. The employed laboratory CTs provide satisfying results on low absorption contrast materials such as sea ice and oil (Figure 6) and reveal their spatial distribution (Figure 4).

Automated segmentation for air with the Otsu gave reasonable results for oil free samples with small bias in vertical profiles. Comparison of salinity evaluated from CT-data with measured salinity show a slight overestimation of brine volume fractions.

Spatial distribution of oil can be studied with significant investment of time into manual segmentation. Oil was found in inclusions with a diameter as small as 0- 36 µm, i.e actually 2 times pixel size. Comparisson of oil content from µ-CT with fluorescent measurements show consistent trends.Future motivation is given by the improvements in segmentation to open the possibility for quantitative oil and ice studies.

ACKNOWLEDGEMENTS

We gratefully acknowledge Matthias Jaggi for assistance and expertise at WSL Swiss Federal Institute for Snow and Avalanche Research SLF, as well as Ole Tore Buset and Leander Michels for guidance and help during µ-CT measurements at the Norwegian University of Science and Technology (NTNU). Special thanks to Math2Market, GeoDict for providing us with the imaging analysis software. Much appreciation to Statoil for providing Troll B crude oil. This work was supported by the Research Council of Norway PETROMAKS2 program, project number 243812 (MOSIDEO).

REFERENCES

Buist, I. A., Potter, S., & Dickins, D. (1983). Fate and Behaviour of Water-in-Oil Emulsion in Ice. *Proceedings of the 6th Annual AMOP Technical Seminar, 263-279.*

Brost, D. F., Foster, A. E., Holmes, M., Designs, T., & Instruments, H. (2011). No-Solvent Oil-in-Water Analysis – A Robust Alternative to Conventional Solvent Extraction Methods. *Offshore Technology Conference*, (January 2011), 1–18. http://doi.org/10.4043/21695-MS

Brown, K., Schlüter, S., Sheppard, A., & Wildenschild, D. (2014). On the challenges of measuring interfacial characteristics of three-phase fluid flow with x-ray microtomography. *Journal of Microscopy*, *253*(3), 171–182.

Buist, I. A., & Pistruzak, W. M. (1981). Dome Petroleum's Oil and Gas Undersea Ice Study. In *Proceedings of the Arctic Marine OIl Spill Programm Technichal Seminar, Edonton, Alberta*.

Cox, G. F. N., & Weeks, W. F. (1983). Equations for determining the gas and brine volumes in sea - ice samples. *Journal of Glciology*, *29*(102), 306–316.

Eicken, H. (1992). Salinity Profiles of Antarctic Sea Ice : Field Data and Model Results. *Journal of Geophysical Research,* 97(C10), 15545-15557

Glaeser, J. L., & Vance, G. P. (1971). *A Study of Behaviour of Oil Spills in the Arctic*.

Hullar, T., & Anastasio, C. (2016). Direct visualization of solute locations in laboratory ice samples. *The Cryosphere*, 10(5), 2057-2068

Karlsson, J. (2009). Oil Movment in Sea Ice, A laboratory study of fixation , release rates and small scale movement of oil in. *University of Copenhagen, Copenhagen,Denmark.*

Karlsson, J., Petrich, C., & Eicken, H. (2011). OIL ENTRAINMENT AND MIGRATION IN LABORATORY- GROWN SALTWATER ICE. In *Proceedings of the 21st International Conference on Port and Ocean Engineering under Arctic Conditions, Montreal ,Canada*.

Kawamura, T. (1988). Observations of the internal structure of sea ice by X ray computed tomography. *Journal of Geophysical Research*, *93*(C3), 2343.

Martin, S. (1979). A field study of brine drainage and oil entrainment in first-year sea ice. *Journal of Glaciology*, *22*(88), 473–502.

Maus, S. (2009). Synchrotron-based X-ray micro-tomography: Insights into Sea Ice

Microstructure.*Report Series in Geophysics, Proceedings of The Sixth Workshop on Baltic Sea Ice Climate*.

Maus, S., Becker, J., Leisinger, S., Matzl, M., Schneebeli, M., & Wiegmann, A. (2015). Oil Saturation of the Sea Ice Pore Space. In *Proceedings of the 23rd International Conference on Port and Ocean Engineering under Arctic Conditions, Trondheim, Norway*.

Maus, S., Leisinger, S., Matzl, M., Schneebeli, M., & Wiegmann, A. (2013). Modelling oil entrapment in sea ice on the basis of 3d micro-tomographic images. In *Proceedings of the 22nd International Conference on Port and Ocean Engineering under Arctic Conditions, Espoo, Finnland*.

McDougall, T. J., & Barker, P. M. (2011). Getting started with TEOS-10 and the Gibbs Seawater (GSW) oceanographic toolbox. SCOR/IAPSO WG, 127, 1-28.

Nelson, W. G. (1981). Oil Migration and Modification Processes in Solid Sea Ice. *International Oil Spill Conference, American Petroleum Institute*, *1*.

NORCOR, (1975). The Interaction of Crude Oil With Arctic Sea Ice.*NORCOR Engineering and Research Limited Yellowknife, N.W.T.*, Beauforts Sea Technical Report 27

Otsu, N. (1979). A Threshold Selection Method from Gray-Level Histograms. *IEEE Transactions on Systems, Man, and Cybernetics*, *9*(1), 62–66.

Otsuka, N., Kondo, H., & Saeki, H. (2004). Experimental study on the characteristics of oil ice sandwich. In *Oceans '04 MTS/IEEE Techno-Ocean '04 (IEEE Cat. No.04CH37600)* (Vol. 3, pp. 1470–1475).

Petrich, C., Karlsson, J., & Eicken, H. (2013). Porosity of growing sea ice and potential for oil entrainment. *Cold Regions Science and Technology*, *87*, 27–32.

Schindelin, J., Arganda-Carreras, I., Frise, E., Kaynig, V., Longair, M., Pietzsch, T., … Cardona, A. (2012). Fiji: an open-source platform for biological-image analysis. *Nature Methods*, *9*(7), 676–682. http://doi.org/10.1038/nmeth.2019

Timco, G. W., & Weeks, W. F. (2010). A review of the engineering properties of sea ice. *Cold Regions Science and Technology*, *60*(2), 107–129.

Wilkinson, J. P., Wadhams, P., & Hughes, N. E. (2007). Modelling the spread of oil under fast sea ice using three-dimensional multibeam sonar data. *Geophysical Research Letters*, 34(22).

Zack, G. W., Rogers, W. E., & Latp, S. A. (1977). Automatic Measurement of Sister Chromatid Exchange Frequency. *The Journal of Histochemistry and Cytochemistry*, *25*(7), 741–753.

Paper IV
Distribution of oil in sea ice: laboratory experiments for 3-dimensional μ-CT investigations

ISBN 978-82-326-5824-4 (printed ver.)
ISBN 978-82-326-6875-5 (electronic ver.)
ISSN 1503-8181 (printed ver.)
ISSN 2703-8084 (online ver.)

NTNU
Norwegian University of
Science and Technology